TRAPPIST asteroid lightcurves

Auteur : Ferrais, Marin
Promoteur(s) : Jehin, Emmanuel
Faculté : Faculté des Sciences
Diplôme : Master en sciences spatiales, à finalité approfondie
Année académique : 2017-2018
URI/URL : www.trappist.ulg.ac.be; http://hdl.handle.net/2268.2/5023

Uɴɪᴠᴇʀsɪᴛʏ ᴏғ Lɪᴇ̀ɢᴇ

Fᴀᴄᴜʟᴛʏ ᴏғ sᴄɪᴇɴᴄᴇs

Dᴇᴘᴀʀᴛᴍᴇɴᴛ ᴏғ Asᴛʀᴏᴘʜʏsɪᴄs, Gᴇᴏᴘʜʏsɪᴄs ᴀɴᴅ Oᴄᴇᴀɴᴏɢʀᴀᴘʜʏ

Mᴀsᴛᴇʀ Tʜᴇsɪs

TRAPPIST ASTEROID LIGHTCURVES

Composite lightcurve of (20) Massalia

A thesis presented for the degree of Master in Space Sciences by

Mᴀʀɪɴ Fᴇʀʀᴀɪs

Under the supervision of Emmanuël Jehin

Academic Year 2017 − 2018

Contents

Remerciements

Je remercie tout d'abord Emmanuël Jehin pour l'opportunité qu'il m'a donnée de découvrir l'observation et l'étude des astéroïdes. Ses conseils et son enthousiasme tout au long de l'année ont été très appréciés. Je remercie également Jean Manfroid pour ses conseils et ses scripts qui m'ont aidé à réaliser ce travail, Sandrine et Youssef pour leur aide très utile et Fran pour la relecture du manuscrit. Merci aussi à Maxime Devogele pour le stage à l'observatoire de Calern qui m'a donné envie de continuer dans l'observation astronomique, et à toutes les personnes impliquées dans la mise en oeuvre du projet TRAPPIST. Enfin je remercie particulièrement mes amis et ma famille pour leurs soutiens durant mes études.

Introduction

Asteroids are fascinating bodies of the Solar System. They are of various sizes (from a few meters to hundreds of kilometres) and compositions (metallic, rocky or a mix of ice and rocks). They are considered as the building blocks of the planets and they are of utmost importance in the understanding of how the Solar System formed and evolved. Indeed, they are with the comets and the trans-Neptunian objects among the most pristine objects formed in the initial solar nebula, about 4.6 billion years ago. Since their formations, they have experienced many collisions, dynamical perturbations and thermal events. Hence, they not only reflect the initial conditions in the solar nebula but also the following evolution of the Solar System. Asteroids can be studied through ground-based, space-based or in-situ observations, laboratory measurements of meteorites or through theoretical and numerical modelling. They exhibit a large variety of shapes, compositions and orbits. As such, they provide powerful constraints on Solar System formation models.

There are various other reasons to study asteroids. For instance, they may have played a role in the origin and evolution of life on Earth by delivering organic compounds on the surface of our planet and through collisional events greatly impacting the biosphere. Asteroids closely approaching Earth can pose a threat on Earth's life and various mitigation strategies are thus developed. These strategies greatly rely on all-sky surveys in order to forecast potential impacts as far in advance as possible. In the future, technological progresses could also allow humans to explore some near asteroids and to extract their materials also for commercial purposes.

Our understanding of asteroids have dramatically improved since the discovery of (1) Ceres by Giuseppe Piazzi in 1801, then considered to be a new planet. However, they remained mysterious objects in a lot of ways. While it is relatively easy to obtain informations on the physical properties of the surface of the largest and/or closest asteroids, it is far more difficult to probe their interiors. The internal structure is a fundamental property of asteroids that results from their time and location of formation and from their collisional history. Therefore, constraining the internal structures of a large number of asteroids of different compositional classes will allow to better understand the formation and evolution of the planetesimals and the Solar System in general. To learn more about asteroid interiors, an ESO Large Programme (LP), described in Chapter 2, is conducting disk-resolved observations of a substantial fraction of the largest Main-Belt Asteroids (MBAs) with the ESO Very Large Telescope (VLT). Such observations allow to reconstruct the 3-D shape models and thus to derive the volumes. When combined with mass estimations, the bulk densities of the asteroids can then be obtained.

In this work we conducted photometric observations of asteroids in order to obtain their rotation lightcurves. Indeed, the brightness of asteroids usually changes through their rotations due to their irregular shapes. We used two robotic telescopes, TRAPPIST-North and TRAPPIST-South (hereafter TRAPPIST-N and TRAPPIST-S) and obtained a large amount of data in about 50 nights of observations. Rotation lightcurves are needed for the shape

modelling of asteroids, as done by the ESO LP. At this end, we observed 9 MBAs and provided the resulting lightcurves to the ESO LP. We also observed Near-Earth Asteroids (NEAs) to support radar imaging, also used for shape modelling, and to determine new rotation periods.

In Chapter 2, various subjects about asteroids are discussed. Questions about their origins, what they are made of, where they are found in the Solar System, how we can study them and what we can learn from them are developed. Emphasis is given to the photometry of asteroids, as this is the technique we used in this work, and on how such measurements allow to derive rotation periods and shape models. The ESO LP for which we observed large MBAs (D $\geq$ 100 km) is also described.

In Chapter 3 we describe the two robotic telescopes TRAPPIST-N and TRAPPIST-S that we used for the asteroid observations. The scientific goals of the TRAPPIST project are discussed and technical details on the telescopes are given, as well as a few words on the operation of the instruments. This chapter also presents the advantages to have two excellent dedicated robotic telescopes located at two largely separated observing sites.

The Chapter 4 is dedicated to the data acquisition for asteroids and to the processing of the data. The observations are done according to the visibility windows of the asteroids we want to observe. Before each night, observing plans are written and sent to the computers operating the telescopes to tell them which target to observe but also when and how to observe it. The raw images obtained are not directly usable for accurate photometric measurements. They have first to be calibrated by different processes described in this chapter. Details on photometric measurements are also given, with the particularities and difficulties linked to asteroid observations.

In Chapter 5 we present the results of our asteroid observations. The first section is dedicated to the 9 MBAs ((596) Scheila, (476) Hedwig, (89) Julia, (24) Themis, (31) Euphrosyne, (20) Massalia, (145) Adeona, (45) Eugenia and (22) Kalliope) observed in the framework of the ESO LP. A first paper, dedicated to (89) Julia, has recently been submitted (Vernazza et al., 2018). The second section describes the results of the optical observations of 3 NEAs in support of radar imaging for the purpose of shape modelling and rotation periods determination. These are the well known triple asteroid (3122) Florence and the recently discovered K17V12R and K18D01H. The last section is about the observations of (3200) Phaethon during its unprecedented flyby of Earth on December 2017. Phaethon is a very peculiar asteroid with an orbit bringing it closer to the Sun than any other known asteroid and because of the unexpected increase of brightness observed during its perihelion passages in 2009 and 2012. Our observations were aiming to investigate potential colour variations through its rotation and to record the changes in the lightcurve shape and amplitude due to changing viewing geometry and illumination during the Earth flyby. We then used these observations to derive a new shape model and spin axis orientation of Phaethon.

About asteroids

2.1 Introduction

2.1.1 The Solar System formation

To understand the origins of asteroids we have first to look at how the Solar System formed, 4.657 Gyr ago. The formation of a planetary system according to the modern version of the nebular hypothesis starts with a giant molecular cloud. These massive clouds contain mainly hydrogen and helium but also some more heavy elements synthesized by previous generations of stars. They are at equilibrium and do normally not collapse but a local perturbation can lead to the contraction of a part of the cloud. This contraction gives birth to a primitive nebula that will flatten due to its initial rotation, consisting in a star in formation surrounded by a proto-planetary disk. The formation of planets is then done in the following steps. First, the dust particles (a few μm in size) will form larger grains by coagulation. The largest grains will accrete more material and reach kilometer size. Those objects are named the planetesimals and are formed in 1 to 2 million years (Myr). The planetesimals are then large enough to deflect smaller bodies and accrete them. Because of the dynamical friction, eccentricity and inclination will decrease for the biggest bodies but increase for the smallest ones. This will increase the probability of collisions and the largest start to grow more rapidly. At this stage the growth rate bodies increase as a function of their masses, leading to a runaway growth where the planetesimals accrete all the nearby material and form Mars size bodies, the planetary embryos. Finally, they will collide and form in about 10 Myr the core of giant planets, that will then continue to slowly accrete the remaining gas. The process for the terrestrial planets is slower and takes 10-100 Myr.

During their formation, planets remove all material in their vicinity. However, between them a lot of small bodies can still be found. Today, only 0.1% of the mass of these bodies remains. To understand what happened to them we have to look at the Grand Tack and the Nice model scenarios.The Grand Tack proposes that after its formation, Jupiter migrated inward from 3.5 to 1.5 au due to interactions with the gaseous disk. Later, Saturn also migrated inward, quickly catching-up with Jupiter with which it entered in a 2:3 mean motion resonance. Jupiter was then doing 3 revolutions around the Sun when Saturn was doing exactly 2. Because of the configuration of the two planets and the disk, the migration reversed and then stopped when the gas was depleted enough. The Nice model postulates that when Saturn and Jupiter migrated and entered in mean motion orbital resonance, they excited the orbits of the small bodies and ejected them all around. This scenario can explain the "Late Heavy Bombardment" and the existence of populations of asteroids like the Neptune and Jupiter trojans.

2.1.2 The Main-Belt of Asteroids

The Main-Belt of Asteroids (MBA) is a region between Mars and Jupiter where orbit hundreds of thousands of asteroids. The total mass of the MBA represents only 4% of the mass of the Moon and around 1/3 of it is due to the dwarf planet Ceres (D = 950 km). The gravitational influence of Jupiter prevented the formation of a planet in this region of the Solar System. Jupiter is also at the origin of regions inside the main-belt where no asteroids are found for peculiar periods, the Kirkwood gaps. They correspond to unstable orbits due to mean motion resonances with Jupiter (for instance 3:1, 5:2 or 2:1). The Kirkwood gaps are visible in Fig. 2.1, as well as the mass distribution as a function of the semi-major axis. Asteroids near the internal edge of the MBA are mostly of the stony type with a geometric albedo of 20% while outer asteroids are mostly carbonaceous with an albedo of only 4%. The orbital elements of the asteroids in the MBA reveal groups of asteroids with similar eccentricities and inclinations. These asteroids with similar orbits can be related to each others and are called asteroid families. They originate from of a single parent body that endured an important collision and the fragments were dispersed but stayed in similar orbits.

2.1.3 Near-Earth Asteroids

NEAs are by definition asteroids with perihelion distances of less than 1.3 au. They are part of the Near-Earth Objects (NEO) group that also contains comets. Their orbits have been perturbed by the gravitational attraction of the planets and other big bodies and were sent in the Earth's neighbourhood. Close encounters with these asteroids are great opportunities to study them because asteroids are usually too far and too faint to do so. High-resolution radar observations can be carried out during NEAs flyby. The informations acquired by studying NEAs helps to better understand the dynamical and collisional history of the Solar System. They are also known to have played an important role in the past Earth geology and history of life.

NEAs can be classified in four groups based on their orbital characteristics (the perihelion distance q, aphelion distance Q and semi-major axis a):

- **The Amors** (named after (1221) Amor) have orbits between those of Earth and Mars ($a \geq 1$ au, 1.017 au $\leq q \leq 1.3$ au).

- **The Apollos** (named after (1826) Apollo) have semi-major axes larger than Earth's and cross its orbit ($a \geq 1$ au and $q \leq 1.017$ au).

- **The Atens** (named after (2062) Aten) have semi-major axes smaller than Earth's and cross its orbit ($a \leq 1$ au, $Q \geq 0.983$ au).

- **The Atiras** (named after (163693) Atira) have orbits entirely within the orbit of Earth ($a \leq 1$ au, $Q \leq 0.983$ au). The values 1.017 au and 0.983 au are the Earth's aphelion and perihelion distances.

Some NEAs are also classified as Potentially Hazardous Asteroids (PHAs) based on their "Minimum Orbit Intersection Distance" (MOID) and absolute magnitude[1] H. By definition, PHAs are asteroids with MOID $\leq$ 0.05 au and H $\leq$ 22 mag, which corresponds to a diameter greater than about 140 meters assuming an albedo of 14%[2]. Indeed, their close approaches make them great targets to observe but they might also pose a threat in case of impact with Earth. In order to minimise the threat, various surveys have undertaken NEAs searches in order to forecast potential impacts as far in advance as possible. As a result, a lot of discoveries were made in the early 2000s and the number of NEAs larger than 1 km that are known is estimated to be about 93% of the

---

[1]An asteroid's absolute magnitude is its visual magnitude when observed at a zero phase angle and placed at a distance of 1 au from the Earth and the Sun.

[2]https://cneos.jpl.nasa.gov/about/neo_groups.html

estimated population. Nevertheless, new discoveries are still made each year, for smaller ones often after the closest approach.

News about NEAs and future close approaches can be found on the NASA's website Asteroid Watch [3].

2.1.4 Asteroid taxonomy

Asteroid taxonomy aims to classify asteroids based on their spectrum, colour and albedo. The main taxonomic systems are the Tholen, SMASS and Bus–DeMeo classifications.

The Tholen classification proposed by Tholen (1984) is based on spectra taken during the Eight-Color Asteroid Survey (ECAS; Zellner et al. (1985)) and albedo measurements of 978 asteroids. 14 groups are defined, the main ones being the C (carbonaceous) and S (stony) classes.

The Small Main-Belt Asteroid Spectroscopic Survey (SMASS) acquired spectra in the visible of 1447 asteroids. The SMASS classification, composed of 26 categories, is based on those spectra and does not use albedo information (Bus and Binzel, 2002). More than 90% of the MBAs fall into the S, Ch/Chg, B/C and P/D classes. The SMASS classification was later on extended by the Bus-DeMeo taxonomy using near infrared spectra (DeMeo et al., 2009).
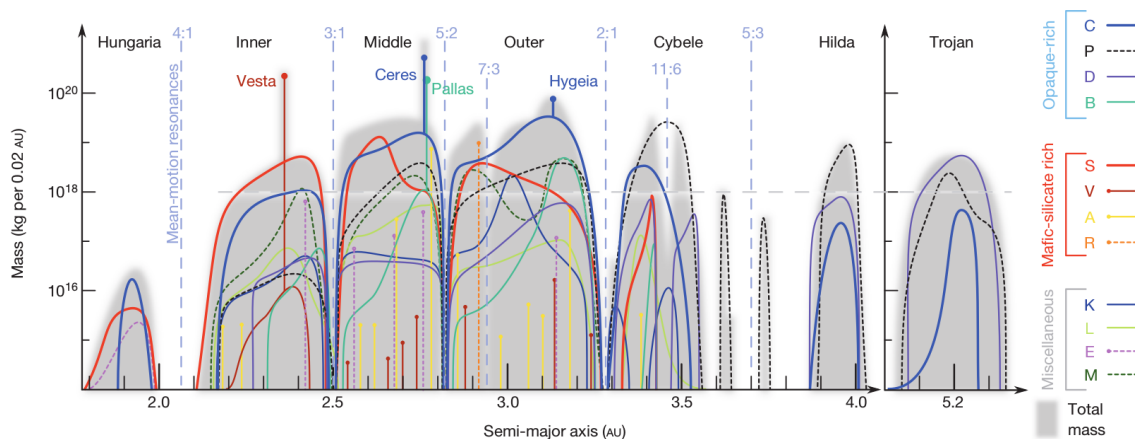
Figure 2.1: Compositional mass distribution of the MBA (DeMeo and Carry, 2014).

2.1.5 Meteorites

Meteorites are fragments of asteroids or comets that have reached the surface of Earth. Studying them helps to understand the formation and composition of the Solar System and of the various planetesimals. Meteorites are usually classified based on their compositions. The main groups are the stony, iron and stony-iron meteorites. The stony group is further divided in two types of meteorites, the chondrites and achondrites. The achondrites and iron meteorites have undergone planetary or asteroidal differentiation. They have melted and they show signs of metamorphism due to processes such as core-mantle differentiation (that separates metals from silicates) and crust-mantle formation. In the other hand, the chondrites are more primitive and remained mostly unchanged since the formation of their parent bodies. They are composed of chondrules embedded in a matrix. The chondrules are small round grains that formed at high temperature and in which all the minerals are mixed together. They are thought to be one of the oldest material of the Solar System. The carbonaceous chondrites are the meteorites whose composition match the best the solar and proto-stellar nebula composition.

---

[3] https://www.jpl.nasa.gov/asteroidwatch/

Meteorite spectra measured in laboratory can be compared to those of observed asteroids which provides informations on their compositions. When asteroids can be linked to meteorite analogues and if estimations of bulk densities are available, comparing those densities with those of meteorite, provides the asteroids porosity.

2.1.6 How to study asteroids?

There are various techniques to study asteroids that provides complementary informations. Those techniques are briefly presented hereafter. For this work we used asteroid photometry and it will be described separately in more details in Sect. 2.2.

Asteroid spectroscopy aims primarily to identify features in asteroid spectra to better understand their surface composition and to try to link them to meteorite analogues. Asteroid spectroscopy can be done in different parts of the electromagnetic spectrum. Most observations were previously done in the visible range because of the atmosphere transparency at those wavelengths. Spectroscopy in the visible can be used to distinguish the carbonaceous from the silicaceous asteroids. Spectroscopy in the near infrared range is more difficult due to the strong water vapour absorption. However, most observations are now done at those wavelengths because of the numerous absorption bands from different mineralogical compounds that are found there.

Asteroid polarimetry study the effects on the polarisation of light after reflection over the surface of an asteroid. The partial polarisation of the unpolarised light of the Sun depends among other things on the texture and composition of the surface, the wavelengths and the phase angle. The phase angle of an object is the angle between the Sun, the object and the observer. Polarimetric observations can be used to help derive the geometric albedo, size and taxonomic classification of an asteroid.

Infrared radiometry is mostly used to determine the size, thermal inertia, surface roughness and emissivity of asteroids. The size is derived from the measurement of the disk-integrated thermal infrared flux of the asteroid, which depends on the square of its diameter. The measurements are made in the thermal infrared (from $4\,\mu m$ to $30\,\mu m$) in the specific windows where the atmosphere is relatively transparent. Space-based telescopes are not limited by atmosphere transparency and thermal background, hence they can observe much fainter asteroids and with smaller uncertainties.

Radar imaging is an active radio astronomy technique. It consists in analysing the reflection of microwaves or radio waves on the asteroid surface. The time delay gives a direct measurement of the distance, hence the combination of both optical and radar observations allow to compute very accurate orbits. Two-dimensional images can be produced by measuring the distribution of echo power in time delay and Doppler frequency. Moreover, if images are obtained at enough viewing geometries, a 3-D shape can be derived as well as the rotation state (details can be found in Ostro et al. (2002)). The echo power is proportional to the inverse fourth-power of the distance, hence the technique is achievable for NEAs and the largest members of the MBA only. The most used radar astronomy facilities for such measurements are the Arecibo Planetary Radar and the Goldstone Solar System Radar (Ostro et al., 2002).

Stellar occultation by an asteroid is an event that occurs when the asteroid pass in front of a star and temporarily blocks its light as seen from Earth. The duration of this event, combined with the apparent velocity of the asteroid on the plane of the sky, allows to derive a physical length (called a chord) on the asteroid 2-D disk. Provided that several chords are detected from different locations, a 2-D profile of the asteroid on the plane of the sky and at the time of the event can be obtained. Stellar occultations can be observed even with small aperture and for targets with small angular sizes such as the Trans-Neptunian Objects (TNOs). The main difficulties with stellar occultation observations comes from the uncertainties on the positions of the star and the

asteroid. Many observers are thus needed to cover a large geographical area. Moreover, those events are rare and thus hard to reproduce. The accuracy of a chord measurement depends on the accuracy of the timing of the star disappearance and reappearance. A big source of error comes from the absolute timing between chords from different observers when merging them together. The stellar occultation technique is mainly used to determine sizes of asteroids but when enough chords are obtained it can even provides details on their shapes. In rare cases, atmospheres and rings can be detected and it is also helpful to set scale to a dimensionless 3-D shape.

2.2 Photometry of asteroids

Asteroid photometry consists of measuring the asteroid brightness variation with time due to its rotation around its spin axis. We will here focus on disk-integrated and ground-based photometry which is the technique used in this work. Photometry can also be done by spacecrafts and disk-resolved observations of asteroids by flyby missions such as the ESA Rosetta, NASA Dawn or NASA New Horizons have allowed significant advances in the domain in the past decade (Li et al., 2015).

The brightness of an asteroid can vary with the viewing angle, the illumination, the changing distance from the Earth and the Sun and with its rotation (because of the asteroids irregular shapes). A rotational lightcurve is the measured flux or magnitude variation of an asteroid during its rotation due to the asteroid presenting alternatively smaller and larger faces. A lightcurve can be folded on the rotation period with the flux or magnitude being plotted as a function of the rotational phase and is then called a phased lightcurve. Rotational phase goes from 0 to 1 in unit of the rotation period and is given by

$$phase = \frac{t - t_0}{P_{rot}} \text{ (modulo 1)}$$

with t_0 being an arbitrary initial time, often chosen as the time of the first measurement in the data set. Colour and albedo variation on the surface will also result in brightness variations, however the collisional erosion process and space weathering create regoliths with time. Thus, asteroid surfaces are mostly uniform in colour and albedo. Spatially unresolved data are of course less rich than the disk-integrated ones, but a lot of information can still be obtained from asteroid lightcurves. With a single lightcurve, one can in principle determine the rotation period. With multiple lightcurves taken at different viewing angles, a shape model and the pole coordinates can be computed. At favourable geometries, the signal of a multiple system can also be detected on optical lightcurves, as illustrated for (22) Kalliope in Sect. 5.1.9.

Photometric measurements

In this section, some aspects of photometric measurements are presented. This discussion is based on the book "*A Practical Guide to Lightcurve Photometry and Analysis*" (Warner, 2016).

The "**air mass**" (or "**airmass**") is the path-length that the light has to go through the atmosphere to reach the observer and is related to the attenuation of light by the air. It is minimal and equal to 1 at the zenith but quickly increases at low altitude. A good approximation for the airmass X, down to about 30° altitude, is given by

$$X = \frac{1}{\cos(z)}$$

where z is the zenith distance:

$$z = 90° - \text{altitude}.$$

There are also more complex formulae of the airmass that should be used for more precise calculations. For a target near the horizon, and so at higher airmass, the light will travel through a longer path than for a target near the zenith and will be strongly dimmed. Also, as light scattering by the air is frequency dependant, blue light is scattered more than red light by the atmosphere. Thus a star will appear redder at higher airmass. Hence, one should not observe at too high airmass as differential colour extinction will appear, as well as increased scintillation making the data more noisy.

The "**seeing**" is a measurement of atmospheric turbulences that are created by temperature differences in layers of air. The temperature differences result in changing refractive index in the light path and cause an object's light to spread on more pixels, decreasing measurements precision and accuracy. The seeing is measured by the Full Width at Half-Maximum (FWHM) of a star's profile and is expressed in arcseconds. The "**scintillation**" is the phenomenon of an object's light to arrive in several packets of light due to small air cells in the atmosphere. When observed with small aperture (like the eyes), this will cause the object to twinkle, causing rapid brightness variations. These fluctuations can be reduced by using a larger aperture and longer exposure times.

The first order extinction is the dimming of light going through the atmosphere, depending on the wavelength. It is measured in unit of magnitude per airmass. The second order extinction depends on the airmass at which an object's light is measured and its colour. It is measured in unit of magnitude per airmass per unit of colour index. The colour index is the difference of the magnitudes of an object measured in different filters, e.g (B-V).

The way to measure an object flux on an image is called "**aperture photometry**". It consists of taking the total flux in a measuring aperture, a circle centred on the object. This total flux is then normalised to an exposure time of one second. The background flux is estimated by taking the median or the a clipped-average of the flux in an annulus also centred on the object but separated from the measuring aperture by a dead zone.

There are two different ways to reduce the data called absolute and differential photometry. For this work, only differential photometry was used.

Absolute photometry is the technique that consists of reducing the measurements of the target to absolute magnitude on a standard photometric system. The absolute magnitudes can then be directly compared to absolute magnitude from catalogues or other observers. Absolute photometry requires to correct for the first and second order extinction. This correction is done by taking measurements of standard stars in widely varying location in the sky and comparing the value in catalogues containing the absolute magnitude of these standard stars. Good and stable atmospheric conditions are needed when using this technique.

Differential photometry takes a completely different approach to photometric measurements. It consists in taking the difference between the target magnitude and the average magnitude of multiple comparison stars. This way, variations of the flux of the target that are not intrinsic to it are corrected. This includes airmass variations or clouds passing in front of the field of view. The comparison stars must be close to the target to have similar airmass and atmospheric conditions. If possible they should also have spectral types as close as possible to that of the target (the spectral type of the Sun for asteroids) to avoid differential extinctions. However, this effect can be reduced by averaging the signal of a large number of comparison stars. In principle, one comparison star could be sufficient but at least two should always be used to check if the signal of the other star is stable. Indeed, some stars have their own brightness variability and they are not suitable as comparison stars. Taking a large number of comparison stars also have the advantage to reduce the noise in the measurements. Differential photometry is more accurate than absolute photometry when measuring small variations.

2.3   Rotation period

The basic physical property we can derive from lightcurves of asteroids is the rotation period. About 90% of the asteroids have a rotation period between 2.4 and 24 hours but some rotate in several tenths of days. For large asteroids (D > 150 m), a cutoff in their rotation periods is observed at 2.4 hours, below that the centrifugal force would become too strong for them to maintain their integrity because of their "rubble pile" structure (Pravec and Harris, 2000). In principle a single lightcurve covering a full rotation is sufficient to determine the period, but the accuracy will mainly be set by the time span of observations. Lightcurves from multiple nights can be merged together to increase the amount of data. It is also the only way to have a complete coverage of the rotation curve of slow rotators for ground-based telescopes or when the visibility windows are short. Observations separated by large time intervals (weeks or months) are useful to refine the accuracy of the rotation period because they contain a large number of rotation cycles. On the other hand, consecutive nights contain a minimum number of revolutions and help to reduce the number of possible aliases. The aliases of a period are the other periods which seem to also fit the data. They can appear when observing at regular intervals an asteroid with a period that is almost a multiple of this interval. In this case there is an integer number of cycles between the start of the different sessions and the same part of the rotation curve is observed each time.

To determine rotation periods from our measurements we used the software Peranso (PERiod ANalysis SOftware), developed by Tony Vanmunster from the CBA Belgium Observatory[4]. Peranso is a powerful and user-friendly software that proposes various time-series analysis methods applied to astronomical data. An introduction to the software is given in Paunzen and Vanmunster (2016). Among the implemented methods we used FALC and ANOVA.

The Fourier Analysis of Light Curves (FALC; Harris et al. (1989)) is a Fourier method that represents lightcurves with series of sines and cosines:

$$I(t) = \bar{I} + \sum_{i=1}^{n} \left[A_i \sin \left(\frac{2\pi i}{P} \right)(t - t_0) + B_i \cos \left(\frac{2\pi i}{P} \right)(t - t_0) \right]$$

where $I(t)$ is the measurement value (magnitude or intensity) at time t, $\bar{I}$ is the mean value of the data set, A_i and B_i are the Fourier coefficients, P is the rotation period and t_0 a zero-point time. The uncertainties on the measurements are taken into account and each observation sets are assigned a new zero-point (magnitude level). The above function is then fitted by a linear least-squares. It is also possible to determine what is the most significant fit order to work with.

ANOVA is a statistical method that represents lightcurves with periodic orthogonal polynomials and uses the analysis of variance (ANOVA) statistic to evaluate the goodness of the fit. It was proposed by Schwarzenberg-Czerny (1996). The strengths of the method are its suitability for nonsinusoidal signals, a strong peak detection sensitivity and a good damping of alias periods.

Figure 2.2 shows two periodograms of the same data with the two methods.

2.4   Shape models

The shape of large asteroids are close to spheres or ellipsoids. An ellipsoid is characterised by the length of three axes (a, b and c with $a \geq b \geq c$). If the rotation state is relaxed, as it is usually the case for large asteroids, the spin axis is aligned with the smallest axis. Contrary to the large bodies, smallest asteroids exhibit a great

---

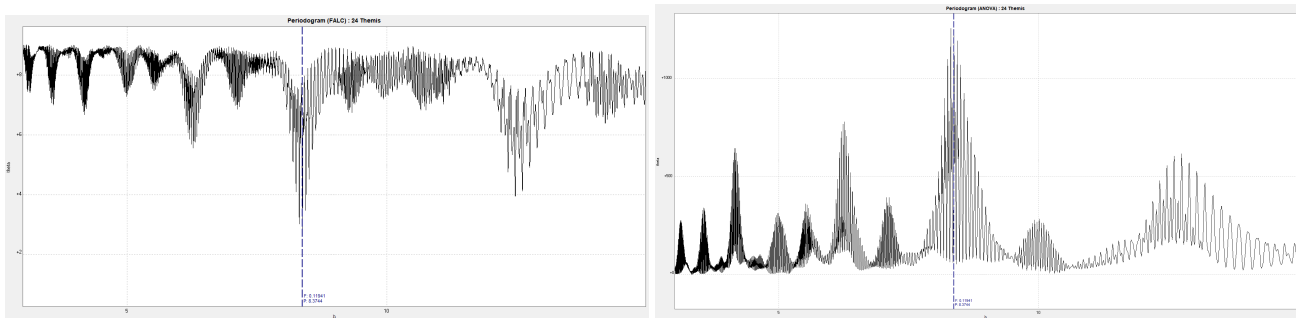[4] http://www.cbabelgium.com/peranso/

Figure 2.2: Example of periodogram with the two methods for (24) Themis. *Left*: FALC method. The prominent period is given by the lowest peak. *Right*: ANOVA method. The prominent period is given by the highest peak.

diversity of shapes, as revealed by space missions and disk-resolved images from the ground. Their shapes can be very irregular, can have large concavities or even be bi-lobed. Their rotation states can be excited, making them rotate along more than one axis.

Shape models are the ultimate result that can be obtained by analysing rotation lightcurves of asteroids. The lightcurve amplitudes provide constraints on the relative dimensions of asteroids. The ratio of the areas of the largest and the smallest faces seen during a rotation can be approximated by

$$Ratio = 10^{Amplitude/2.5}$$

Even more informations, on the shape and spin axis orientation, can be obtained using a set of lightcurves taken at different viewing angles.

2.4.1   Asteroid models from disk-integrated photometry

Rotation lightcurves taken at different phase angles, and so at different illuminations and viewing directions, can be used to reconstruct the 3-D shape and the spin state of an asteroid. This technique can be applied to MBAs provided several apparitions are observed or to NEAs approaching close enough to Earth. However, it is not possible for Centaurs and TNOs that are never seen at geometries significantly different from opposition. This reconstruction is done with the *lightcurve inversion* method described in Kaasalainen and Torppa (2001) and Kaasalainen et al. (2002a). Lightcurve inversion is a case of inverse problems, some of the most important mathematical problems with wide applications. These are problems that based on the observations (here multiple lightcurves) calculate the properties that caused them (here the asteroid shape, pole direction, surface properties ...). The lightcurve inversion produce an approximate global shape of the asteroid and a unique solution is produced only if the derived shape is convex.

The method has already been used for hundreds of asteroids and more than 1700 models are publicly available at the Database of Asteroid Models from Inversion Techniques[5] (DAMIT; Durech et al. (2010)). DAMIT also contains the source codes of the lightcurve inversion procedure *Convexinv*.

This procedure computes the shape, spin and scattering models that gives the best fit to the input lightcurves (calibrated or uncalibrated). In short, it uses the Levenberg-Marquardt algorithm to minimise the relative chi-square defined as

$$\chi_{rel}^2 = \sum_i = \left\| \frac{\boldsymbol{L}_{obs}^{(i)}}{\bar{\boldsymbol{L}}_{obs}^{(i)}} - \frac{\boldsymbol{L}^{(i)}}{\bar{\bar{L}}^{(i)}} \right\|^2$$

[5]http://astro.troja.mff.cuni.cz/projects/damit

where $\boldsymbol{L}_{obs}^{(i)}$ obs and $\boldsymbol{L}^{(i)}$ are observed and modelled lightcurves and $\bar{L}_{obs}^{(i)}$ and $\bar{L}^{(i)}$ are the corresponding average brightness.

The format of the lightcurve data files is the following. The first line contains the number of points followed by the number zero for relative or 1 for calibrated lightcurves. This line is followed by the data themselves. The first column contains the light-time corrected epochs in Julian Days, the second column is for the brightness in intensity units and the six last columns are for the ecliptic astrocentric cartesian coordinates x, y, z of the Sun and of the Earth in au.

At the end of the process, different output files are created. The file with the output parameters contains the solution for the spin ecliptic pole coordinates (λ, β) [deg], the rotation period, and the scattering parameters. The output lightcurves file contains the synthetic brightness values generated with the computed shape model. It allows to compare the observed lightcurves with the modelled brightness. A file with output areas and vertices contains the informations that describe the shape model by its Gaussian image. This file can then be used as an input for the *minkowski* procedure to create a convex polyhedron. If needed, the *standardtri* procedure can convert the polyhedron from *minkowski* into a new polyhedron that has all facets triangular.

The validity of the inversion method has been tested by comparing the results with models from disk-resolved images available for a few asteroids. The global triaxial dimensions agreed within 5-10% and the pole coordinates also agreed within a few degrees (Kaasalainen et al., 2002a).

2.4.2   Asteroid models from multiple data sources

The apparition in the early 2000s of adaptive optics facilities able to achieve disk-resolved imaging of small bodies such as NACO at the VLT triggered the development of shape modelling techniques able to combine data obtained with different techniques (Durech et al., 2015).

The addition of complementary data sources to photometry allowed great progress in the field of asteroid models reconstruction. Indeed, disk-resolved data contains much more information than the disk-integrated ones. They allow to recover fine-scale details and non-convexities. The optical lightcurves are still essential since they stabilise the optimisation process and provide informations on regions of the asteroid not covered by other data sources.

The data types that can be used include disk-resolved images from AO and flybys, stellar occultations, interferometry, thermal radiometry and radar imaging, while photometry remains the main source of data.

The softwares used for asteroid modeling from multiple data sources include KOALA and ADAM. KOALA (Knitted Occultation, Adaptive optics and Lightcurve Analysis; Carry et al. (2012)) uses a combination of optical lightcurves, disk-resolved images and stellar occultation chords and is based on the extraction of a silhouette contour for each images. The ADAM (All-Data Asteroid Modelling) algorithm, presented in Viikinkoski et al. (2015), can use any combination of data sources and does not require to process the images to extract contours.

2.5   The ESO Large Programme: "Asteroids as tracers of Solar System formation: Probing the interior of primordial main-belt asteroids"

This ESO Large Programme (LP) aims to characterise the interior of primordial main-belt asteroids to provide unprecedented constraints on Solar System formation models by determining their bulk density. It carries out ground-based adaptive optics observations at the ESO Very Large Telescope (VLT) with the AO camera SPHERE

and will observe most of the large MBAs (D $\geq$ 100 km). It also investigates other topics such as the multiplicity rate of asteroids, their variety of shapes and crater distributions. Observations are spread over four semesters, from April 2017 to March 2019 and sample the four main compositional classes (S, Ch/Cgh, B/C, P/D).

There are various methods such as polarimetry or spectroscopy to obtain information of the surface of asteroids (Sect. 2.1.6) and so the surface composition of most large MBAs is quite well known. However, probing the interior of these objects is more challenging, leaving their internal structure mostly unknown. The bulk density is the most important physical property used to characterise the interior of asteroids but it has only been measured for a few with space probes, such as the ESA Rosetta or NASA Dawn missions.

There are other relevant physical properties that have to be taken into account. Indeed, the internal structures of asteroids results mainly from three things: formation location, time of formation and collisional history. The formation location determines the initial material that made the asteroid, mostly rock in the inner Solar System and more icy when formed further from the Sun. The time of formation determines the amount of radionuclides with short life time present to heat the asteroid. This heat source could have led to the differentiation of the asteroid. Finally the collisional history is very important since collisions can create voids in the interior of asteroids and increase their porosity.

Porosity is an important property of the internal structure of asteroids. It can be estimated by comparing asteroids and meteorites densities. Macroporosity ranges from 0% up to 50-60% for rubble-pile asteroids (Carry, 2012). For asteroids with large macroporosity it is no longer possible to use their bulk densities to characterise their internal structures. Fortunately, objects like the minor planets and the largest asteroids (D $\geq$ 100 km) usually have much lower macroporosity and their internal structure remained mostly intact since their formations. The goal of the ESO LP is to determine the bulk density of these rather compact objects via disk-resolved imaging and interpret it in terms of bulk composition. Observation through their rotation allows to derive their tridimensional shapes and thus their volumes, which, when combined with already available estimations of their masses, provides determination of their bulk densities. The high-resolution observations with the VLT also provide the crater-size ($\geq$ 30 km) distribution and thus characterisation of the crust of the asteroid. Indeed, large impacts into a low density outer crust result in larger craters than for higher density.
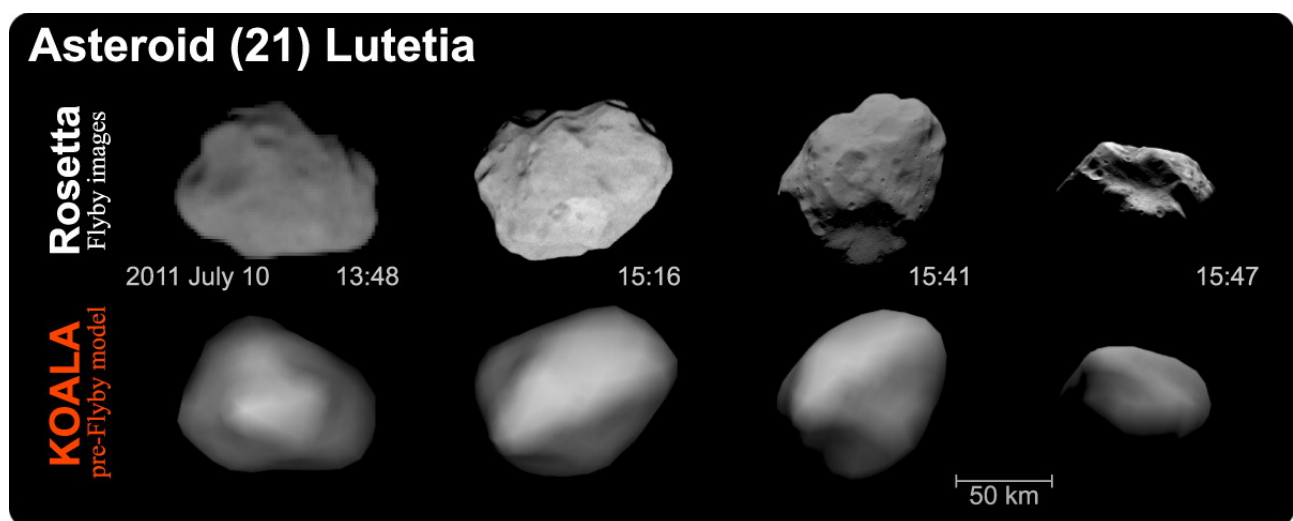

Figure 2.3: Comparison of the shape modelling technique with the Rosetta fly-by of (21) Lutetia (Carry et al., 2012).

The techniques have already been applied to several asteroids (e.g. Marsset et al. (2017)), and successfully

validated by in situ space missions. For instance, the shape and spin orientation of (21) Lutetia have been derived with disk-resolved images before being briefly visited by the ESA Rosetta mission (Carry et al., 2010). The results are very convincing as the spin axis was accurate within 2°, the diameter within 2% and the volume within 10% (Carry et al., 2012). The modelled 3-D shape was also in very good visual agreement with the Rosetta images (Fig. 2.3), assessing the validity of the technique.

Data from stellar occultations and especially optical rotation lightcurves are used to derive their models. There are already convex shape models from existing lightcurves for most of the targets. However, new data are needed to refine the models, especially lightcurves taken at about the same time and so at the same view angle and illumination than the disk-resolved images. This is the reason why new lightcurves like the ones we obtained during this work are so useful and will be collected regularly as the project is carried on.

The TRAPPIST telescopes

3.1 Scientific goals

The TRAPPIST telescopes[1] (TRAnsiting Planets and PlanetesImals Small Telescopes; Jehin et al. (2011a)) are twin robotic telescopes with a diameter of 0.6 m. TRAPPIST-S is installed at the ESO La Silla Observatory in Chile since 2010 and TRAPPIST-N is in operation at the Oukaïmeden Observatory (Morocco) since June 2016. They are operated by the Origins in Cosmology and Astrophysics (OrCA) group of the department of Astrophysics, Geophysics and Oceanography (AGO) of the University of Liège (Belgium). The Moroccan telescope is the result of a collaboration with the Cadi Ayyad University. The main goals of the project are the detection and characterisation of exoplanets via the transit method and the study of small bodies of the solar system. A comparison of the characteristics of the two telescopes is given in Tab. 3.1.

The first TRAPPIST program concerns photometric observations of transiting exoplanets. The first part consists in follow-up observations of planetary candidates of transit surveys. It allows to reject false positive scenarios and to determine the system parameters when a planet is confirmed. A second goal is the refinement of orbital and physical parameters of known transiting system. The third and main part is now the photometric monitoring of close and bright ultra-cool dwarfs ($T_{eff} \leq 2700$ K). These observations are also part of a new project named SPECULOOS[2] (Search for habitable Planets EClipsing ULtra-cOOl Stars) aiming at finding Earth size planets transiting the nearest ultra-cool dwarfs. TRAPPIST observations and follow-up observations by the NASA Spitzer Space Telescope led to the spectacular discovery of 7 Earth-size temperate planets around the nearby (12 pc, i.e. 39.5 ly) star TRAPPIST-1-a (Gillon et al., 2016, 2017).

The second largest observational time is dedicated to comets. The bright comets are observed with narrow-band cometary filters to monitor their gas (OH, NH, CN, C_2 ...) and dust production rates (Jehin et al., 2014b). Photometric monitoring on long time-scale allows to follow the activity and composition of comets along their orbits and as a function of their heliocentric distances. The rotation period of their nuclei can also be measured, as well as activity bursts or the apparition of jets in parallel to observations performed with larger telescopes (e.g Jehin et al. (2014a)). The faint comets are regularly observed with broad-band filters to measure their dust production rates, magnitudes and positions. Observations were done in this case in support of NASA EPOXI (Jehin et al., 2011b) and ESA ROSETTA (Jehin, 2015; Snodgrass et al., 2016).

TRAPPIST is also used to study trans-Neptunian objects and centaurs. Photometric observations of stellar occultations of these objects allow, when several chords are observed, to obtain information on their diameters,

---

[1]http://www.trappist.uliege.be/cms/c_3300885/en/trappist-portail
[2]https://www.speculoos.uliege.be/cms/c_3272698/en/speculoos-portail

shapes and geometric albedo. Eventual atmospheres and rings can also be detected. TRAPPIST was involved in the stellar occultation of the dwarf planet Eris leading to the revision of its radius (Sicardy et al., 2011) and in the discovery of a system of rings around the largest Centaur, Chariklo (Braga-Ribas et al., 2014).

Photometric observations of asteroids have also been conducted in the past with TRAPPIST to obtain information on their rotation periods, shapes and rotational states (e.g Pravec et al. (2014)).

The possibilities and advantages given by the TRAPPIST telescopes are various. The first is the large amount of observation time available for dedicated projects. As the telescopes are operated by Liège we avoid the tedious and time consuming process of observational time request. When the Moon is bright is usually a good time for asteroids observations as they are less sensitive to the moon illumination than comets and their extended and faint coma. We can also be very reactive in our observations, for instance for a recently discovered NEA an observation can be decided in a very short time. Another strength to have two telescopes is the large sky coverage. Their locations in two different hemispheres and the important difference in longitude allow an access to the whole sky. When the target is visible from both sites it is in addition possible to start to observe with TRAPPIST-N and then with TRAPPIST-S allowing very long observing sessions. It is particularly convenient for asteroids with long rotation periods.

3.2 TRAPPIST-South

TRAPPIST-S is located at 2400 m of altitude in the ESO La Silla Observatory in the Atacama desert in Chile. This site offers some of the best observing conditions in the world, with very good atmospheric stability and about 300 clear nights per year. The Atacama desert hosts several famous astronomical observatories such as Paranal hosting the Very Large Telescope (VLT), CTIO hosting among many other telescopes the 8 m Gemini-South telescope or the very large radio interferometer array ALMA.
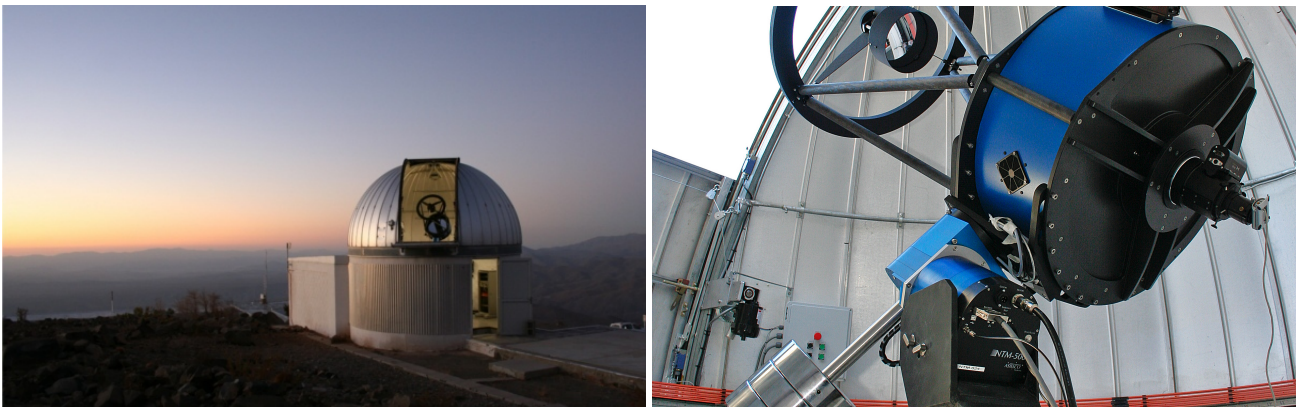

Figure 3.1: TRAPPIST-S telescope at ESO La Silla Observatory (MPC Observatory code: I40).

The telescope is a 0.6m f/8 Ritchey-Chrétien built by the German ASTELCO company[3]. The use of aluminium and carbon fiber in an open design makes it very light (75 kg with instruments). The compact German equatorial mount uses direct drive torque motors allowing fast slewing, accurate pointing and tracking and no periodic errors. The CCD camera is a FLI ProLine PL3041-BB with a back-illuminated Fairchild chip of 2048×2048 pixels and a field of view of $22' \times 22'$. The pixel size and scale are respectively of $15\,\mu m$ and 0.64 arcsec/pixels. The chip is cooled by Peltier effect to $-55\,°C$ below the ambient temperature with a stability

---

[3] http://www.astelco.com/

of 0.1 °C. The dark current is 0.1 e/s/pixel and the gain is 1.26 e/ADU. The quantum efficiency (QE) of the Fairchild chip which is the ratio of the number of collected electrons over the number of incident photons peak at 96% at 750 nm (Fig. 3.2). The camera can be operated with 3 possible read-out modes, 1×1 / 1×2 / 2×2 MHz, corresponding to read-out noises of 9.5 / 14 / 14 electrons and read-out times of 6 / 4 / 2 seconds. For our observations we used the slower 1×1 MHz mode in order to reduce the noise.
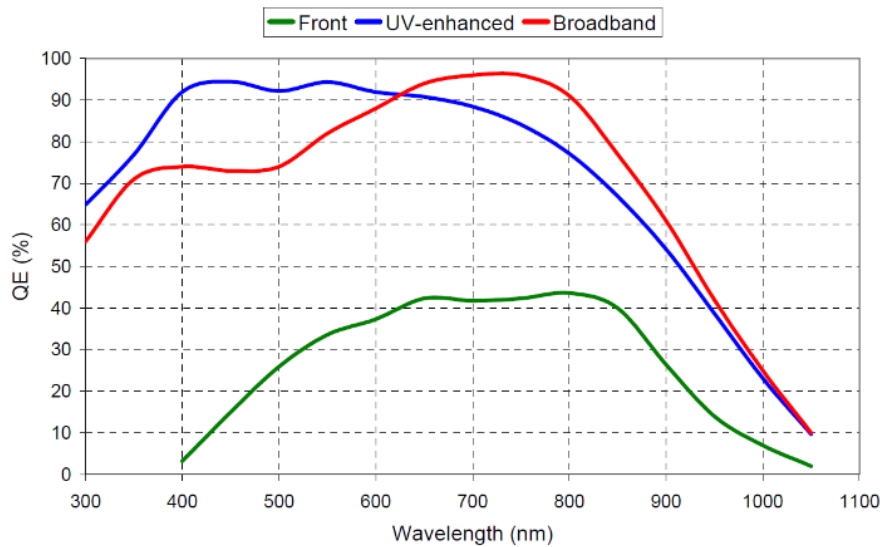

Figure 3.2: QE curve of TRAPPIST-S CCD PL3041-BB Fairchild chip (broadband curve).
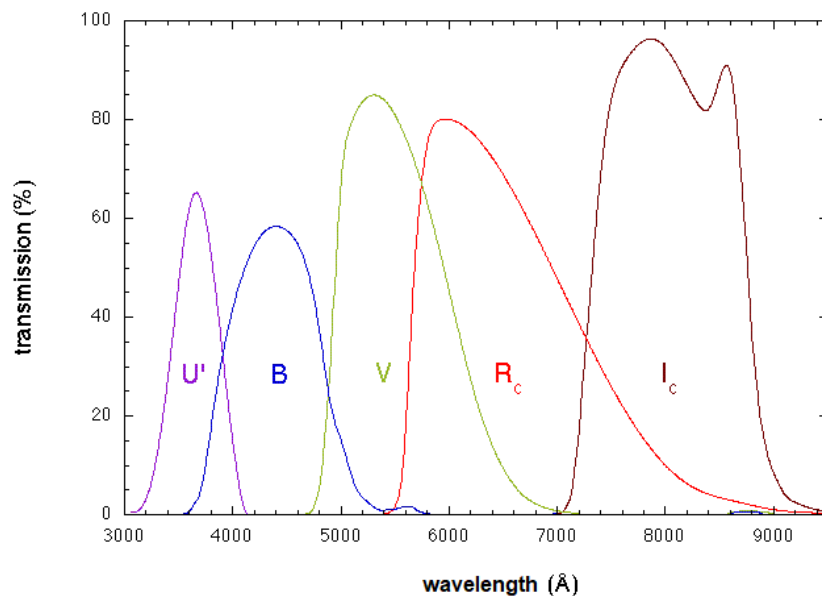

Figure 3.3: Transmission curves of the TRAPPIST-S and TRAPPIST-N broad band filters used for asteroid photometry.

Observation with TRAPPIST-S can be done with a large set of filters. A double Apogee filter wheel gives access to 7 broad-bands filters (Johnson-Cousins B,V,Rc,Ic, Sloan z and exoplanet filters I+z' and Exo) and 11 narrow-band cometary filters designed by NASA for Hale-Bopp observation in 1997 (OH, NH, CN, CO^+,C_3, BC, C_2, GC, RC NaI and H_2O^+). The transmission curves of the Johnson-Cousins filters we used for the asteroid observations are shown in Fig. 3.3.

3.3 TRAPPIST-North

The Oukaïmeden Observatory located at 2750 m of altitude in the Atlas mountains is one of the best astronomical site of the northern hemisphere. It benefits of about 250 clear nights per year.

Figure 3.4: TRAPPIST-N telescope at the Oukaïmeden Observatory (MPC Observatory code: Z53).

The Moroccan telescope is a twin of the Chilean one. The telescope designs and the mounts are essentially the same, the noticeable differences are in the camera characteristics and in the dome. The Johnson-Cousins filters B, V, Rc, Ic are the same than for TRAPPIST-S (Fig. 3.3). The camera of this telescope is an Andor IKONL BEX2-DD. The back-illuminated deep depletion CCD e2V chip of 2048×2048 pixels has a field of view of $20' \times 20'$ and can be cooled down to $-100\,°C$ below ambient temperature. The pixel size and scale are respectively of $13.5\,\mu m$ and 0.60 arcsec/pixels and the gain is 1.1 e/ADU. There are three possible read-out modes, 1MHz, 3 MHz, and 5MHz, corresponding to read-out noises of 7 / 12 / 32 electrons and read-out times of 5 / 3 / 1.8 seconds.
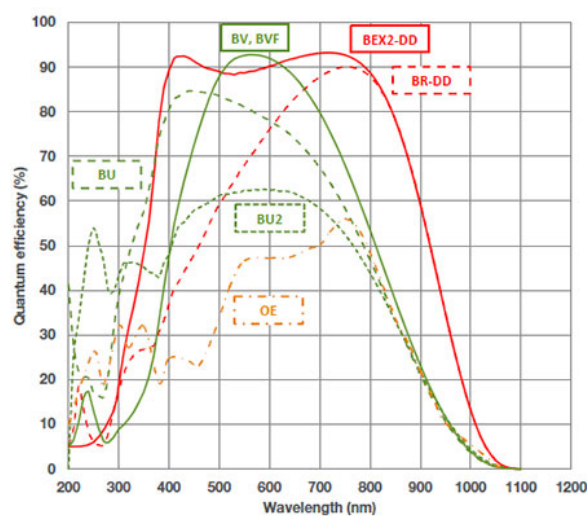

Figure 3.5: QE curve of the TRAPPIST-N CCD e2V chip with the extended coating in the blue (solid red curve BEX2-DD).

The TRAPPIST telescopes are entirely robotic and observations do not have to be done on site but the

counterpart is the requirement of a very robust design for every aspect of the observatory. They can be operated from anywhere via a Virtual Private Network (VPN), a secured internet connection. Observing plans consisting in text files are transmitted each night to the computer inside the dome and controlling the telescope. On this computer one of the main software handles every aspect of the observatory robotic operations. This includes scientific and calibration images acquisition, the focusing and astrometry, the telescope pointing and tracking, the filter wheel and the dome management. The mechanical operation can be supervised with webcams and microphones. A weather station and a rain sensor monitor the on site meteorological conditions in real time. The dome is closed and the telescoped placed in safe position automatically when rain/snow or clouds are detected, when the winds speed goes above 25 km/h or when the dew point is reached. A live feed of the inside and outside webcams and the meteorological conditions is accessible on the TRAPPIST operation webpage [4].

Table 3.1: Comparison of the characteristics of TRAPPIST-S and TRAPPIST-N.

	TRAPPIST-South	TRAPPIST-North
Site	La Silla Observatory (I40)	Oukaïmeden Observatory (Z53)
Altitude (m)	2315	2751
Latitude	29° 15′ 16.6″ (S) / 29.2546° (S)	31° 12′ 22″ (N) /31.2061° (N)
Longitude	70° 44′ 121.8″ (W) / 70.7394° (W)	7° 51′ 29″ (W) / 7.8664° (W)
Δ LAT - Δ LON - Baseline	60.4607° - 62.873° - 8618 km	
Telescope	Astelco RC Lightweight Telescope - Ritchey-Chretien - F/8 - 0.6 m - 75 kg	
Mount	Model: Astelco NTM-500 - Type: German equatorial Motors: direct drive systems - Drive accuracy: no periodic error Speed: up to $50\,°/s$ - Pointing accuracy: $5″$ Differential positioning accuracy: $< 1″$ RMS Tracking accuracy without autoguider: $1″/4\,min$	
Camera model	FLI ProLine PL3041-BB	Andor IKONL BEX2 DD
CCD type	Back-illuminated	Back Illuminated CCD Deep Depletion with fringe suppression Extended range dual AR coating
Array size (pixels)	2048×2048	2048×2048
Pixel size (µm)	15	13.5
Pixel scale (arcsecs/pixels)	0.64	0.60
Field of view	$22′×22′$	$20′×20′$
Full well (e)	100,000	100,000
Gain (e/ADU)	1.1	1.1
Peak QE (%)	96	90
Read-out modes (MHz)	1×1 / 1×2 / 2×2	1 / 3 / 5
Read-out noise (e)	9.5 / 14 / 14	7 / 12 / 32
Read-out time (s)	6 / 4 / 2	5 / 3 / 1.8
Dark current (e/s)	0.1	0.15 (at $-65\,°C$)
Cooling below ambient (°C)	-55.0 ± 0.1	-100.0 ± 0.1
Filter Wheel model	Double Apogee AI-FW50-10S	
Filters (wheel 1)	B, V, Rc, Ic, Sloan z, I+z', Exo (cut blue), NaI, H_2O^+	B, V, Rc, Ic, Sloan z, Exo (cut blue), NaI
Filters (wheel 2)	OH, NH, CN, C_3, CO^+, BC, C_2, GC, RC	OH, NH, CN, C_3, $H\alpha$, BC, C_2, GC, RC

[4] https://www.trappist.uliege.be/cms/c_3434181/en/trappist-live-trappist

Observations and data reduction

This section first describes the image acquisition process, then the basics of the data reduction are explained. Finally, details on differential aperture photometry are given.

4.1 Data acquisition for asteroids

The main targets of this work are large MBA, in order to provide additional data to the ESO Large Programme described in Sect. 2.5. We acquired data for 9 of these objects: (596) Scheila, (476) Hedwig, (89) Julia, (31) Euphrosyne, (24) Themis, (20) Massalia, (145) Adeona, (45) Eugenia and (22) Kalliope. In addition, we also observed four NEAs in support to high resolution radar observations of (3122) Florence, K17V12R, K18D01H and (3200) Phaethon. Observations took place from June 2017 to March 2018, with thousands of images taken on about 50 nights. To prepare the observations we first need to determine the visibility windows of each moving target. There are for instance the Horizons website (NASA/JPL, 2017a) or the method ViSiON provided by the webservice Miriade of the "Institut de Mécanique Céleste et de Calcul des Éphémérides" (IMCCE)[1]. ViSiON gives the length of the visibility windows according to observation criteria such as apparent magnitude or moon elongation and provides plots of the asteroids altitude and airmass during the night (Fig. 4.1). As our MBA targets are relatively bright ($m_V \sim$ 10 - 11), we can keep observing down to an airmass of $\sim$2.8 and we are not too sensitive to the moon illumination.

Before each night, observing plans have to be sent to the computers controlling the telescopes. They are text files that contain the informations on where, when and how to observe. An example is given on Fig. 4.2 for an observation of (89) Julia between 02:30 and 06:00 UTC, using the Rc filter, binning 1×1 and 15 seconds exposure time. The line number 9 contains the orbital elements of the target, used for the non-sidereal tracking. They are retrieved from the Minor Planet Center (MPC) website[2], the organism responsible for the designation of the minor bodies of the solar system and the collection of their orbits.

The observations sessions were planned in order to obtain the longest possible observing time by night and to have the largest coverage of the rotation curve. At the end of each night, a set of 7 flat-field frames by filters and by binning used are usually taken as well as 9 bias and dark frames. We mostly used the 1×1 binning, 1×1 MHz read-out mode and the Rc filter. In the case of (3200) Phaethon, we observed with the four B, V, Rc and Ic filters to investigate colour variations during its rotation. For the faint NEAs we used the 2×2 binning to increase the photometric sensitivity.

---

[1] http://vo.imcce.fr/webservices/miriade/
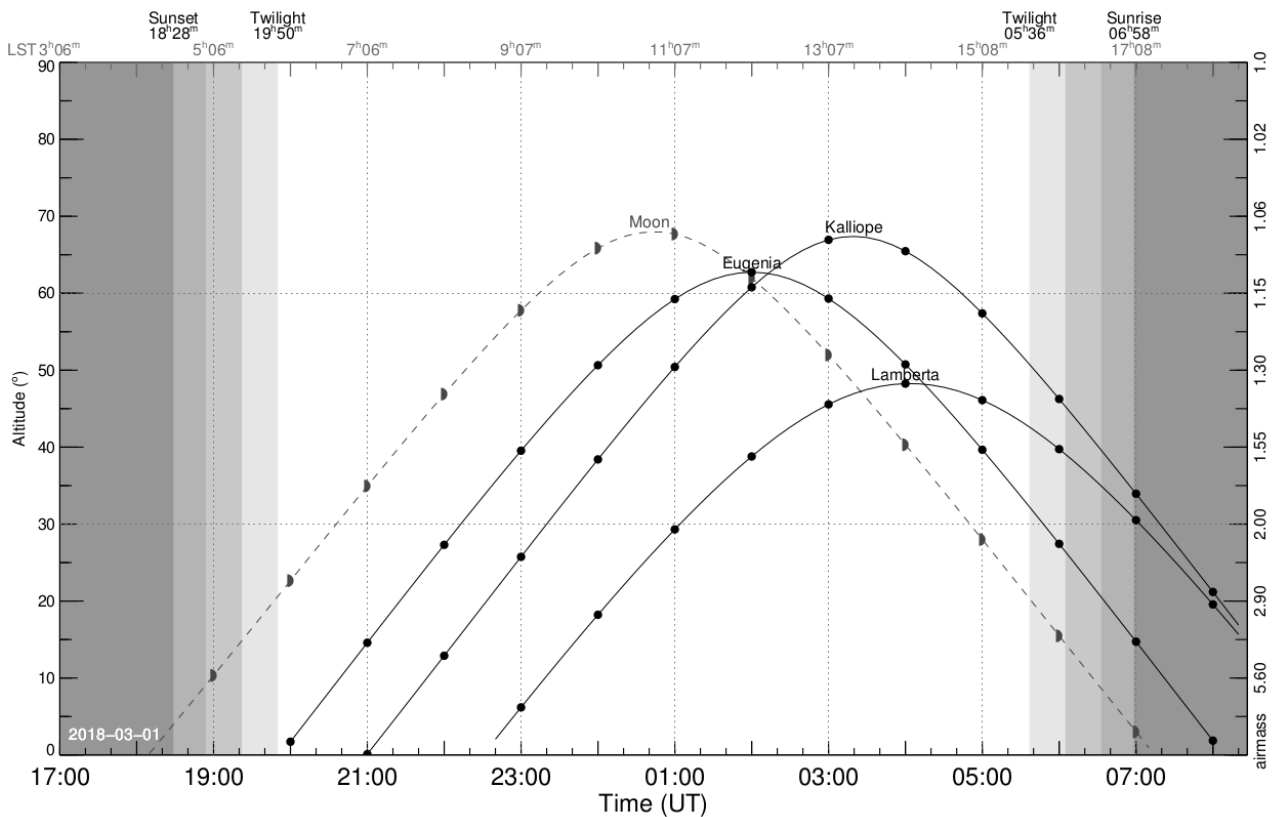[2] https://www.minorplanetcenter.net/iau/mpc.html

Figure 4.1: Example of visibility plot of (22) Kalliope, (45) Eugenia and (187) Lamberta on March 3, 2018, produced by ViSiON at VO-IMCCE – B. Carry (OCA) & J. Berthier (IMCCE).

```
 1 ; ==89 Julia==
 2 #waituntil 1, 02:30
 3 #autofocus
 4 #count 5000
 5 #binning 1
 6 #filter R
 7 #INTERVAL 15
 8 #trackon
 9 00089    6.60  0.15 K183N  40.58982   45.45240  311.55504   16.12653  0.1845785  0.24195335   2.5506349
   0 MPO439060  1865  61 1866-2018 0.53 M-v 38h MPCLINUX   0000    (89) Julia                20180209
10 #trackoff
11 #quitat 06:00
12 ;
```

Figure 4.2: Example of an observing plan.

4.2   Image calibration

There is no such things as a perfect instrument and so raw images cannot be directly used to do science. The recorded flux is affected by electronic and thermal noises and sensitivity to light that is different not only for each sensor but also from pixel to pixel. While these effects are not noticeable for daylight pictures, they become very important when the flux is much lower like it is usually the case in astronomy and for accurate flux measurements. It is therefore essential to perform an adequate image calibration to remove at best these defects and it is mandatory to obtain accurate photometric measurements. This calibration is done for all light images in three steps, the bias and dark subtraction and the flat-field division. The principle of these steps will be discussed in the following. An example of the result of an image calibration is shown in Fig 4.3. The pixel to pixel variations have been reduced and dust shadows and brightness variation across the image removed.

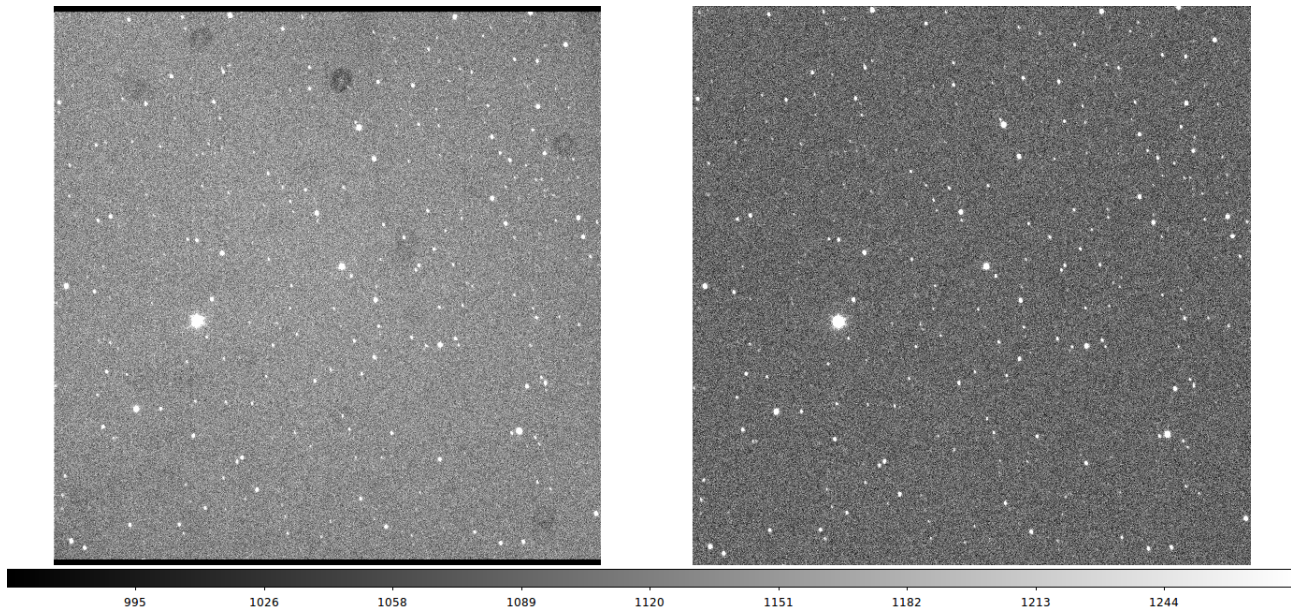There are numerous softwares to perform such calibration. However when large numbers of images from

Figure 4.3: Comparison of the same image before and after the calibration process.

different night are obtained it is more convenient to automate as much as possible this process. For this work all calibration images have been done with previously written scripts that make use of IRAF tasks. IRAF (Image Reduction and Analysis Facility [3]) is a collection of tasks allowing to do various operations on astronomical data. The scripts also make use of the power of the FITS (Flexible Images Transport System) format, a standard digital file format in astronomy. In addition to the normal data, these files contain metadata that describe the images in a header. In the header can be found information like the type of image (light, dark ...), the exposure time, the binning used, the target name and its coordinates and much more.

4.2.1 Bias subtraction

When taking a frame with a zero-length exposure and the shutter closed, a so called "bias frame" (Fig. 4.4), we would expect to read a null signal for all pixels. In fact we will record mostly the bias, an electronic offset signal that can vary across the image. The bias is more or less constant from image to image except for a small readout noise of a few electrons produced when the pixels are read. A "master bias" is produced by averaging a number of bias frames together using the *zerocombine* task of IRAF in order to reduce the noise. Bias frame calibration can then be done by subtracting the master-bias to the light images but also to the "dark" and "flat-field" frames.

Due to the zero-length exposure, bias frames are easy to acquire. For each night, 9 such frames were taken for a given binning.

4.2.2 Dark subtraction

During a CCD exposure a so called "dark current" (because it builds up with no light) is produced and added to the signal. The dark current is related to the thermal noise and accumulates linearly with time on pixels. It can be minimised by cooling the camera sensor but it does not completely suppress it. As each pixel has a different dark current some pixels will accumulate thermally excited electrons faster, they are called "hot pixels". This dark current and the hot pixels can be removed by subtracting a dark frame (Fig. 4.4). "Dark frames" are images
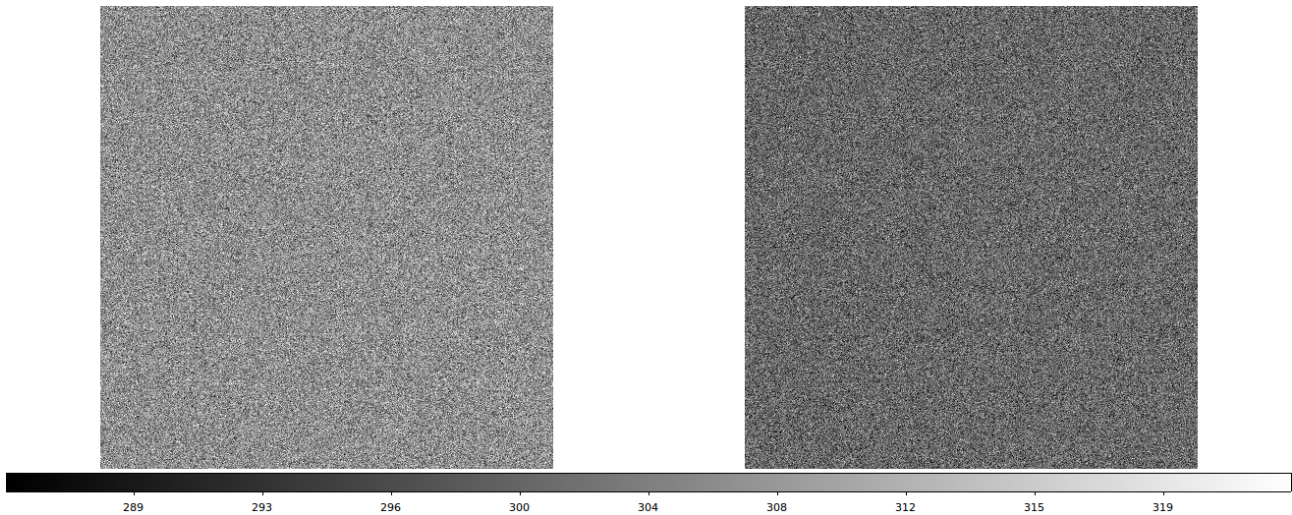
---

[3]http://iraf.noao.edu/

Figure 4.4: *Left:* Master bias in binning 1x1 created with the IRAF task *zerocombine*. *Right:* Master dark frame in binning 1x1 created with the IRAF task *darkcombine*.

taken with the shutter closed in order to only record the dark current. Ideally they should be taken with the same temperature and with the same exposure than the light images. The TRAPPIST camera are cooled to a constant temperature and dark frames with exposure matching those of light frames are normally taken each night. If not, images are calibrated using a dark frame scaling. The rate of dark current is constant for a given pixel but the thermal excitation is still a random process. Because of this random noise, subtracting a dark frame will improve the hot spots problem but unfortunately also add noise to the image (readout plus dark current noise). Subtraction of a single dark frame will increase the random noise by 41%. Like for the master-bias it can be improved by averaging a large number N of dark frames together because it reduces the noise contribution by a factor $\sqrt{N}$. Therefore, a "master dark" combining 16 dark frames will only increase the noise on the image by 10%. Closing the shutter prevent light to reach the sensor but not cosmic rays, which can produce little streaks or spots of bright pixels. Those outlier pixels will biased the value of the average when combining the dark frames together to create the master-dark. This is why a sigma-clip, an average of only the values close enough to the median, is used instead.

4.2.3 Flat division

The "flat-field" calibration aims to correct for the pixel to pixel variation in sensitivity and is very important for accurate photometry. The first source of flat-fielding variation is inherent to the CCD manufacturing because pixels cannot be made perfectly identical. Moreover, dust can reach the surface of the sensor or the camera window and cast shadows looking like donuts. In addition, vignetting in the optical system can result in darker edges of the science image. To compensate for these effects, images of uniform (flat) fields are taken. This way only light sensitivity variations across the image appear. Flat-field frames are usually taken by observing the sky at twilight or dusk, when it shows a very uniform glow. Some bright stars can still be visible, but as the telescope pointing is offsetted between each exposure, it will be at different positions on successive images and so the stars can be removed when combining flat-field frames together using a median pile. Flat-field frames must be first bias and dark subtracted and normalized by their median pixel values to compensate for different sky brightnesses and exposures. Unlike bias and dark frames, flat-field frames are filter dependent (Fig. 4.5). Sigma clipping is used to combine flat-field frames together to reduce the noise and remove the outlier pixels (cosmic

rays, stars ...). All light images are then divided by the adequate "master flat-field", removing the sensitivity variations as illustrate in Fig. 4.3.
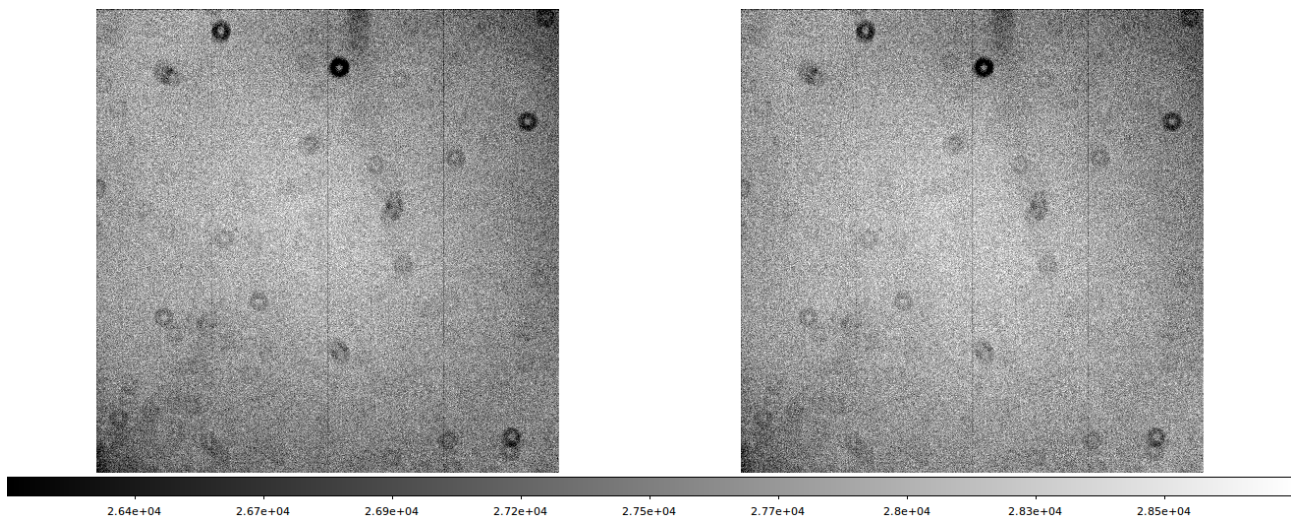

Figure 4.5: Master flat-field frames with a Rc (left) and V (right) filter.

4.3 Photometry

Once the images have been calibrated, they are ready for the photometric measurements. The measurements are done using aperture photometry, as described in Sect. 2.2. The target's flux is taken as the total flux in a measuring aperture, normalised to an exposure of 1 second, and subtracted of the sky background. Fig 4.6 illustrates the measuring aperture and the sky background annulus. The size of the measuring aperture has to be adequate regarding the size of the target's point spread function (PSF). It should be large enough to get all the flux of the target but a too large aperture will result in a lower signal to noise ratio (SNR). The SNR is the ratio between the useful signal over the total signal (target + noise). The higher the SNR the better will be the accuracy of the measurement. In practise the aperture size should be 2 or 3 times the average FWHM of several well exposed stars. Even if dark and flat corrections are applied, the sky background has to be subtracted, as the sky itself is never totally dark. This value is taken as the median or clipped-average of the flux in an annulus centred on the target and separated from the measuring aperture by a dead zone to avoid any flux from the target to be taken into account.

The photometric measurements are done for the target and a certain number of comparison stars. It is done with a collection of previously written IRAF and bash scripts. As asteroids are moving targets on the plane of the sky, a script retrieves the ephemerids of the asteroid at the time of observations on the NASA/JPL Horizons website. The asteroid coordinates are converted in position in pixels for each images. Then an IRAF task determines the centroid of the asteroid's profile and the aperture measurement is done. All the stars on the image that are not saturated and with a high enough SNR are also measured. For each image, a file with the brightness measurements of the asteroid and all the detected stars is created with each stars being assigned an identification number.

When all brightness measurements are done, the set of comparison stars that will be used has to be determined. The most direct way is to first select the stars that have been measured on every images. This can results in just a few stars or up to a few hundreds for crowded fields. Then, an inspection of the flux of these stars is done and
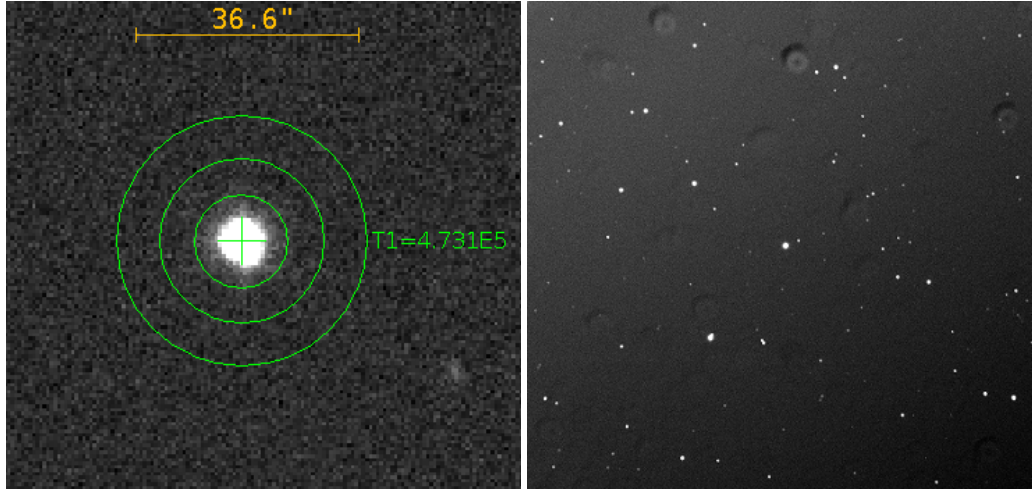
Figure 4.6: *Left:* Illustration of the measuring aperture used to compute the flux of an object (here (24) Themis) and the annulus used to estimate the background flux. *Right:* Flux variations that can be caused by the light of the Moon when close to the asteroid and at high illumination.

only the stars with a flux stable during the observations are kept. If the time of observation and /or the asteroid apparent velocity is small, a large number of comparison stars should be obtained. If the observed field change during the observations, as when observing NEAs, the data is split on two or more sets, with their own sets of comparison stars. A correction is then applied when merging the data to account for the different average flux of each sets of comparison stars. When the moon illumination is high and the separation with the asteroid is small, the light of the Moon can cause a flux gradient across the frames and cast the shadows of the dusts present on the CCD window. This makes "donuts" shapes appear on the images (Fig. 4.6), like those on flat-field images but here they cannot be totally corrected. It is not a problem for the asteroid as it is tracked by the telescope. The stars however drift slowly across the frames and their brightnesses could be affected by the shadows. In this case, particular attention on the examination of the comparison stars lightcurves must be taken to keep only the unaffected stars.

At this stage differential photometry can be executed. The asteroid differential flux is obtained by dividing the raw flux by the total flux of the comparison stars for each measurement. The flux is then normalised by its average.

The error on the flux for each measurement is given by

$$n_{pix} = \pi \times A^2$$

$$F_C = F_{C1} + F_{C2} + ...$$

$$sc = \frac{(0.09 \times D^{-2/3} \times X^{1.75} \times e^{-H/8000})}{\sqrt{2 \times t_{exp}}}$$

$$N_T = F_T + (F_T \times sc)^2 + n_{pix} \times (bg + RON^2)$$

$$N_C = F_C + (F_C \times sc)^2 + n_C \times n_{pix} \times (bg + RON^2)$$

$$\sigma = \sqrt{\frac{N_T}{F_T^2} + \frac{N_C}{F_C^2}}$$

where A is the aperture size (pixels), t_{exp} is the exposure time (s), bg is the the background noise (e), X is the airmass, H the altitude of the observatory (m), D the telescope diameter (cm), RON is the read-out noise

(e), sc is the scintillation, n_C is the number of comparison stars, F_C is the total flux of the comparison stars and F_T is the target flux.

In order to normalise the time of observations between different observers, that can be at different distances of the asteroid at a given time, the epochs have to be *light-time corrected*. The time associated to each measurement is then taken as the time at which the detected photons left the surface of the asteroid. Again, a request to the JPL Horizons website is needed to retrieve the distance to the asteroid. The time of travel of the light is computed and subtracted to the time of observation.

To fold a lightcurve on its rotation period it can be necessary (generally for NEAs) to correct for potential trend in the lightcurves due to changes in the apparent magnitude of the asteroid during the night. It can be done by dividing the asteroid flux by the magnitude variation, retrieved on ephemerids services.

To put the data in the format used by DAMIT, the service compiling asteroid shape models, the ecliptic asteroid-centric cartesian coordinates x, y, z of the Sun and of the Earth in au at the epochs of observation are needed. These coordinates are used by the lightcurve inversion algorithm to reconstruct asteroids shape models. They can be retrieved using the *ephemcc* method of the Miriade service of the IMCCE[4].

When the rotation coverage is sufficient, the data can be fitted by a Fourier expansion for a given number of Fourier modes, which directly gives the lightcurve amplitude. The order of the fit is taken as the lowest that satisfactorily fit the data. In practise, the order is incremented until the RMS of the residuals levels out. The fit is done with the *MultiTermFit* function of the python library *astroML*.

---

[4] http://vo.imcce.fr/webservices/miriade/?ephemcc

Results

In this chapter the results of our observations will be presented. The first section is dedicated to the 9 large MBAs that we observed to support the modelling effort of the ESO Large programme presented in Sect. 2.5. The second section is dedicated to the observations of the close approach of three NEAs. Those are (3122) Florence (D $\sim$ 4 km) which is known since 1981, and two smaller ones discovered in 2017 (K17V12R) and 2018 (K18D01H). The last section focus on (3200) Phaethon, another NEA that we observed during eight nights with TRAPPIST-N in December 2017.

5.1 ESO Large Programme targets

5.1.1 (596) Scheila

The first asteroid we observed is Scheila, a main-belt asteroid of 160 ± 1 km in diameter with a geometric albedo of 4%, according to the NASA/JPL Small-Body Data Browser[1] (SBDB) (NASA/JPL, 2017b).

On December 2010, an outburst was detected by the Catalina Sky Survey and the asteroid exhibited a comet-like appearance (Fig. 5.1). It was thought that Scheila could actually be a Main Belt Comet (MBC). MBCs are bodies orbiting inside Jupiter's orbit like MBAs but that most probably undergo water ice sublimation when approaching perihelion (Hsieh and Jewitt, 2006). However, using follow-up observations with the Hubble Space Telescope, Jewitt et al. (2011) explained this behaviour by an impact with a $\sim$35 m asteroid. The dust coma faded quickly and Scheila returned to a star-like appearance.

We observed Scheila on June 2 and 3, 2017. After cleaning of the data due to some clouds during the first night, we obtained an almost full coverage of the phased lightcurve. We used the rotation period P = 15.793 $\pm$ 0.005 h from Warner (2017) because we did not have enough data to confidently determine a new period. At around 0.4 of the rotational phase, the data of the first night are more dispersed due to higher airmass and unstable atmospheric conditions (Fig. 5.2). Except for this part of the curve, the quality of the lightcurve is good and the residuals of the fit are low.

The amplitude of the lightcurve, estimated with a fit by a 7th order Fourier series, is low (A = 0.071 $\pm$ 0.004 mag). Large asteroids usually have relatively low lightcurve amplitudes as they are generally not very elongated due to their own gravitational attraction. Moreover, in this case the aspect angle (the angle between the spin axis and the line of sight) was of $156°$ (Fig. 5.1), meaning that the asteroid was seen almost pole-on. Therefore the same side of Scheila was seen throughout its rotation, limiting brightness variations. A convenient way to
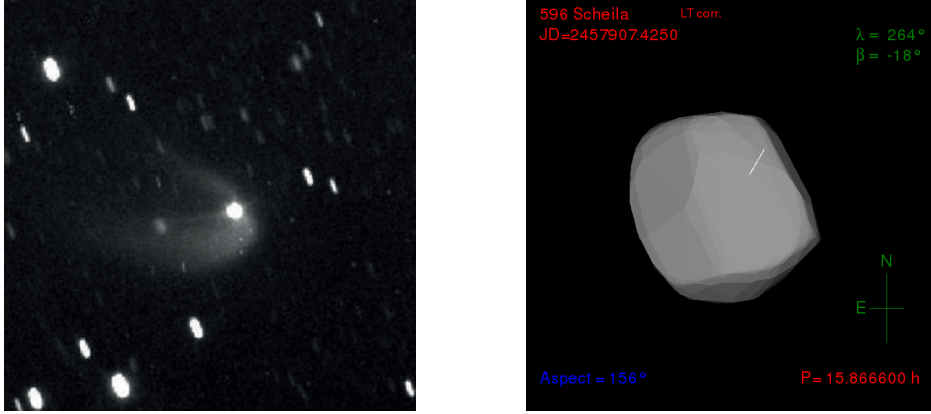
---

[1] https://ssd.jpl.nasa.gov/sbdb.cgi

Figure 5.1: *Left*: Image of the outburst of (596) Scheila taken by TRAPPIST-S on December 18, 2010 (Jehin et al., 2011a). *Right*: Shape model and orientation of (596) Scheila on June 2, 2017. Source: Interactive Service for Asteroid Models (ISAM).

Table 5.1: Summary of (596) Scheila observations.

(596) Scheila - $P \simeq 15.8$ h						
Date	Julian date	Telescope	Filter	Phase angle (°)	Duration (h)	Number of images
2017-06-02	7907	TS	Rc	1.3	7.2	601
2017-06-03	7908	TS	Rc	1.7	9.8	741
Total					17.0	1342

check the orientation of an asteroid at a given epoch is provided by the Interactive Service for Asteroid Models (ISAM) [2], presented in Marciniak et al. (2012). Among other things this website can be used to display an available asteroid shape model on the plane of the sky for a given date, as in Fig. 5.1. The spin axis is represented by a straight white line and the aspect angle is given.

5.1.2 (476) Hedwig

The second MBA we observed is (476) Hedwig which has a diameter D $\sim$ 140 km and and albedo $p_V \sim 0.035$ (NASA/JPL, 2017b). The observations took place at the end of June and the beginning of July, spread on four nights. Despite a substantial total observation duration of 17 hours, the rotation was not fully covered. Indeed, Hedwig is a slow rotator with a rotation period of 27.246 ± 0.005 h (Marciniak et al., 2015). The resulting composite phased lightcurve is presented in Fig. 5.3. We do not have a full coverage but our data will be combined with those of other observers to be used in the multiple data sources modelling of the ESO LP.

Table 5.2: Summary of (476) Hedwig observations.

(476) Hedwig - $P \simeq 27.2$ h						
Date	Julian date	Telescope	Filter	Phase angle (°)	Duration (h)	Number of images
2018-06-18	7923	TS	Rc	6.6	8.5	576
2018-06-28	7933	TS	Rc	6.0	0.6	46
2018-07-09	7944	TS	Rc	1.5	6.0	403
2018-07-11	7946	TS	Rc	4.6	1.7	153
Total					16.8	1178

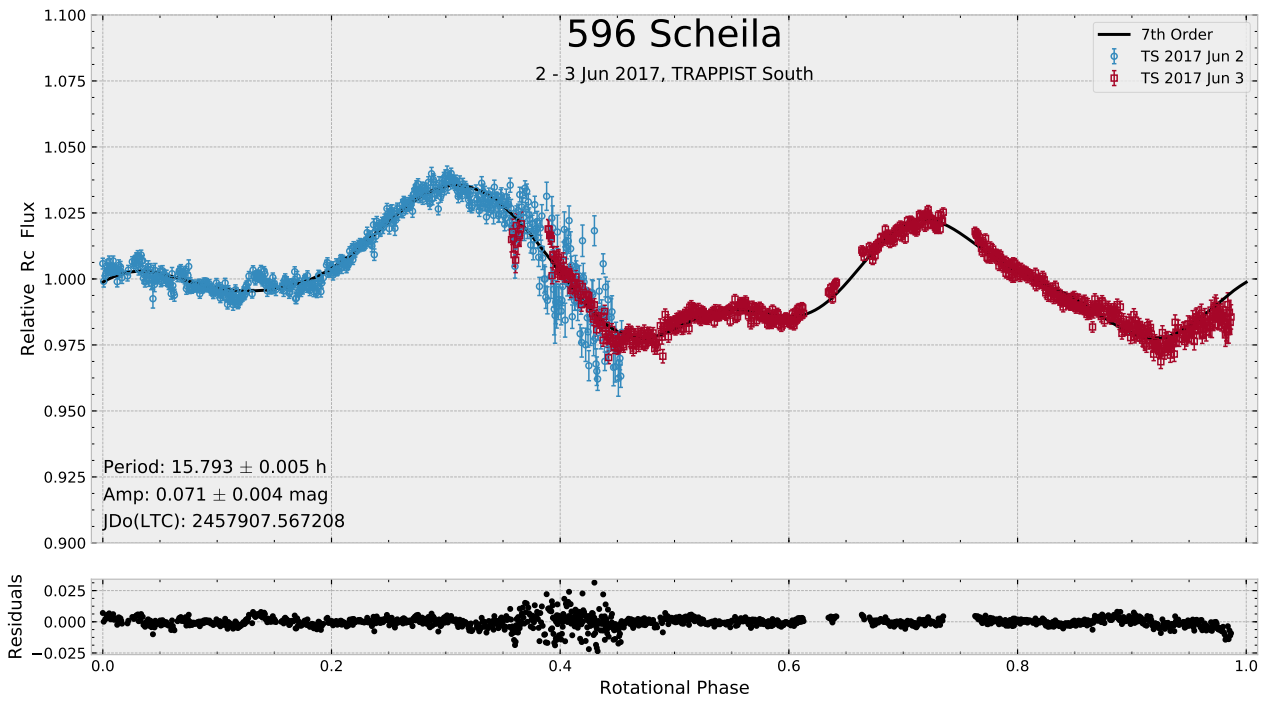[2] http://isam.astro.amu.edu.pl/
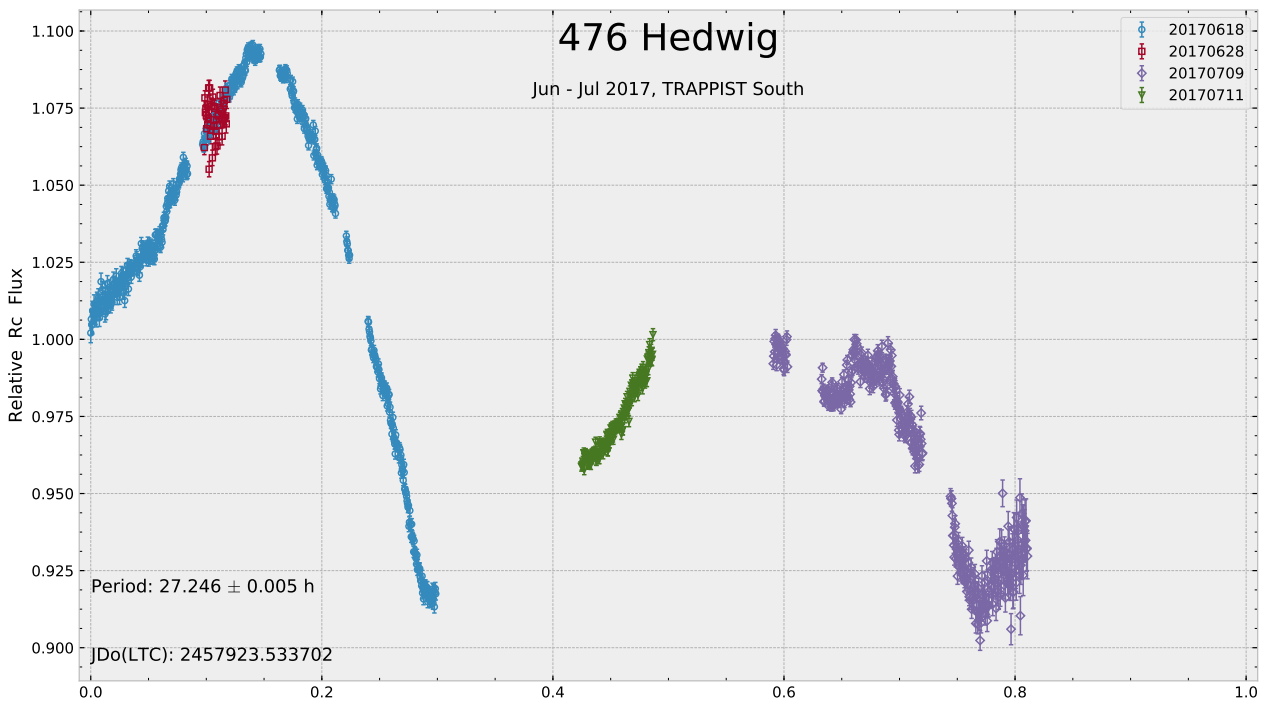
Figure 5.2: Phased lightcurve of (596) Scheila.

Figure 5.3: Phased lightcurve of (476) Hedwig.

5.1.3 (89) Julia

Julia is an S-type asteroid that has already been studied a lot in the past as it was a potential flyby target for the ESA Rosetta mission, but was ultimately not selected. Birlan et al. (2004) acquired its near-IR spectrum and an equatorial diameter of 130 ± 15 km was determined by AO observations (Durech et al., 2010). Moreover, multiple stellar occultations by Julia were observed. Adaptive optics observations as part of the ESO LP have already been carried out and the resulting images and shape model are shown in Fig. 5.4.
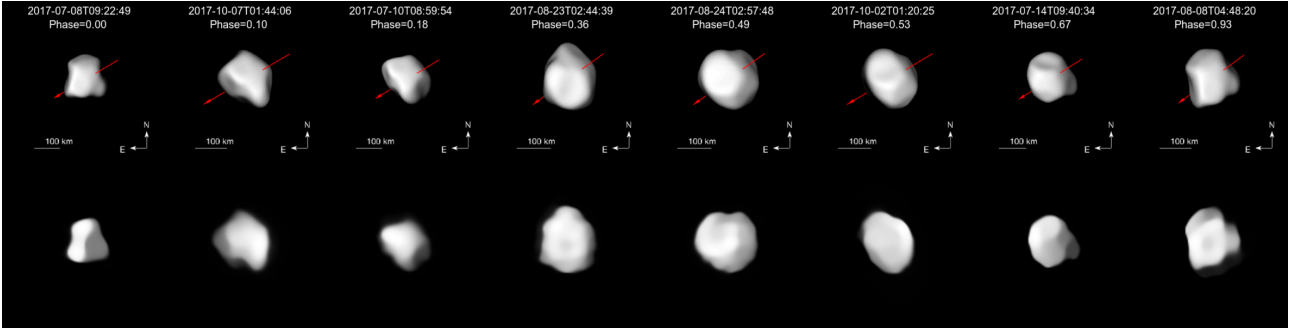
Figure 5.4: Comparison between the shape model (top) and deconvolved adaptive optics images of (89) Julia at increasing rotational phase (Vernazza et al., 2018).

We extensively observed Julia with TRAPPIST-S (4 nights in September 2017 with a V filter) and TRAPPIST-N (4 nights in November and December 2017 with a Rc filter). The total duration of the observations is 32.2 hours and the rotation is covered several times at almost all rotational phases. The resulting phased lightcurve (Fig. 5.5) is very dense (4457 individual measurements).

Table 5.3: Summary of (89) Julia observations.

(89) Julia - $P \simeq 11.4$ h						
Date	Julian date	Telescope	Filter	Phase angle (°)	Duration (h)	Number of images
2017-09-20	8017	TS	V	11.4	3.4	553
2017-09-21	8018	TS	V	11.7	3.4	537
2017-09-22	8019	TS	V	12.1	3.6	619
2017-09-30	8027	TS	V	15.0	4.0	726
2017-11-27	8085	TN	Rc	27.6	5.1	522
2017-12-02	8090	TN	Rc	27.8	4.6	478
2017-12-07	8095	TN	Rc	27.9	4.1	604
2017-12-23	8111	TN	Rc	27.5	4.0	418
Total					32.2	4457

With this large data set we used the FALC method of the software Peranso (see section 2.3) to determine a rotation period. We found a period of P = 11.3844 ± 0.0002 h (Fig. 5.6), which is consistent with other values of the literature (e.g. P = 11.3831 ± 0.0005 h from Warner (2018b)). The lightcurve presents a deep minimum and the 8th order Fourier fit gives an amplitude A = 0.187 ± 0.012 mag.

The first results of the ESO LP survey concerning Julia are presented in Vernazza et al. (2018) for which the TRAPPIST data were used. In this paper, they challenged the recent proposition that Julia is the parent body of a small family of 33 known asteroids originating from a cratering collisional event (Nesvorný et al., 2015). They used their disk-resolved images recently acquired with SPHERE at the VLT, the already available shape model on DAMIT (Durech et al., 2010) as well as the new optical lightcurves. With their new shape model and
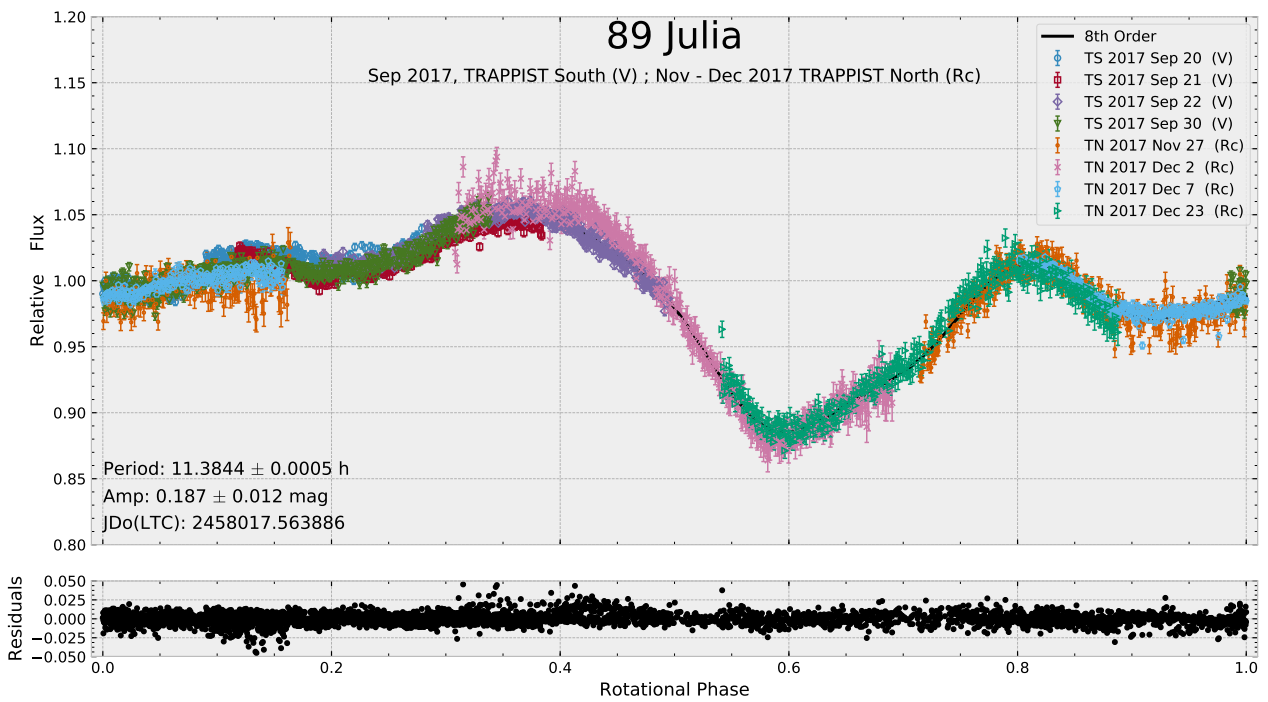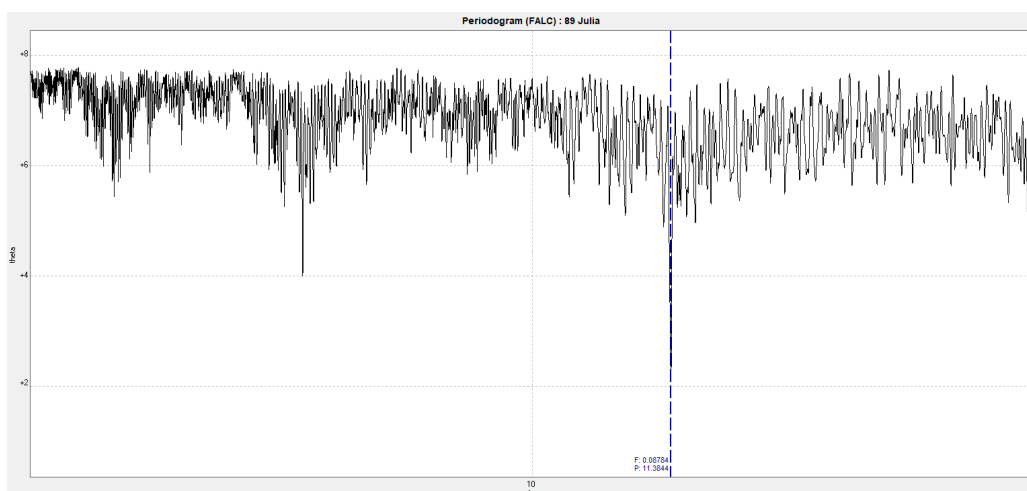
Figure 5.5: Phased lightcurve of (89) Julia.

Figure 5.6: Period spectrum of (89) Julia with the FALC method.

numerical simulations they confirmed that Julia was impacted 30 to 120 Myr ago by a D ∼8 km asteroid that created a ∼60 km crater, most likely in the southern hemisphere. They did a reconnaissance and characterisation of the largest craters at the surface of Julia and found one such crater (D ∼75 km) in Julia's southern hemisphere.

5.1.4 (24) Themis

This large asteroid of D ∼200 km (NASA/JPL, 2017b) orbits in the outer part of the MBA and has a C/B spectral type. It is the main body of the Themis family, a group of more than 500 asteroids sharing similar semi-major axes (3.08 au $\leq a \leq$ 3.24 au), orbital eccentricities (0.09 $\leq e \leq$ 022) and inclinations ($i < 3°$).

We have again gathered a large amount of data on this asteroid. We observed it during 7 nights with TRAPPIST-S (in September and November 2017) and one night with TRAPPIST-N. On November 8, Themis was first observed with the Moroccan telescope followed on the same night by the Chilean one. This allowed to gather a very long session of 10.3 hours of continuous observation (longer than the rotation period), with an overlap of about 2.5 hours of both telescopes (Fig. 5.7).

Table 5.4: Summary of (24) Themis observations.

Date	Julian date	Telescope	Filter	Phase angle (°)	Duration (h)	Number of images
(24) Themis - P ≃ 8.4 h						
2017-09-20	8017	TS	Rc	9.6	3.2	255
2017-09-21	8018	TS	Rc	9.4	3.4	315
2017-09-22	8019	TS	Rc	9.1	3.4	308
2017-09-23	8020	TS	Rc	8.8	3.8	362
2017-11-07	8065	TS	Rc	6.7	7.0	698
2017-11-08	8066	TS	Rc	7.0	7.0	698
2017-11-08	8066	TN	Rc	7.0	6.7	628
Total					34.5	3264

With the 8 nights, the total duration of observation is 34.5 hours, which results in a very dense sampling of the rotation with 3264 points (Fig. 5.8). The lightcurve exhibits a complex shape and a 13th order Fourier series was needed to fit it. The lightcurve amplitude is A = 0.131 ± 0.006 mag.

The period we derived is P = 8.3744 ± 0.0003 h (Fig. 5.9), in good agreement with other studies (e.g. P = 8.374187 h, Viikinkoski et al. (2017)).

5.1.5 (31) Euphrosyne

Euphrosyne is the 5th most massive asteroid of the MBA after (1) Ceres, (4) Vesta, (2) Pallas and (10) Hygiea. It has a diameter of about 267 km, belongs to the C spectral type (NASA/JPL, 2017b) and gave its name to the Euphrosyne family.

Observations were conducted during four nights in November and December 2017 with the Rc filter, for a total of 15 hours. Euphrosyne has been reported multiple times to have a period of about 5.5 hours (e.g. P = 5.529597 h, Hanuš et al. (2016b)). Our observations covered completely the rotation curve, for which we used 1841 individual measurements. The lightcurve is fitted by a 5th order Fourier series and we found a small amplitude A = 0.071 ± 0.006 mag.

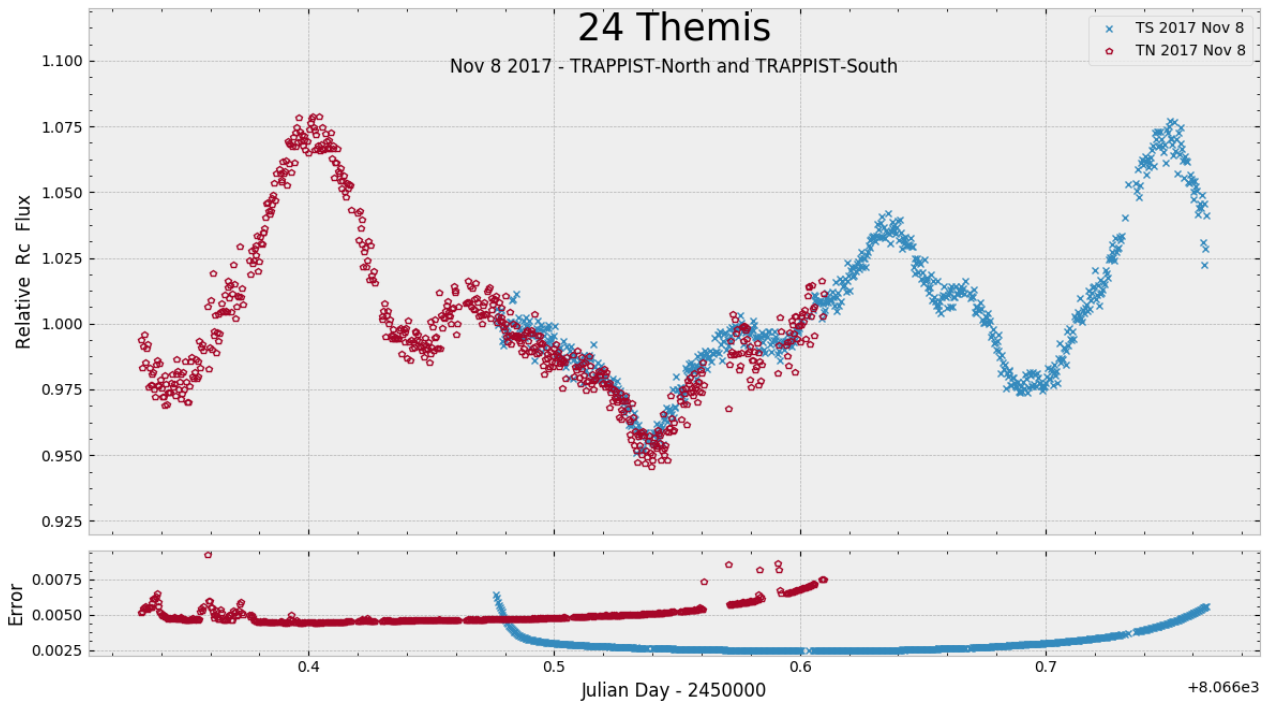Our period estimate is P = 5.5312 ± 0.0010 h (Fig. 5.11).

Figure 5.7: Lightcurve of (24) Themis the night of November 8, 2017 taken with TRAPPIST-N and TRAPPIST-S.
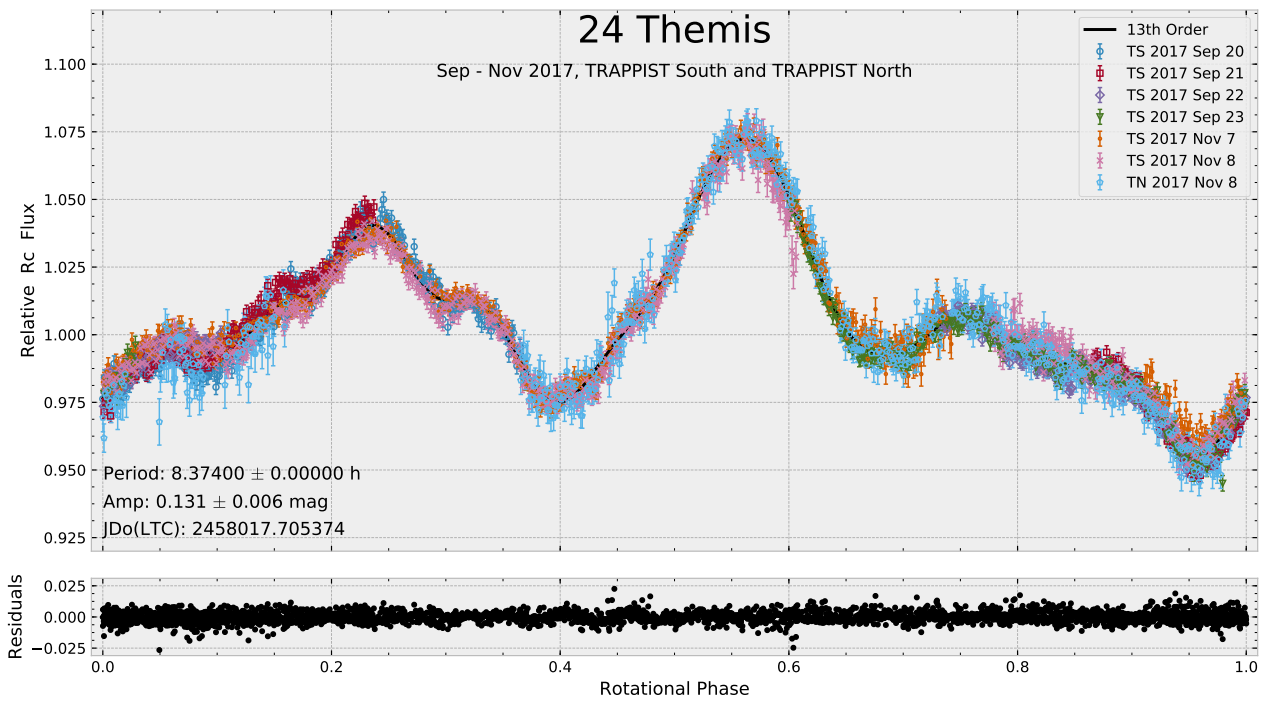

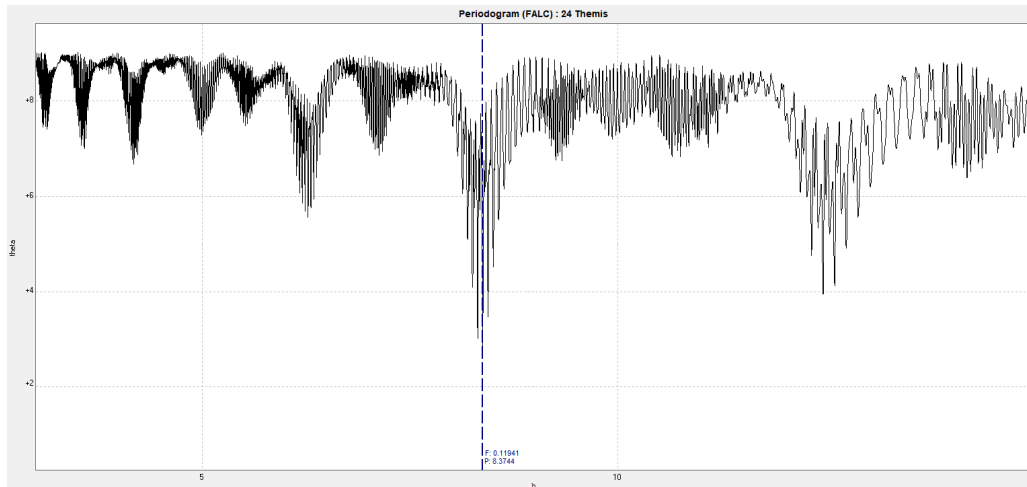Figure 5.8: Phased lightcurve of (24) Themis.

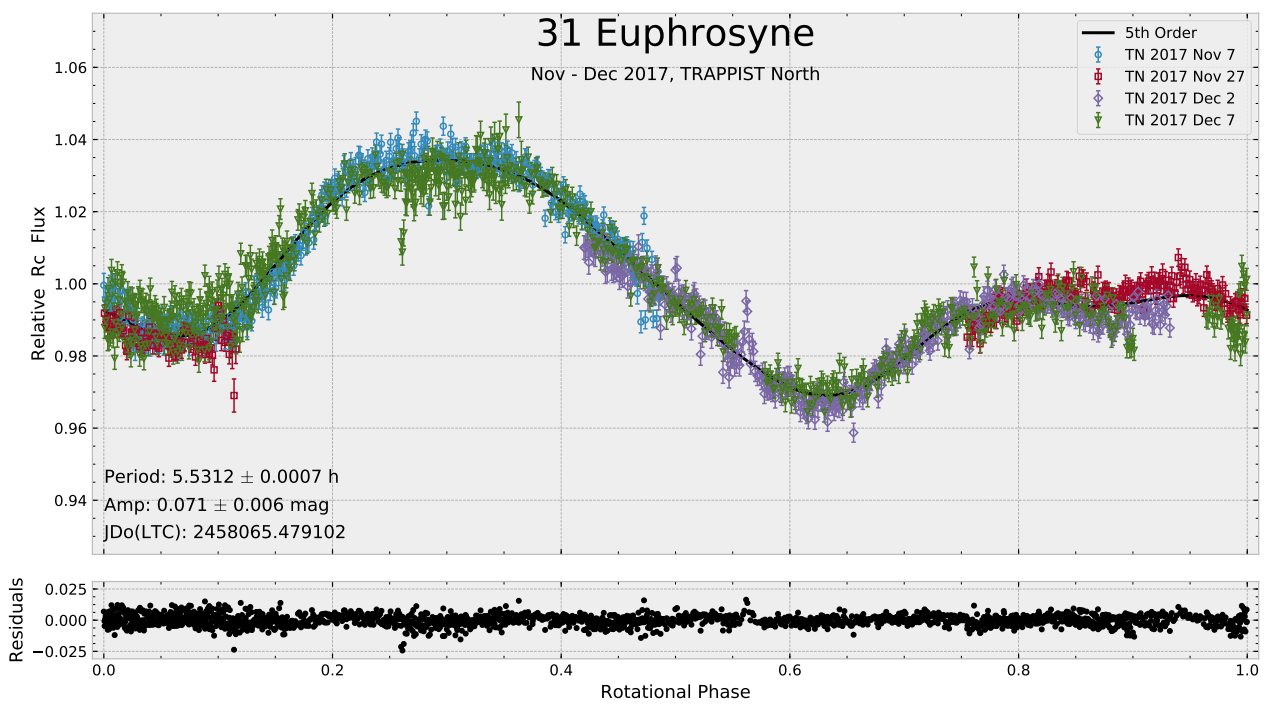Figure 5.9: Period spectrum of (24) Themis with the FALC method.

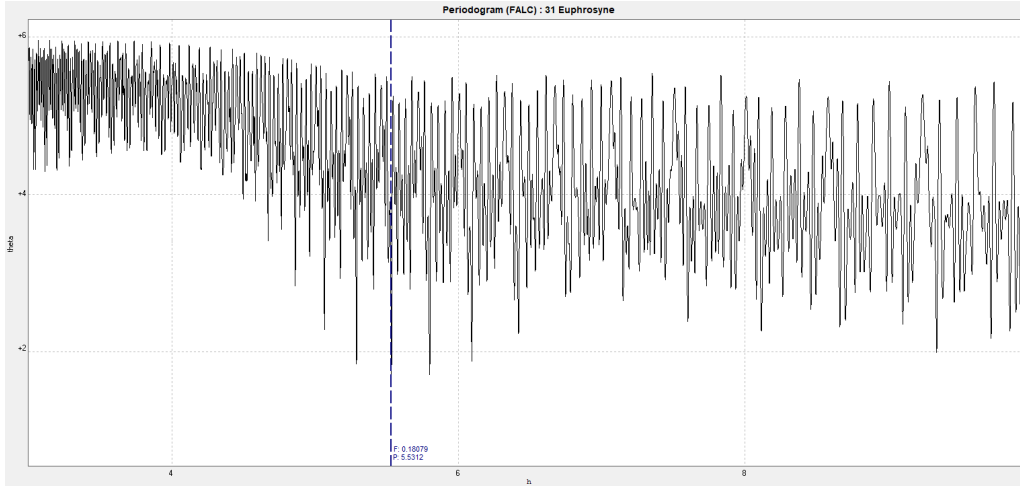Figure 5.10: Phased lightcurve of (31) Euphrosyne.

Figure 5.11: Period spectrum of (31) Euphrosyne with the FALC method.

Table 5.5: Summary of (31) Euphrosyne observations.

(31) Euphrosyne) - P $\simeq$ 5.5 h						
Date	Julian date	Telescope	Filter	Phase angle (°)	Duration (h)	Number of images
2017-11-07	8065	TN	Rc	19.8	2.4	359
2017-11-27	8085	TN	Rc	16.3	2.2	261
2017-12-02	8090	TN	Rc	15.5	2.8	365
2017-12-07	8095	TN	Rc	14.8	7.8	864
Total					15.2	1849

5.1.6   (20) Massalia

Massalia is a stony asteroid of the inner belt with a diameter of D = 136 $\pm$ 4 km and albedo of p_V = 0.241 $\pm$ 0.018 (NASA/JPL, 2017b). It is the parent body of the Massalia family, a group of stony asteroids originating from a collisional event at the surface of Massalia.

Our observations of Massalia are spread from 2017 November 10 to December 8, during five nights with both TRAPPIST-N and TRAPPIST-S using the Rc filter. Due to its size, albedo, and location in the inner part of the MBA, Massalia was very bright (8.7 $\leq$ m_V $\leq$ 9.5). Hence, we had to observe out of focus in order to spread the flux on a larger area to avoid pixel saturation and then to use an adequate aperture size for the photometric measurements.

As for Themis, we used both TRAPPIST telescopes to observe Massalia on November 10 and 18, resulting in two observing runs of almost 10 hours, i.e. longer than the rotation period of about 8.1 hours (e.g. P = 8.097714 h, Kaasalainen et al. (2002b)).

In total we observed during 24.7 hours and the phased lightcurve use 3245 individual measurements (Fig. 5.12). We derived from our data a period P = 8.0978 $\pm$ 0.0002 h with the ANOVA method of Peranso (Fig. 5.13), consistent with previous studies. The amplitude A = 0.257 $\pm$ 0.006 mag is rather large for such a big body, and the shape model of Massalia available on the DAMIT database (Durech et al., 2010) reveals a somewhat elongated shape.
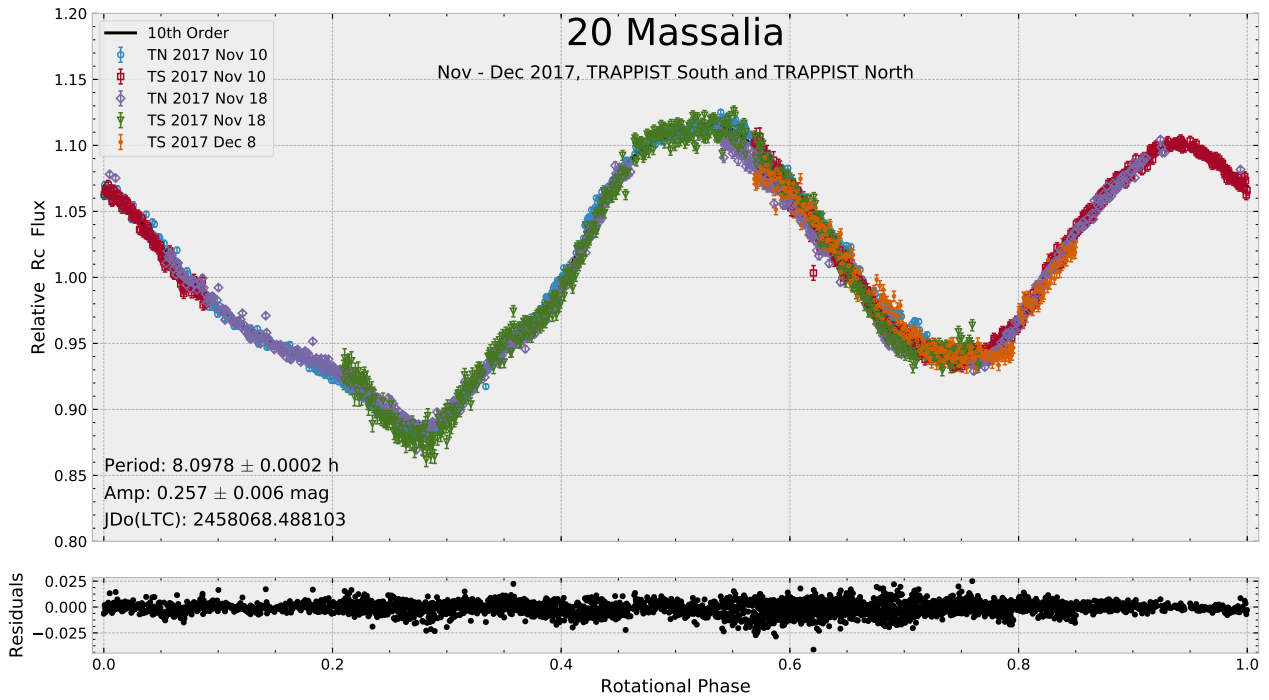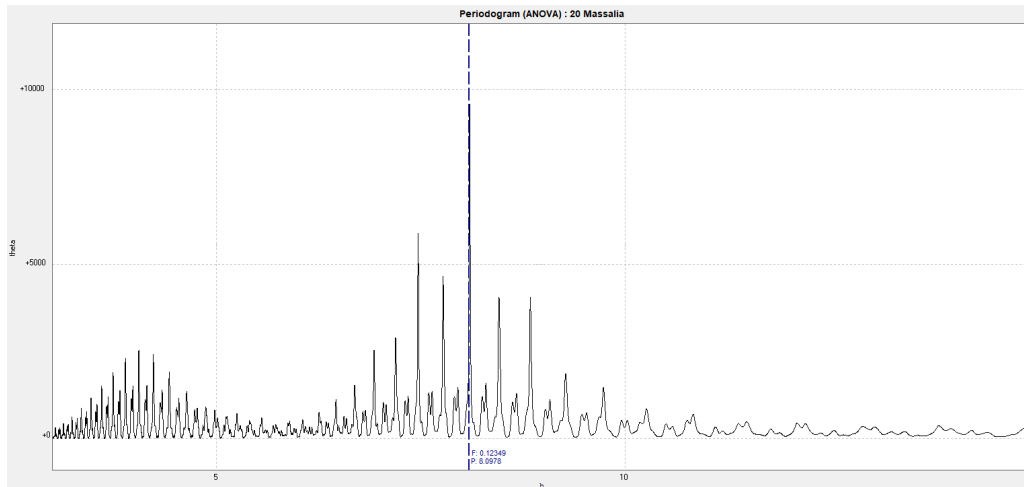
Figure 5.12: Phased lightcurve of (20) Massalia.

Figure 5.13: Period spectrum of (20) Massalia with the ANOVA method.

Table 5.6: Summary of (20) Massalia observations.

(20) Massalia - P $\simeq$ 8.1 h						
Date	Julian date	Telescope	Filter	Phase angle (°)	Duration (h)	Number of images
2017-11-10	8068	TN	Rc	18.8	5.9	600
2017-11-10	8068	TS	Rc	18.8	4.2	729
2017-11-18	8076	TN	Rc	15.5	7.7	700
2017-11-18	8076	TS	Rc	15.5	4.5	783
2017-12-08	8096	TS	Rc	5.3	2.4	433
Total					24.7	3245

5.1.7 (145) Adeona

Adeona is a C-type MBA. It is the parent body of the Adeona family and its diameter is 151 ± 18 km, as measured from radar observations with the Arecibo Observatory (Magri et al., 2007).

We observed (145) Adeona with TRAPPIST-N using the Rc filter. The observations have been carried out during 4 nights in February and March 2018 for a total of 28.5 hours, achieving an almost complete coverage of the rotation (Fig. 5.14). The small amplitude of 0.065 ± 0.007 mag is explained by the longitude of $122°$, relatively close to the rotational pole. The fit uses a 6th order Fourier series and results in a rms residuals of 0.004 mag.
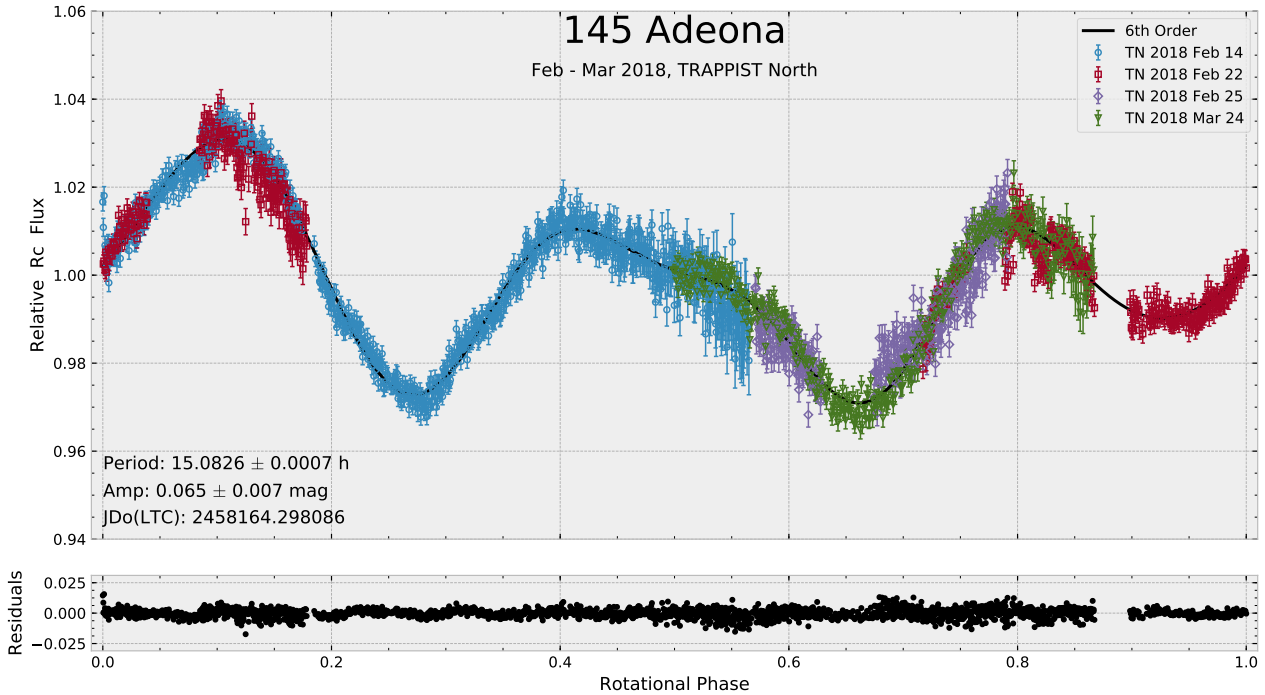

Figure 5.14: Phased lightcurve of (145) Adeona.

The previous accepted rotation period was 15.071 h (Pilcher, 2010). Our important amount of data as well as the time separation of more than a month between first and last night allowed us to compute a more accurate period. We found P = 15.0826 ± 0.0007 h (Fig. 5.15), which fits our data better than the previous one.

Table 5.7: Summary of (145) Adeona observations.

(145) Adeona - P $\simeq$ 15.1 h						
Date	Julian date	Telescope	Filter	Phase angle (°)	Duration (h)	Number of images
2018-02-14	8164	TN	Rc	17	8.6	948
2018-02-22	8172	TN	Rc	19	6.7	578
2018-02-25	8175	TN	Rc	20	3.4	302
2018-03-24	8202	TN	Rc	25	5.5	444
Total					24.2	2272

A difficulty for the observations of Adeona was its slow apparent movement in the sky. Because of this, when the asteroid passes near a star as seen from Earth, it will stay near the star for a long time. The point spread functions of the asteroid and the star will then blend together and the aperture photometry will record
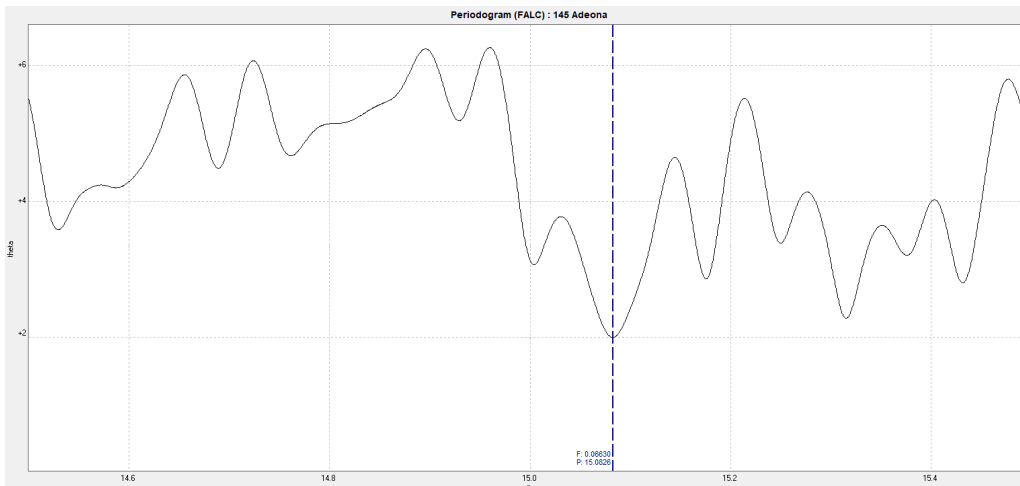
Figure 5.15: Period spectrum of (145) Adeona with the FALC method.

fluxes from both objects, leading to an apparent increase in the brightness of the asteroid. When this happens to asteroids with higher apparent motion, the affected data are simply discarded. However, for these observations of Adeona, that would have lead to the loss of large amount of data. Nonetheless, if the flux of the star is stable, it is possible to recover the flux variations of the asteroid. If we make sure to have an aperture large enough to include both the star and the asteroid, the star flux will only add a constant value to the total measured flux. We can estimate it by averaging the flux of the star before it blends with the asteroid. By subtracting this value we can hope to recover the flux variation of the asteroid, only at the cost of adding some noise. Here we could recover the data taken on February 22 (red square symbols on Fig. 5.14) and corresponding to rotational phases from 0.08 to 0.18.

5.1.8 (45) Eugenia

Eugenia is a MBA of the F-type classification (dark carbonaceous asteroids) with a diameter $D = 202 \pm 2$ km (NASA/JPL, 2017b). It is the second known triple asteroid system after (87) Sylvia. Petit-Prince ($D \sim 13$ km) was discovered in 1998 and orbits Eugenia at about 1180 km. S/2004 (45) 1 is smaller ($D \sim 6$ km) and was discovered on images taken in 2004 with the ESO VLT (Marchis et al., 2007).

We observed it on a single night of March 2018 with TRAPPIST-S and a Rc filter, covering about 1.4 rotation. We used a period of 5.699152 h (Hanuš et al. (2017) and references therein) to fold the lightcurve (Fig. 5.16). The phased lightcurve shows a very regular bimodal shape and an amplitude $A = 0.156 \pm 0.006$ mag.

Table 5.8: Summary of (45) Eugenia observations.

(45) Eugenia - P ≃ 5.7 h						
Date	Julian date	Telescope	Filter	Phase angle (°)	Duration (h)	Number of images
2018-03-06	8184	TS	Rc	5.3	7.9	1155

5.1.9 (22) Kalliope

Kalliope is a M-type binary asteroid. In 2007, a campaign of photometric observations coordinated by the IMCCE was organised to observe the mutual eclipses between Kalliope and its satellite Linus. Such events happen when the orbital plane of Linus is aligned with the Sun's line of sight. This configuration occurs every
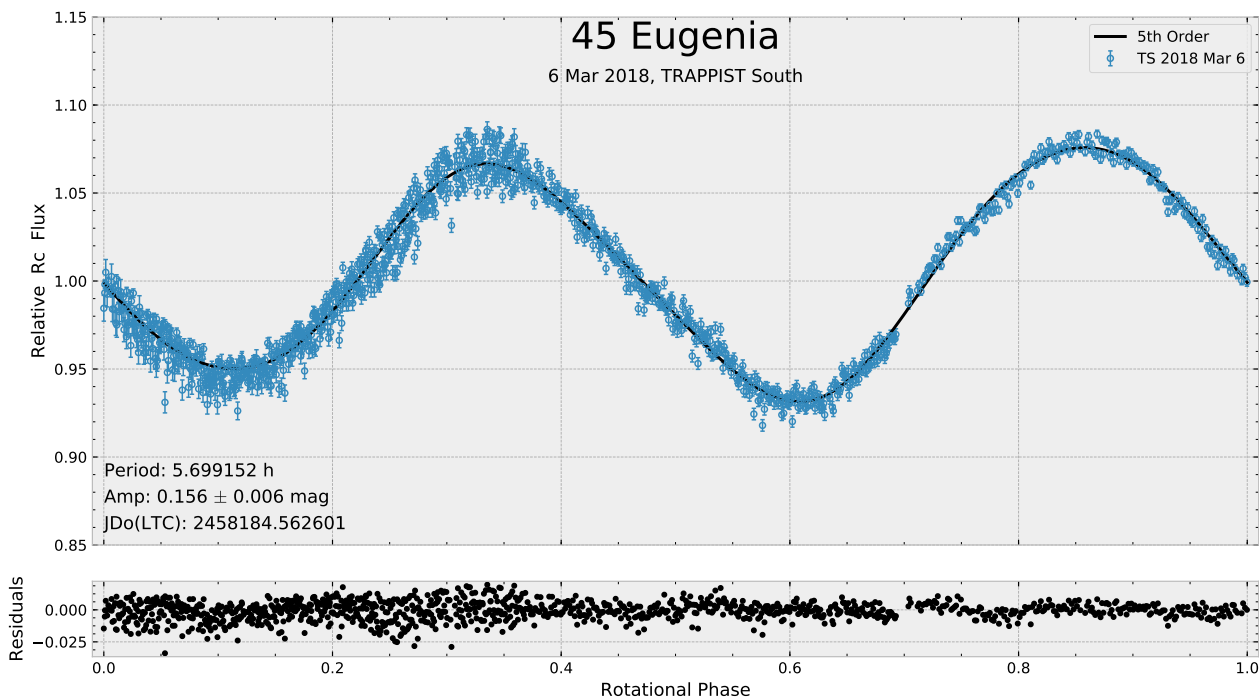
Figure 5.16: Phased lightcurve of (45) Eugenia.

2.5 years. The observation campaign allowed to constrain the sizes of the two bodies. They derived new values of the diameter of Kalliope (166.2 ± 2.8 km) and of Linus (28 ± 2 km), which is considered as spherical ([Descamps et al., 2008](#)). They also gave a new estimate of the bulk density of Kalliope, $3.3 \pm 0.33 \, \mathrm{g \, cm^{-3}}$.

We observed Kalliope in 2018 as part of the ESO LP collaboration and it was already observed by TRAPPIST-S in February 2012 to try to catch some events of the 2012 season of mutual eclipses.

2012 Observations with TRAPPIST-S

In 2012, Kalliope was observed during 3 nights on February 5, 7 and 27. An eclipse was predicted to happen on the 27th, with the shadow of Linus being projected on Kalliope's surface. The lightcurve attenuation was predicted to last about 2 hours with an amplitude of 0.03 to 0.07 mag, depending on the size of Linus ([Springmann et al., 2012](#)). Linus is big for an asteroid moon (D $\sim$ 28 km) but the size ratio between Kalliope and Linus is only about 0.17. Hence, the eclipses does not result in sharp peaks in the lightcurves but rather in slight attenuation of a few hours long while variations due to the rotation of Kalliope still dominate.

Our lightcurves of the 5th and 7th cover the full rotation and the lightcurve of the 27th, when merged with the first two, shows a clear attenuation (top panel of Fig. [5.17](#)). A 6th order Fourier fit has been done on the data of the first two nights that are used as reference lightcurves. The difference between this fit and the eclipse lightcurve is plotted in the bottom panel of Fig. [5.17](#). The flux drop during the event can be clearly seen. The eclipse ingress was observed but not the end of the event. Such eclipses detection from multiple sites and nights can then be analysed and are used to refine Linus's size and orbital model.

With the 2012 observations, the ANOVA method of Peranso provides a period of P = 4.1485 ± 0.0008 h (Fig. [5.18](#)), which is in agreement with the value of P = 4.1483 h in the Asteroid Lightcurve Database[3] (LCDB) ([Warner et al., 2009](#))) and P = 4.14820 h ([Hanuš et al., 2017](#)).

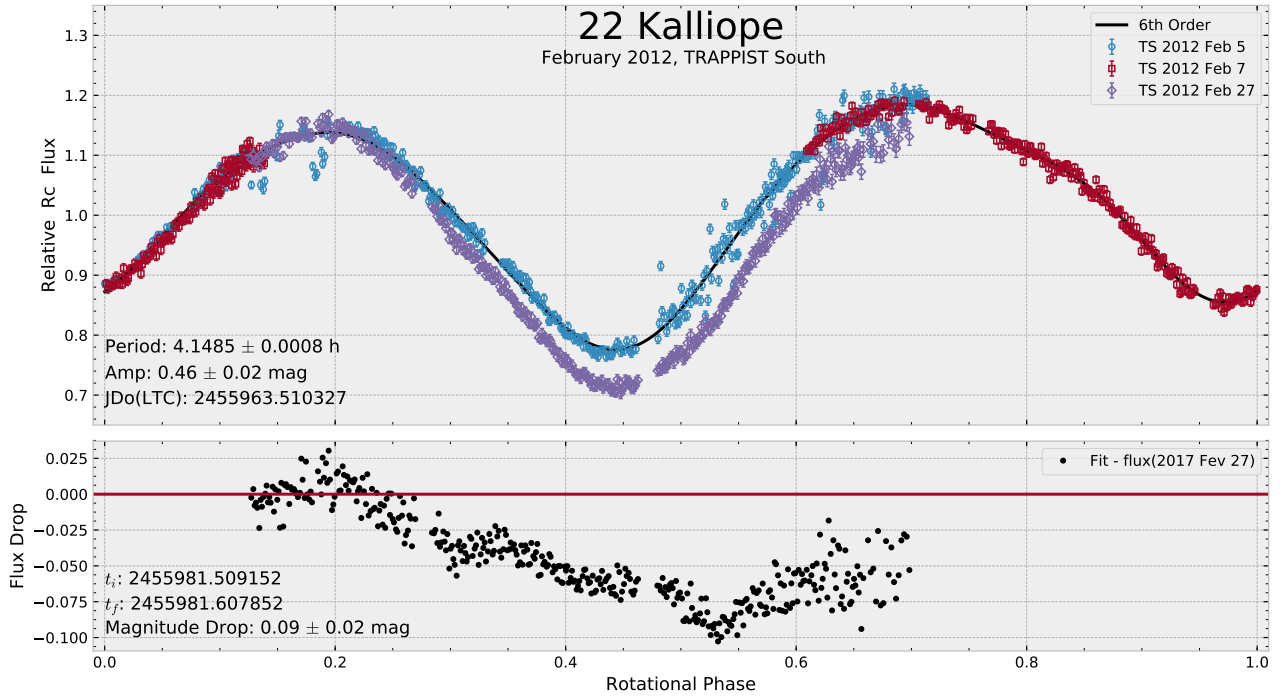[3] http://www.minorplanet.info/lightcurvedatabase.html

Figure 5.17: Phased lightcurve of (22) Kalliope in 2012. *Top*: Lightcurves of 2012 February 5 and 7 are taken as reference and fitted with a Fourier fit. *Bottom*: Difference between the fit and the event lightcurve.
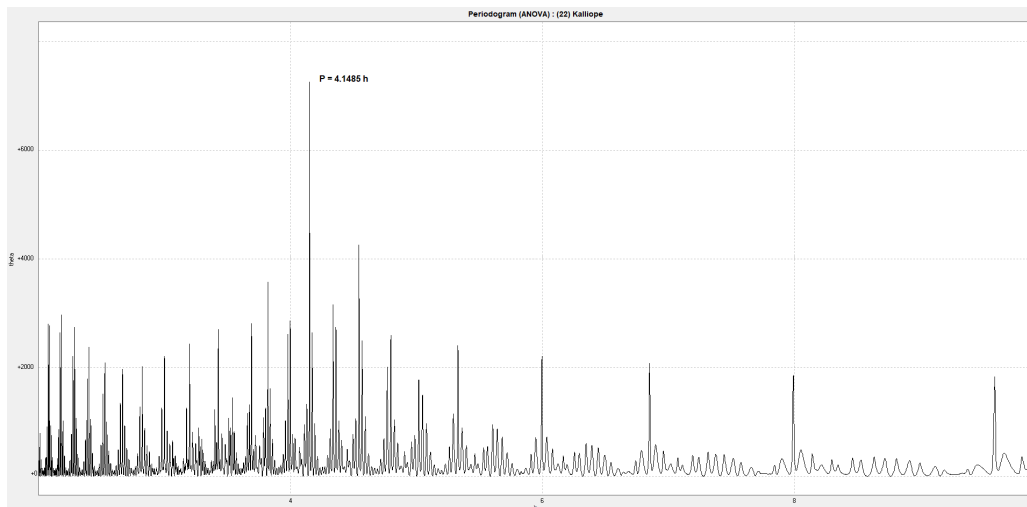

Figure 5.18: Period spectrum of (22) Kalliope with the ANOVA method.

Table 5.9: Summary of (22) Kalliope - February 2012 observations.

(22) Kalliope - P ≃ 4.1 h						
Date	Julian date	Telescope	Filter	Phase angle (°)	Duration (h)	Number of images
2012-02-05	5963	TS	Rc	16.9	3.0	438
2012-02-07	5965	TS	Rc	17.4	2.4	403
2012-02-23	5981	TS	Rc	20.1	2.6	424
Total					8.0	1265

2018 Observations with TRAPPIST-N

The observations of March 2018 were done during an observing mission with students of the University of Liège Space Sciences master at the Oukaïmeden observatory. We used TRAPPIST-N with the Rc filter for a total of 19.6 hours spread on 5 nights. Kalliope rotates fairly quickly, we thus have a dense coverage of the rotation curve (Fig. 5.19).
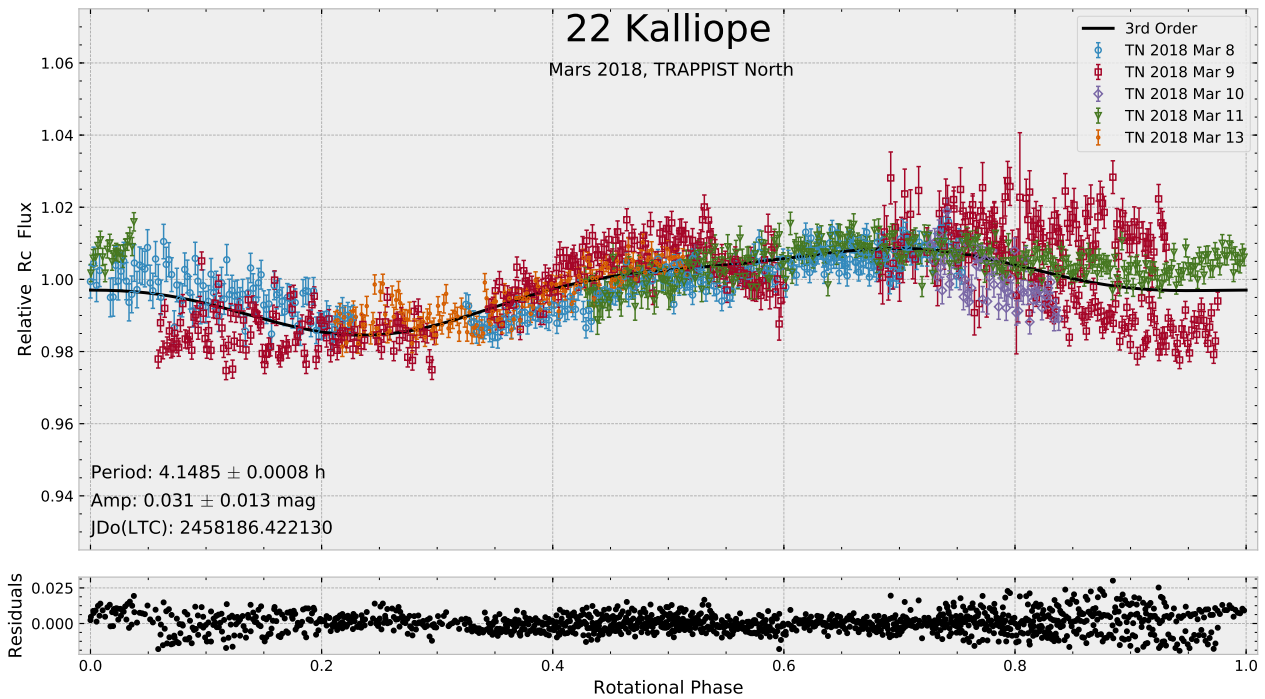

Figure 5.19: Phased lightcurve of (22) Kalliope in March 2018.

While the data look noisy, it is due to the very low variations of Kalliope's brightness at this epoch. Indeed, we determined a large amplitude $A_{2012} = 0.460 \pm 0.020$ mag in February 2012 but only $A_{2018} = 0.031 \pm 0.003$ mag in March 2018. As illustrated in Fig. 5.20, the spin axis of Kalliope was seen on the side on 2012 (aspect angle = 70°) but was almost parallel to the line of sight in 2018 (aspect angle close to 180°).
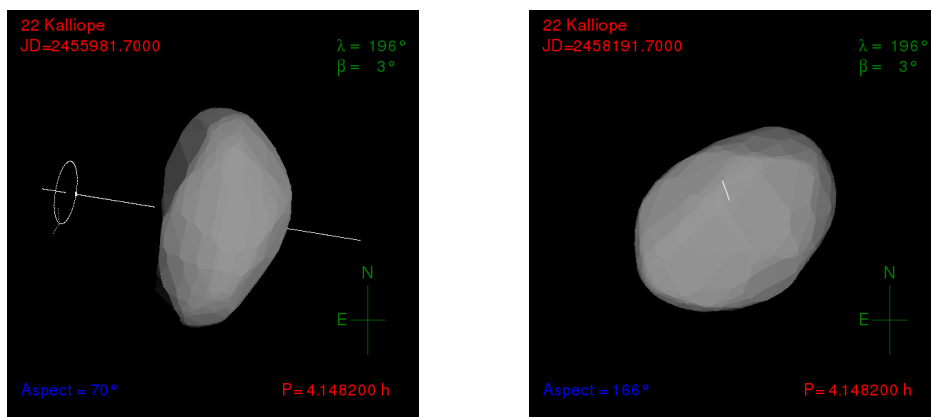

Figure 5.20: *Left*: Orientation of (22) Kalliope spin axis in February 2012. *Right*: Orientation of (22) Kalliope in March 2018. Source: Interactive service for asteroid models (ISAM).

A smoother curve was obtained by binning together the phased data. Figure 5.21 shows the result using bins

of rotational phase corresponding to 0.03 hours, with values given by the weighted average. Errors are given by the standard error of the mean.
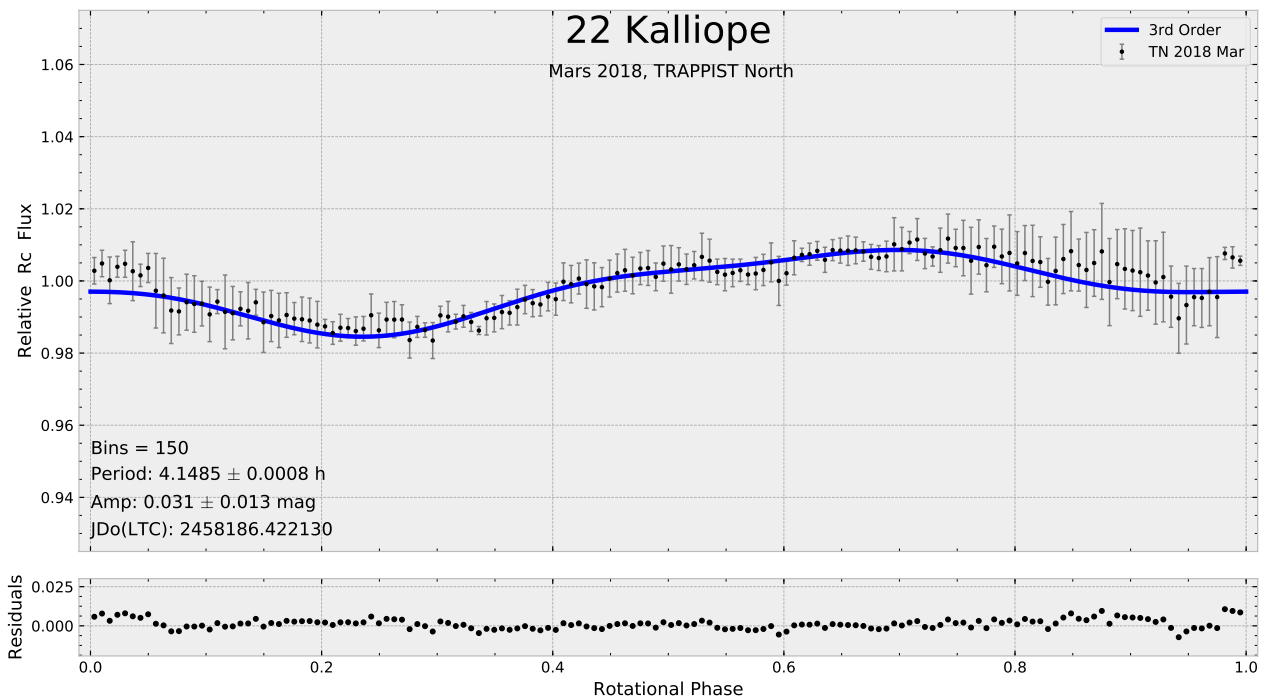

Figure 5.21: Binned phased lightcurve of (22) Kalliope in March 2018.

Table 5.10: Summary of (22) Kalliope - March 2018 observations.

(22) Kalliope - $P \simeq 4.1$ h						
Date	Julian date	Telescope	Filter	Phase angle (°)	Duration (h)	Number of images
2018-03-08	8186	TN	Rc	10.0	7.3	335
2018-03-09	8187	TN	Rc	9.7	8.1	510
2018-03-10	8188	TN	Rc	9.4	0.4	62
2018-03-11	8189	TN	Rc	9.2	2.5	325
2018-03-13	8191	TN	Rc	8.7	1.3	159
Total					19.6	1391

5.2   Near-Earth Asteroids (NEAs)

We will now focus on much smaller objects than the MBAs we have studied previously. NEAs have often sizes of less than a few kilometres and their orbits are such that from time to time they approach Earth closely (see Sect. 2.1.3). Those close encounters are always great opportunities to learn more about those peculiar objects and asteroids in general. In this section, we present observations of three NEAs: (3122) Florence, K17V12R and K18D01H. Another NEA, the large and unusual (3200) Phaethon will be the subject of a separate section.

5.2.1   (3122) Florence

The first NEA we observed was Florence on September 3, 2017, two days after its closest approach to Earth at a distance of about 7 millions km. It is an Amor asteroid (asteroids approaching Earth's orbit without crossing

it) and is classified as potentially hazardous because of its low minimal distance with Earth. Its size makes it the 4th largest known NEA, just after (3200) Phaethon. Florence was discovered in 1981 and has been already well studied. Estimations of its rotation period of about 2.36 hours (see LCDB; Warner et al. (2009)), size of D = 4.010 ±1.237 km and visible albedo of p_V = 0.258 ± 0.199 (Mainzer et al., 2012), were already available before the 2017 flyby. However nothing was known on the pole direction or the presence of moons. During the flyby, Florence was the target of many photometric, spectroscopic, IR radiometry and radar observations. Observations from the Goldstone and Arecibo observatories revealed that Florence has two little moons and is therefore the third known triple NEA (Fig. 5.22).

Figure 5.22: Radar image of (3122) Florence and its two moons with the Arecibo Observatory. Credit: NASA/JPL.

For the observations of Florence we used both TRAPPIST-S and TRAPPIST-N. We observed it during 7.7 hours with 1.3 hours of overlap between the two telescopes. We used the V filter (plus a few measurements in Ic) and covered three complete rotations. The data are well fitted by a 5th order Fourier series and reveal an amplitude of 0.222 ± 0.015 mag, which is the sign of a relatively small elongation of Florence's shape (for a body of a few kilometres).

For the rotation period we obtained P = 2.3652 ± 0.0012 h with the ANOVA method (Fig. 5.24). Various observers previously reported periods around this value (e.g. Warner (2018a)).

Table 5.11: Summary of (3122) Florence observations.

(3122) Florence - P $\simeq$ 2.4 h						
Date	Julian date	Telescope	Filter	Phase angle (°)	Duration (h)	Number of images
2017-09-03	8000	TN	Ic	44.5	0.5	18
2017-09-03	8000	TN	V	44.5	5.6	579
2017-09-03	8000	TS	V	44.5	2.9	268
Total					9.0	865

We took advantage of the measurements from the two very distant telescopes to also estimate the distance of Florence at the time of the observations. We applied the parallax method as explained in Appendix B. The measurement is achieved by stacking images from both telescopes taken at the same time and by directly measuring the offset on the sky between the two positions of the asteroid. Here we used 70 images from the two telescopes and the stack of the images shows clearly the two separate parallel trails (Fig. 5.25), due to the small distance of Florence and the large telescope separation. The result of the measurement is a distance d = 0.050 ±
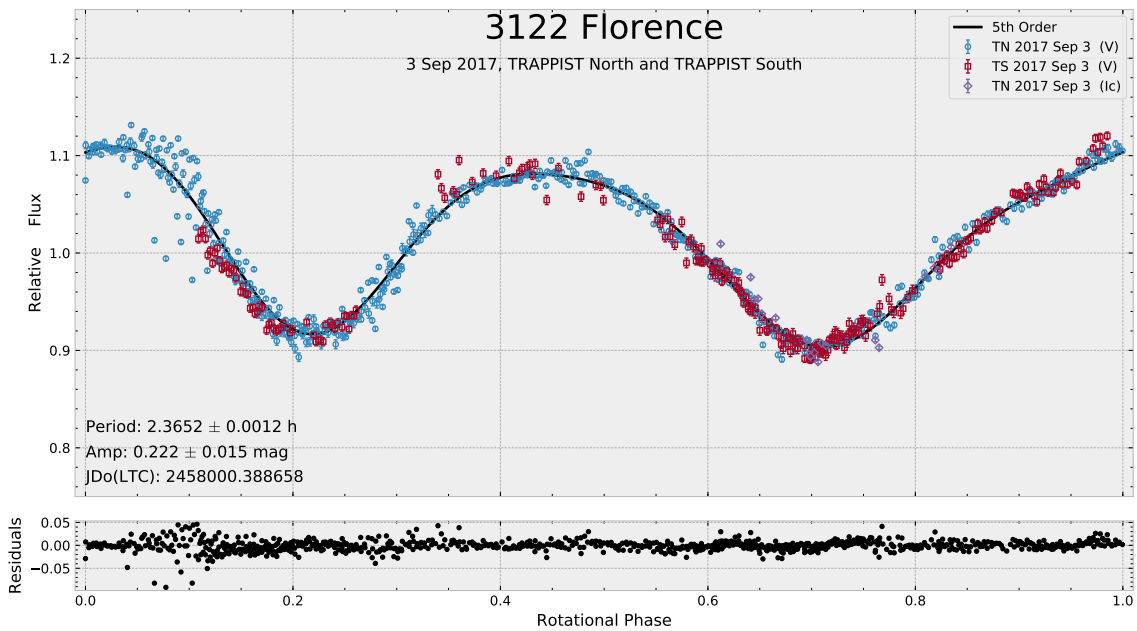
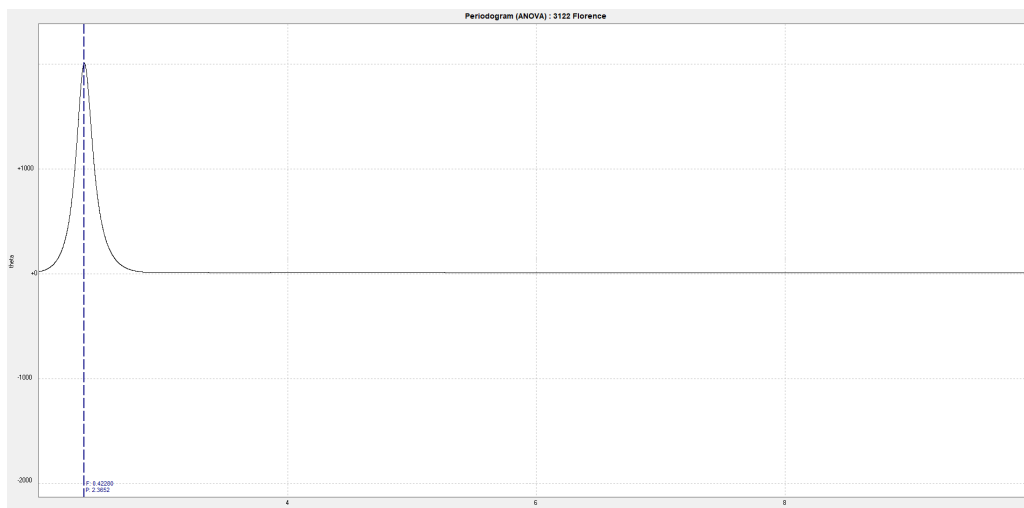Figure 5.23: Phased lightcurve of (3122) Florence.

Figure 5.24: Period spectrum of (3122) Florence with the ANOVA method.

0.002 au (19.4 lunar distances). The orbit of Florence was well known and the distance was available from the ephemerids. The Horizons website (NASA/JPL, 2017a) gives a distance of 0.051 au (19.9 lunar distances) at the time of our measurement, which is very close to what we found.

5.2.2 K17V12R

K17V12R is a NEA discovered on 2017 November 10 by the telescope Pan-STARRS 1 in Hawaii[4]. It approached Earth within 3.8 lunar distances on 7 March 2018. Before this flyby, only its absolute magnitude H = 20.3 was known (NASA/JPL, 2017b), which results in a diameter of about 250 m assuming an albedo of 20%. It was observed by the Goldstone/Green Bank Telescope[5], a NASA Deep Space Network antenna throughout 1.3

---

[4] https://panstarrs.stsci.edu/
[5] https://echo.jpl.nasa.gov/asteroids/2017VR12/2017VR12_planning.2018.html
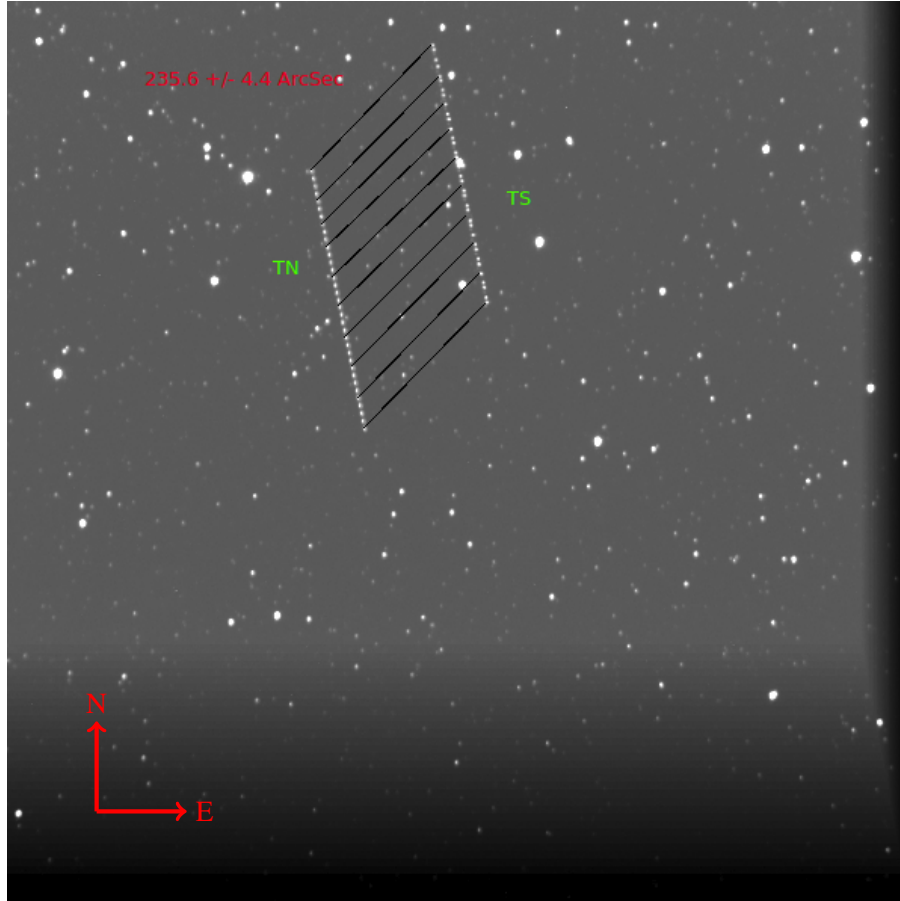
Figure 5.25: Stack of 70 images of Florence from Trappist-S and 70 images from TRAPPIST-N, taken approximately at the same time, during its close approach to Earth on September 3, 2017.

rotation, with a resolution of 3.75 m $\times$ 0.5 Hz.

We observed K17V12R on March 8, 2018 with TRAPPIST-N, also as part of the observing mission with the master students in Morocco. We used the Rc filter and a 2$\times$2 binning. It was bright (m$_V$ $\sim$ 11.4 mag) so we used exposure time of only 15 seconds. We only observed during 2.7 hours due to its small visibility window, but we were surprised to still derive a nice lightcurve with 2 clear maxima and minima. The large amplitude of 0.907 ± 0.070 mag points to a somewhat elongated body (Fig. 5.26), which is more common for NEAs that are usually small bodies.

With Peranso and the ANOVA method we found a rotation period of 1.3718 ± 0.0032 h (Fig. 5.27). This value was confirmed by other teams (e.g. P = 1.37752 ± 0.00007 h in the LCDB).

Our photometric data will be used together with the radar observations in future modelling of this asteroid.

Table 5.12: Summary of K17V12R observations.

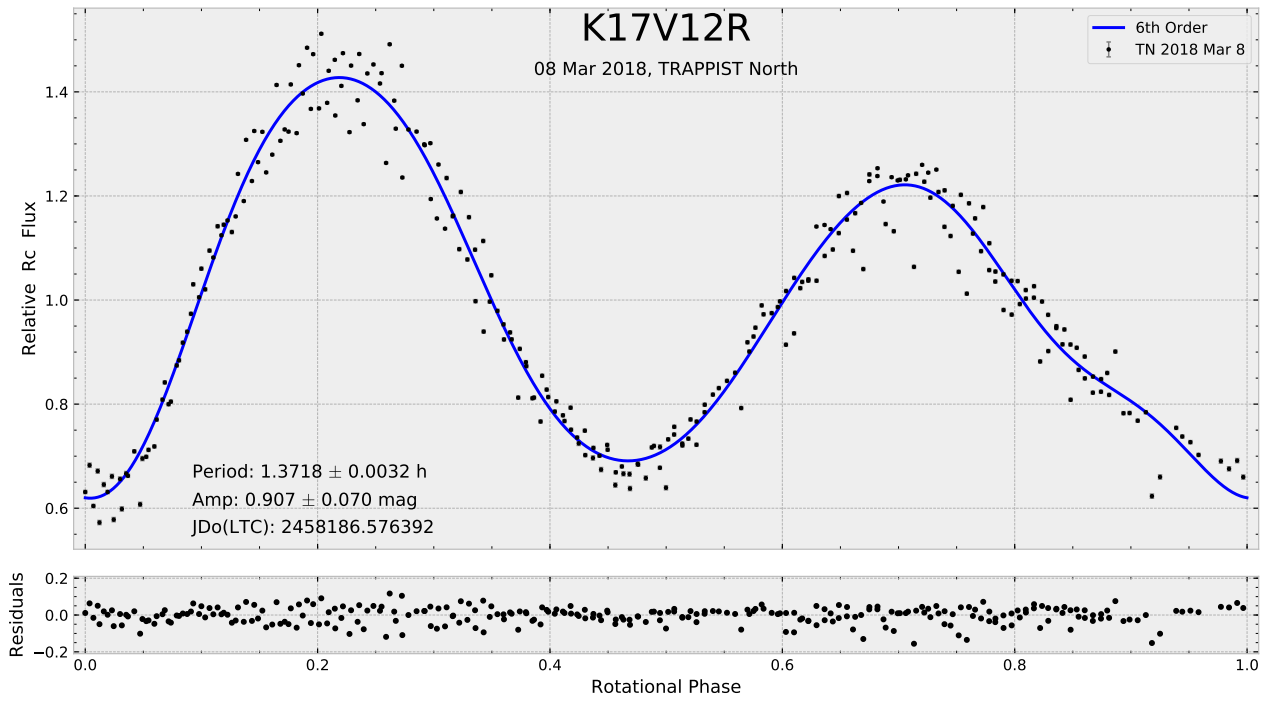| K17V12R - P $\simeq$ 1.4 h						
Date	Julian date	Telescope	Filter	Phase angle (°)	Duration (h)	Number of images
2018-03-08	8186	TN	Rc	47.6 - 49.3	2.7	272

Figure 5.26: Phased lightcurve of K17V12R on March 8, 2018.

Figure 5.27: Period spectrum of K17V12R with the ANOVA method.

5.2.3   K18D01H

K18D01H is another NEA that we observed from Morocco with TRAPPIST-N in March 2018. It was discovered a few days earlier, on February 22, 2018 at the Purple Mountain Observatory (China) and not much was known about this asteroid. It is an Apollo asteroid ($a \geq 1$ au and $q \leq 1.017$ au) and its absolute magnitude is 21.1 mag (NASA/JPL, 2017b). Assuming a geometric albedo of 0.20 (S-type) or 0.04 (C-type), one can estimate a size of 180 or 400 meters respectively. It was expected to flyby Earth on March 27, at a minimal distance of 0.024 au (9.2 lunar distances). We had observed it on March 12 when it was still approaching Earth and was still faint ($m_V \sim 17.3$ mag) while it was the last day it was visible with TRAPPIST telescopes. We used TRAPPIST-N with a 2×2 binning, no filter to collect a maximum of light and an exposure time of 90 seconds. We observed it for 1.6 hours before we had to stop because of degrading atmospheric conditions. As its period was estimated to be about 5 hours (measured by Petr Pravec at Ondrejov Observatory[6]), we covered only a part of its rotation curve (Fig. 5.28).
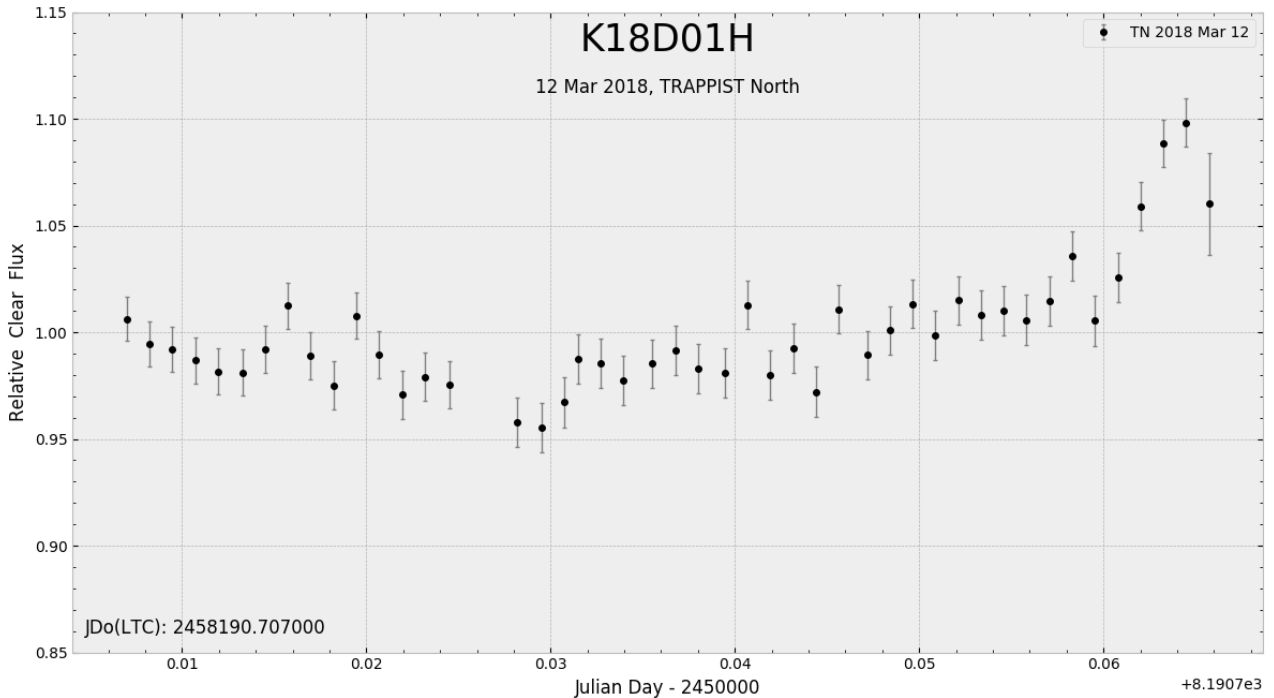

Figure 5.28: Lightcurve of K18D01H on March 12, 2018.

Table 5.13: Summary of K18D01H observations.

K18D01H - $P \simeq 5.0$ h						
Date	Julian date	Telescope	Filter	Phase angle (°)	Duration (h)	Number of images
2018-03-12	8190	TN	Clear	7.0	1.58	46
2018-03-12	8190	TS	exoBB	6.9	0.16	6
Total					1.74	52

We also took some images of K18D01H with TRAPPIST-S, to measure its distance with the parallax method. The estimation was a bit harder than for (3122) Florence because of the smaller angle and because K18D01H

---

[6] http://www.asu.cas.cz/~ppravec/neo.htm

was moving almost in the same direction than the offset in the sky (Fig. 5.29). Our result is d = 0.125 ± 0.005 au, which is close to the value of 0.124 au given by the ephemerids of the Horizons website (NASA/JPL, 2017a).
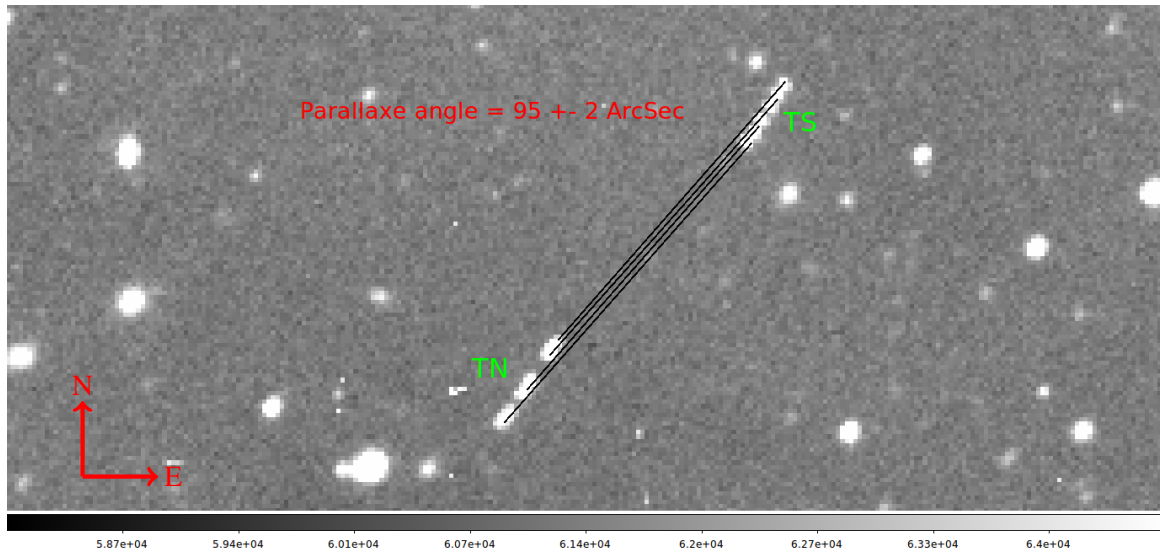

Figure 5.29: Stack of 6 images of K18D01H from Trappist-S and 6 images from TRAPPIST-N, taken approximately at the same time on 2018 March 12, 2018.

5.3 (3200) Phaethon

Phaethon is an enigmatic NEA discovered in 1983 in the data of the NASA's InfraRed Astronomical Satellite (IRAS), followed by optical confirmation at Palomar Observatory (Green and Kowal, 1983). It is an Apollo, B-type asteroid and the third largest NEA known, with a diameter of 5.1 ± 0.2 km (NASA/JPL, 2017b). Phaethon has a peculiar orbit, shown in Fig. 5.30, that looks like a comet orbit. However, its Tisserand parameter T_J = 4.5 is not cometary[7] (Jewitt et al., 2015). Its eccentricity of 0.89 is unusually high and its perihelion ($q \sim$ 0.14 au) is the smallest of all known asteroids. This very small perihelion distance, which makes Phaethon periodically graze the Sun, is also at the origin of its name (Phaethon is the son of the Sun's god Helios in the Greek mythology).

Phaethon is considered as the parent body of the Geminid meteor shower (maximum on December 14) because of the similarities of the orbits (Williams and Wu, 1993). This raised the question of the nature of Phaeton as a potential inactive comet nucleus. However, de León et al. (2010) found that Pallas was likely the parent body of Phaethon due to spectral similarities and dynamical connections, although the spectrum of Phaethon is bluer than that of Pallas. Before 2009 no evidence of mass loss or comet-like activity was found. However, Jewitt and Li (2010) and Jewitt et al. (2013) found in the data of NASA's STEREO solar spacecraft an unexpected brightening by a factor 2 near its perihelion passages of 2009 and 2012, associated with a comet-like tail (Fig. 5.30). Phaethon's surface is too hot near perihelion ($\sim$1000 K) for water to survive. It has been thus proposed that dust particles are created by thermal fracturing and then swept away by the radiation pressure. However, the effective diameter of the particles estimated from the STEREO data is $\sim$1 μm while the typical sizes of the Geminid meteors range from $\sim$10 μm to 4.5 cm. Hence, the question of the exact process or processes at the origin of the Geminid stream is still open.

---

[7]The Tisserand parameter of a small body is calculated from several of its orbital elements and those of a perturbing larger body (frequently Jupiter, T_J). This parameter allows to discriminate cometary ($T_J < 3$) from asteroidal ($T_J > 3$) orbits.
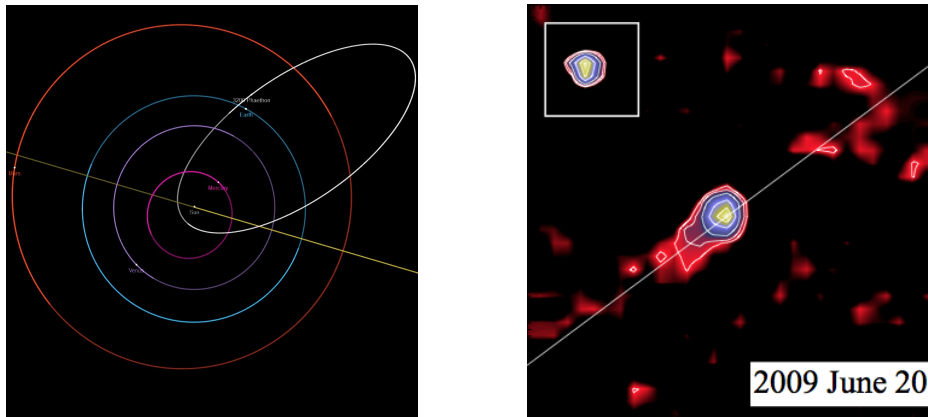
Figure 5.30: *Left*: The Sun-grazing orbit of (3200) Phaethon. Image generated with the SBDB website; NASA/JPL (2017b). *Right*: Dust tail of (3200) Phaethon along the projected sun-comet line at perihelion in 2009. The image is $490''$ square and the point spread function of a near star is shown for comparison (Jewitt et al., 2013).

During the 30 years following its discovery, Phaethon was the subject of numerous studies. For exemple, in Hanuš et al. (2016a) one can found an extensive study of different Phaethon's properties. They presented a new convex shape model with ecliptic coordinates of the pole orientation of $(319°, −39°)$. They derived its size (D = 5.1 ± 0.2 km) and geometric albedo ($p_V = 0.122 \pm 0.008$) and characterised its thermal parameters, surface roughness and orbit. Notably they found that the strong solar heating during perihelion passages is not connected to a specific area on the surface. Such preferential heating could have affected the spectral properties of Phaethon's surface. Their best solution for the rotation period, using all available photometric measurements at the time, is 3.603958 hours. This value is consistent with various other measurements, all around 3.6 hours (see LCDB; Warner et al. (2009)).

In 2017, Kinoshita et al. (2017) announced that they inferred longitudinal inhomogeneity on Phaethon's surface from their rotationally time-resolved visible spectroscopy data of the asteroid obtained in 2007. From their observations, Phaethon's surface is dominated by B-type coloured (blue) material due to thermal metamorphing. This material would be related to CI/CM chondrites. In addition, they found at a particular rotational phase a C-type red-spectral slope suggesting the presence of a large C-type red-coloured area (D $\sim$ 2.9 km) in the mid-latitude of Phaethon's southern hemisphere (Fig. 5.31).

Despite the fact that it has already been well studied, Phaethon still holds many secrets. In December 16, 2017, Phaethon approached within 0.069 au of Earth. It will not pass closer before 2093, it was then the best opportunity so far to characterise it. Phaethon will be the target of the Japan Aerospace Exploration Agency (JAXA) flyby mission Demonstration and Experiment of Space Technology for INterplanetary voYage, Phaethon fLyby and dUst Science (DESTINY+). This mission scheduled in 2022 will be equipped with a multi-band cameras and a dust analyser, and aims among other things to realise high-resolution imaging of Phaethon and to understand dust ejection mechanisms of active asteroids (Arai et al., 2018).

5.3.1 Phaethon's 2017 close approach

On December 2017, Phaethon approached closely to Earth. It passed at only 0.069 au (27 lunar distances) from Earth on December 16. It was brighter than mag 16 for about a month and reached mag 11 on December 15. The phase angle changed very rapidly between December 13 and 21 (from 29° to 117°) during this short time
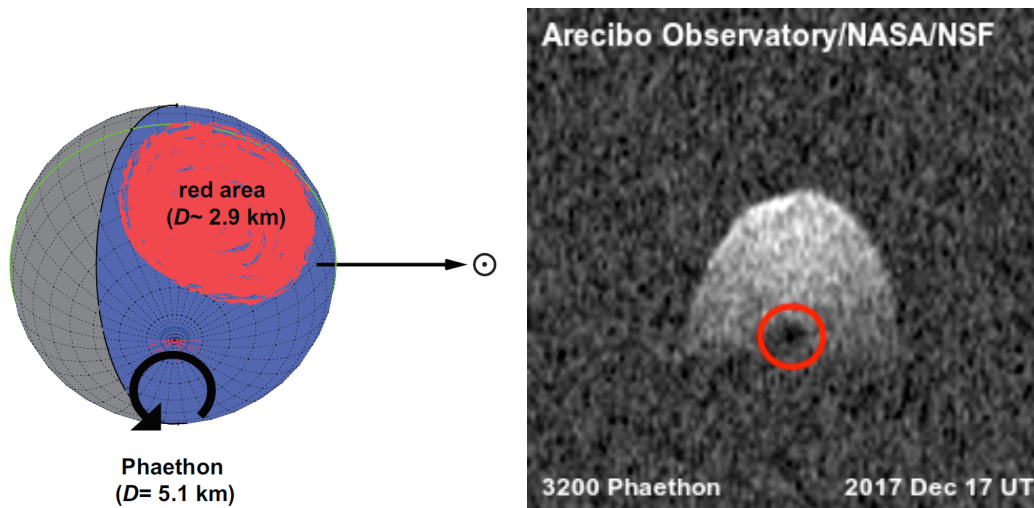
Figure 5.31: *Left*: Schematic of the red area on Phaethon's surface as viewed from Earth in December 2007 (Kinoshita et al., 2017). *Right*: Arecibo radar images of Phaethon on December 17, 2017. The dark radar features is circled in red (Taylor et al., 2018).

span (Fig. 5.32, left). Phaethon crossed the galactic plane on December 11 and was therefore on crowed fields around that date (Fig. 5.32, right)
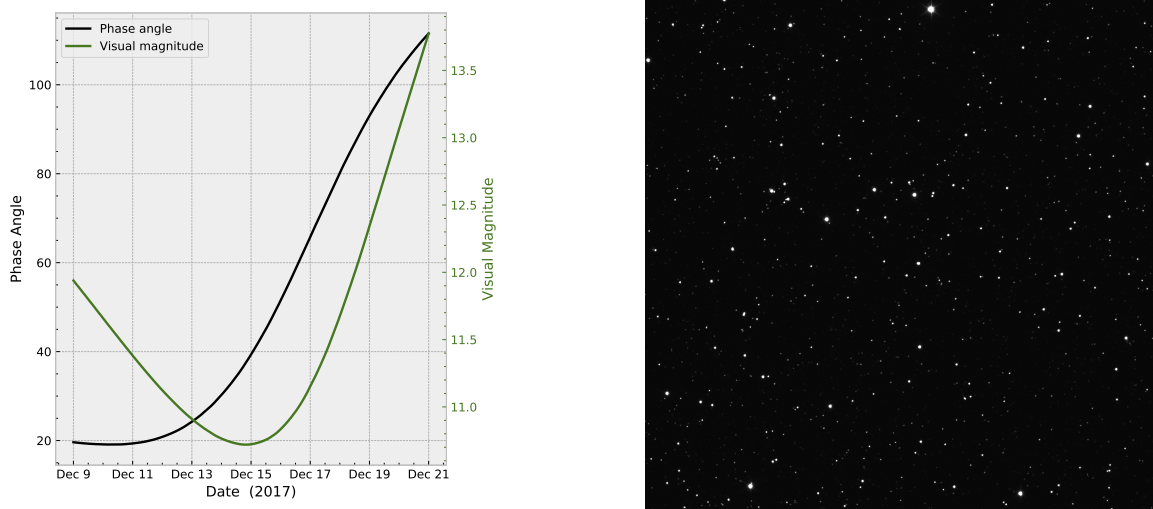

Figure 5.32: *Left:* Variation of the phase angle and visual magnitude of Phaethon between 2017 December 9 and 21. *Right:* Image of Phaethon in a crowded field taken with TRAPPIST-N on December 10, when it was near the galactic plane.

At the occasion of this unprecedented flyby, a large observation campaign with various techniques and telescopes was setup. It was notably observed with the Arecibo planetary radar system and the Goldstone Solar System Radar (Taylor et al., 2018). Arecibo range-Doppler images covered the full rotation at a resolution of 75 meters per pixel. The Goldstone radar collected echo power spectra from December 11 to 21. The observations revealed a larger diameter (D ~6 km) than previously estimated (D ~5.1 km), and a roughly spheroidal shape. The images also show a large concavity near the equator and a radar dark feature near one of the poles (Fig.5.31). This radar dark spot could be due to a polar crater or a region flatter than its surroundings.

5.3.2 TRAPPIST-N observations

The close approach of Phaethon was visible from the Oukaïmeden observatory in Morocco. We extensively observed it with TRAPPIST-N during 8 nights between December 9 and 20. The total duration of the observations is of about 54 hours and 5478 individual measurements are used in the final lightcurves (details are given in Table 5.14). The first two nights (December 9 and 10), the four Johnson-Cousins filters (B, V, R and Ic) were used alternatively to sample the lightcurve in different colours. On December 13, only the Rc filter was used. During those three first nights Phaethon was near the galactic plane and was therefore crossing fields containing a lot of stars. This is problematic for photometric measurements because the signal of a nearby star will pollute the measurement of the brightness of the asteroid. Fortunately, the path of Phaethon on the sky avoided most of the bright stars and only a few amount of data were lost. On December 14 we first observed with the Rc filter (plus a few regular measurements in B, V and Ic), then with the V filter. On December 15 we observed first in the Ic band, then in B. The last three nights (December 18, 19 and 20), only the Rc filter was used. Phaeton was also observed from the same site by Claudine Rinner and Michel Ory with The Morocco Oukaïmeden Sky Survey (MOSS) telescope (D = 0.5 m), during 7 nights and with a Clear filter (Table 5.15).

Table 5.14: Summary of Phaethon observations with TRAPPIST-North.

Date	Julian date	Telescope	Filter	Phase angle (°)	Duration (h)	Number of images
(3200) Phaethon - P ≃ 3.6 h						
2017-12-09	8097	TN	B	19.1		140
2017-12-09	8097	TN	V	19.1		234
2017-12-09	8097	TN	Rc	19.1		241
2017-12-09	8097	TN	Ic	19.1		226
Total 2017-12-09					11.5	841
2017-12-10	8089	TN	B	19.3		120
2017-12-10	8089	TN	V	19.3		202
2017-12-10	8089	TN	Rc	19.3		222
2017-12-10	8089	TN	Ic	19.3		209
Total 2017-12-10					8.2	753
2017-12-13	8101	TN	Rc	28.4 - 31.6	10.6	1339
2017-12-14	8102	TN	B	36.7 - 40.7		24
2017-12-14	8102	TN	V	36.7 - 40.7		491
2017-12-14	8102	TN	Rc	36.7 - 40.7		359
2017-12-14	8102	TN	Ic	36.7 - 40.7		24
Total 2017-12-14					7.7	898
2017-12-15	8103	TN	B	48.2 - 50.1		371
2017-12-15	8103	TN	I	48.2 - 50.1		439
Total 2017-12-15					7.3	810
2017-12-18	8106	TN	Rc	90.0 - 92.0	3.4	365
2017-12-19	8107	TN	Rc	101.0 - 102.2	3.3	299
2017-12-20	8108	TN	Rc	109.7 - 110.3	2.4	170
Total					54.4	5478

5.3.3 Results

We had two main goals for the observations of Phaethon. The first one was to investigate potential colour variations throughout Phaethon's rotation. It was suggested from spectroscopic observations by Kinoshita et al.

Table 5.15: Summary of Phaethon observations with MOSS. These data were taken at the Morocco Oukaïmeden Sky Survey (MOSS) observatory (J43), also located at Oukaïmeden. Observations, with a remote 0.50 m, f/3 Newton telescope, and processing of the data (using PRISM 10.3.34.336.) were made by Claudine Rinner.

(3200) Phaethon - P ≃ 3.6 h						
Date	Julian date	Telescope	Filter	Phase angle (°)	Duration (h)	Number of images
2017-12-13	8101	MOSS	C	28.7 - 30.1	4.4	385
2017-12-14	8102	MOSS	C	37.2 - 39.0	4.0	616
2017-12-15	8103	MOSS	C	48.6 - 51.0	4.2	624
2017-12-18	8106	MOSS	C	90.3 - 91.3	2.0	264
2017-12-19	8107	MOSS	C	101.2 - 102.6	3.4	222
2017-12-20	8108	MOSS	C	109.8 - 110.8	3.0	356
2017-12-21	8109	MOSS	C	116.5 - 117.2	2.4	239
Total					23.4	2705

(2017), that Phaethon might have a large red-coloured area at its surface (Fig. 5.31). At this end, we carried out photometric measurements in B, V, Rc and Ic filters to be able to find potential differences in the lightcurves at different colours. An example of the study of the surface composition of an asteroid (here (15) Eunomia) through the construction of a colour map can be found in Nathues et al. (2005). The second objective was to observe the change in the lightcurve shape and amplitude due to the rapid variation of the phase angle between December 13 and 21. Such observations are very useful for the shape modelling of the asteroid because of the large changes in viewing geometries and illuminations. We used the TRAPPIST-N and MOSS data, along with previously available lightcurves, to reconstruct a shape model of Phaethon using the *Lightcurve Inversion* method (Kaasalainen et al., 2002a). Moreover, our lightcurves will be used in addition to the radar observations in a near future to revise its shape model.

We obtained a lot of data in a time span of 10 days, covering a total of about 15 rotations. This allowed us to derive a solid rotation period of Phaethon. We obtained P = 3.6034 ± 0.0001 h (Fig. 5.33), in agreement with the other values available (see LCDB; Warner et al. (2009)).
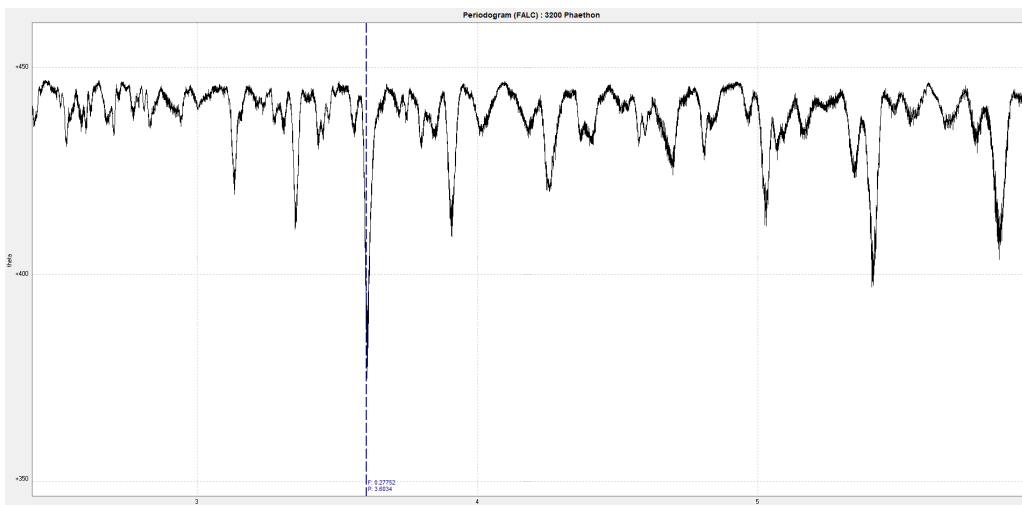

Figure 5.33: Period spectrum of (3200) Phaethon with the FALC method.

Colour variations

To investigate potential colour variation at the surface of Phaethon, the 4 Johnson-Cousins filters were used. On December 9 and 10 we alternated 5 measurements with the B filter, then 5 with the V, 5 with the Rc and 3 with the Ic, before getting back to B (Fig. 5.34). This way, we obtained a good sampling of the rotation curve in the four colours. The phase angle during these two nights was only changing very slowly as the asteroid was still far from Earth and did not induced significant variations in Phaethon's brightness at these dates. For these two nights, the data of the 4 filters were first phased together. Using the period determined with Peranso, the data fold very well and we cannot visually detect any colour variations in lightcurve (Fig. 5.35).
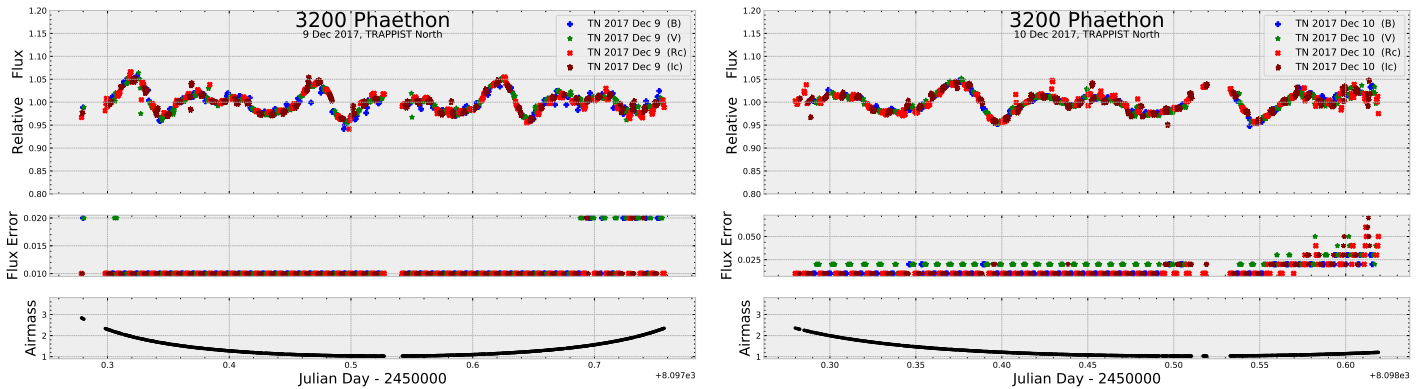

Figure 5.34: Lightcurve in Julian Days of (3200) Phaethon taken with TRAPPIST-N on December 9 and 10 with B, V, Rc and Ic filters.
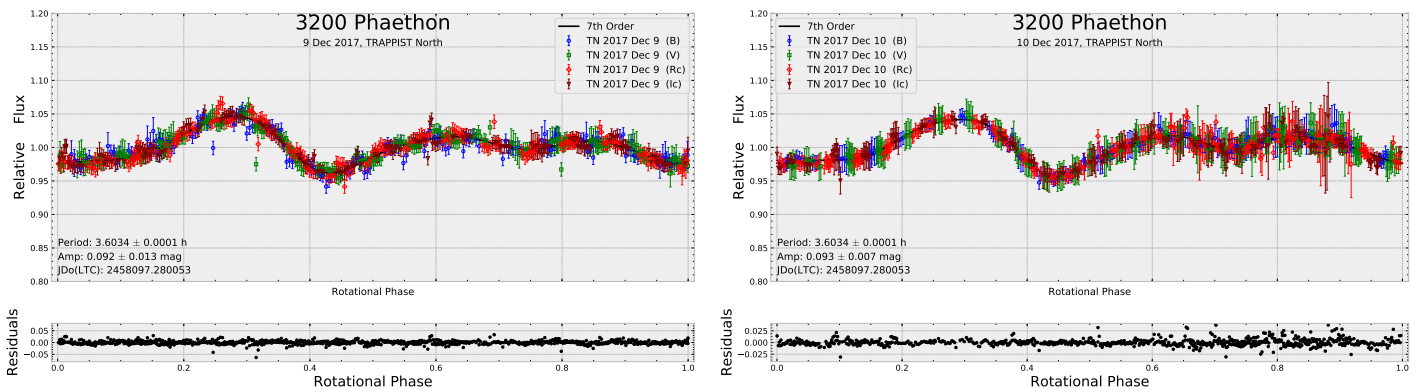

Figure 5.35: Phased lightcurve of (3200) Phaethon taken with TRAPPIST-N on December 9 and 10 with B, V, Rc and Ic filters.

The data of the two nights were then fitted by a 7th order Fourier series for each colour separately, in order to better compare them (Fig. 5.36). Some differences between the different colours in certain part of the lightcurves can be detected but they are small and they never repeat in the lightcurve of the other night. This is shown more clearly in Fig. 5.37 where the colour ratios V/Rc and B/Ic are plotted for the two nights and where no variation appears above the noise level.

The red-coloured area is thought to be located in the mid-latitude of Phaethon's southern hemisphere (Fig. 5.31). However, on December 9 and 10, mostly the northern hemisphere was observable (Fig. 5.37), which could explain the absence of colour variations in our data.
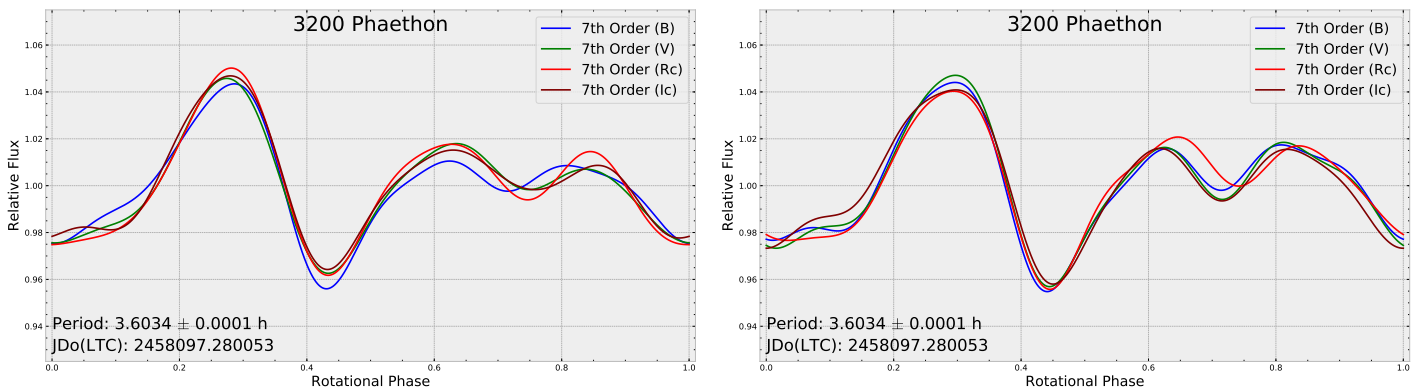
Figure 5.36: Fit by 7th order Fourier series of the B, V, Rc and Ic bands data. *Left*: Dec. 9 ; *Right*: Dec. 10.
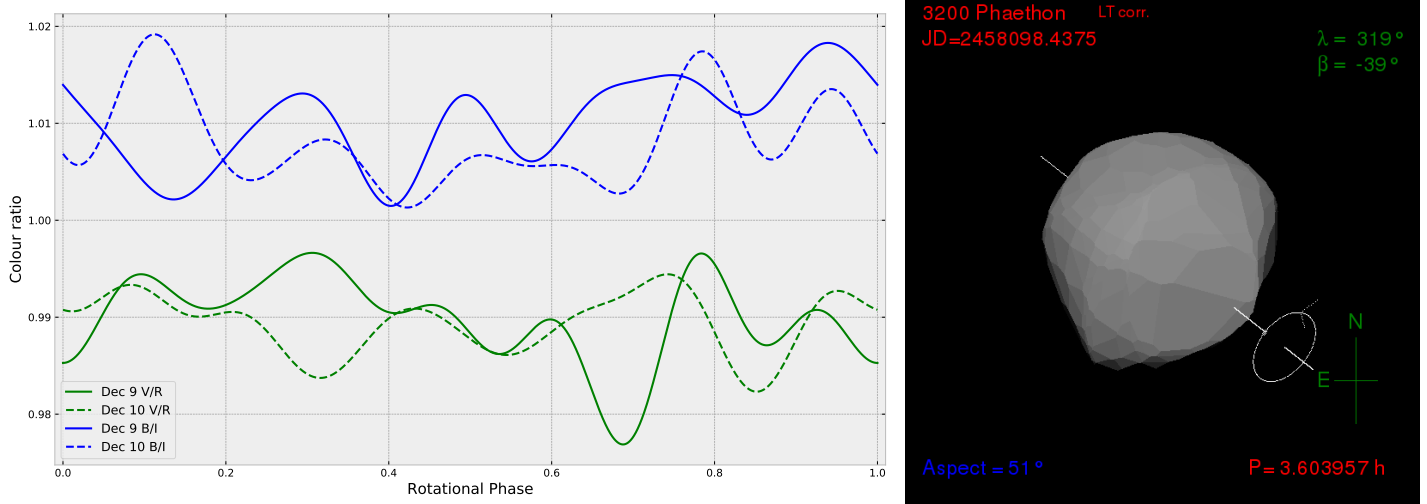

Figure 5.37: *Left*: Colour ratio V/Rc and B/Ic on December 9 and 10. The V/Rc curves are shifted with respect to the B/Ic curves for clarity. *Right*: Orientation of Phaethon on 2017 December 10. Source: Interactive Service for Asteroid Models (ISAM).

Phaethon could not be observed on December 11 and 12 due to bad meteorological conditions. From December 13 the phase angle started to increase rapidly, making the analysis of colour variation more difficult because the lightcurve was also changing as the phase angle increased. On December 13 only the Rc filter was used but on December 14 we observed first with the Rc filter (plus a few regular measurements in B, V and Ic) and then with the V filter (Fig. 5.38). On December 15 the Ic filter was used first then the B filter (Fig. 5.39). At these dates, the viewing angle was more favourable to the observation of the northern hemisphere (the aspect changed from 51° on Dec. 10 to 84° on Dec. 15) but the phase angle was varying so fast that the shapes of the lightcurves were changing overnight. On December 14, a difference between the Rc and V measurements is visible at a rotation phase of about 0.3 but the few V measurements made during the first part of the night support the explanation of a change due to the changing phase angle. On December 15, the B and Ic curves are relatively different on all the rotation but the phase angle is probably again the main culprit.
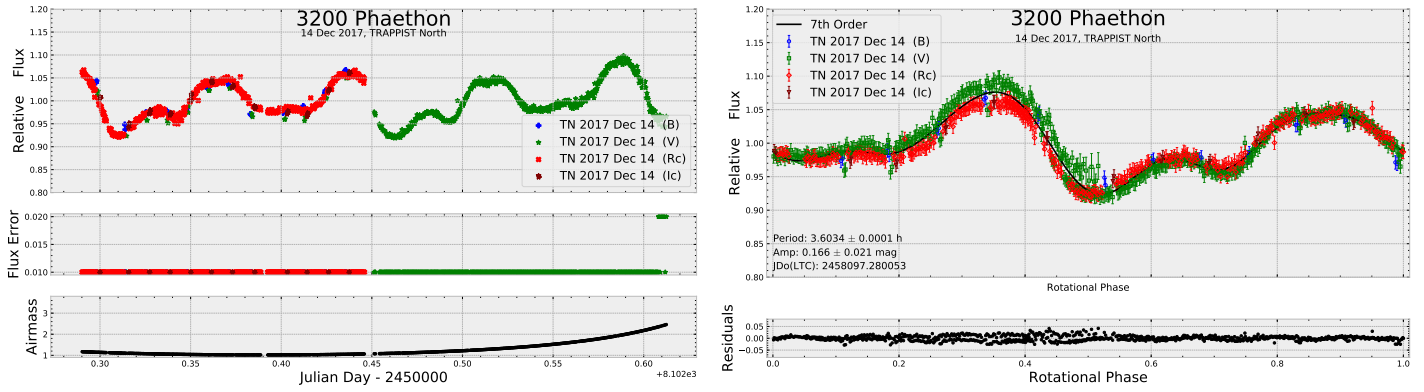
Figure 5.38: *Left*: Lightcurve in Julian Days taken with TRAPPIST-N on December 14 with the B, V, Rc and Ic filters. *Right*: The corresponding phased lightcurve.
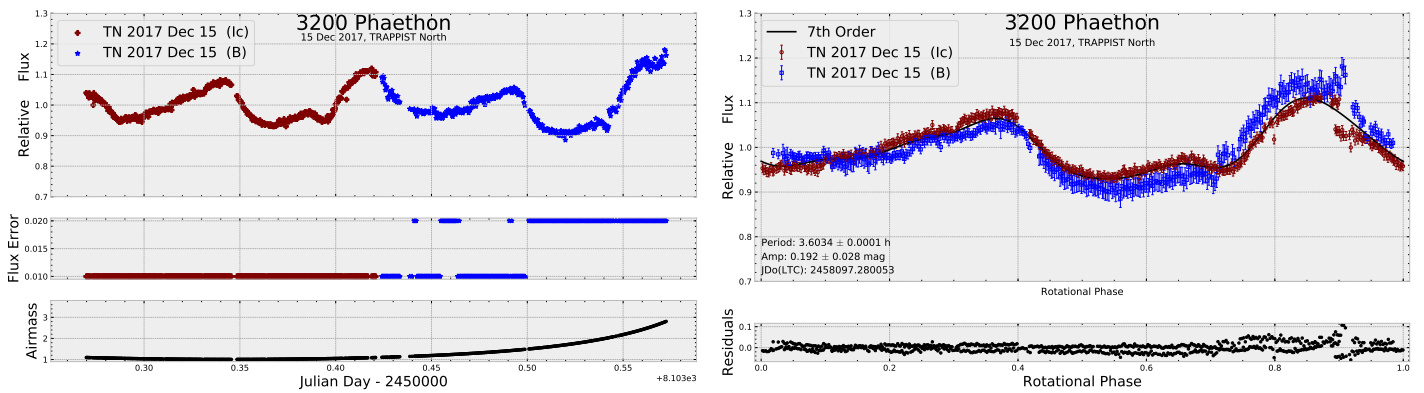

Figure 5.39: *Left*: Lightcurve in Julian Days taken with TRAPPIST-N on December 15 with the B, and Ic filters. *Right*: The corresponding phased lightcurve.

Shape model

In addition to the data of December 9, 10, 14 and 15 already presented, we also observed Phaethon on December 13, 18, 19 and 20 with the Rc filter. The lightcurve in Julian days of these nights and their corresponding phased lightcurves (detrended from the magnitude variation) are shown in Fig. 5.40. The large change in phase angle during the time span of the observations resulted in spectacular changes in the shape and amplitude of the lightcurve. These changes are illustrated in Fig. 5.41, where the Fourier fits of each night (at the exception of Dec. 20 because of insufficient rotation coverage) are plotted. The lightcurve amplitude went from 0.09 mag on December 9 (Fig. 5.35) to 0.92 mag on December 20 (Fig. A.2).

With TRAPPIST-N, we obtained a large number of measurements of Phaethon's brightness variation at phase angles ranging from 19° to 110°, which is very useful for the reconstruction of its shape with the *Lightcurve Inversion* technique (Kaasalainen et al., 2002a). We also used the data of the 7 nights of observation by Claudine Rinner with the MOSS telescope, after light-time correction of each epochs. The phased lightcurves of these nights are given in Appendix A. In addition, to cover more viewing geometries and illumination, we added to the data set the 51 lightcurves available on DAMIT (2570 individual measurements), obtained between 1994 and 2015 (Ansdell et al., 2014; Hanuš et al., 2016a; Pravec et al., 1998; Warner, 2015). The model available on DAMIT is based on these lightcurves (Hanuš et al., 2016a). The preferred pole orientation is $(\lambda, \beta) = (319°, -39°)$ and the resulting shape model at three different viewing geometries is shown in Fig. 5.42.
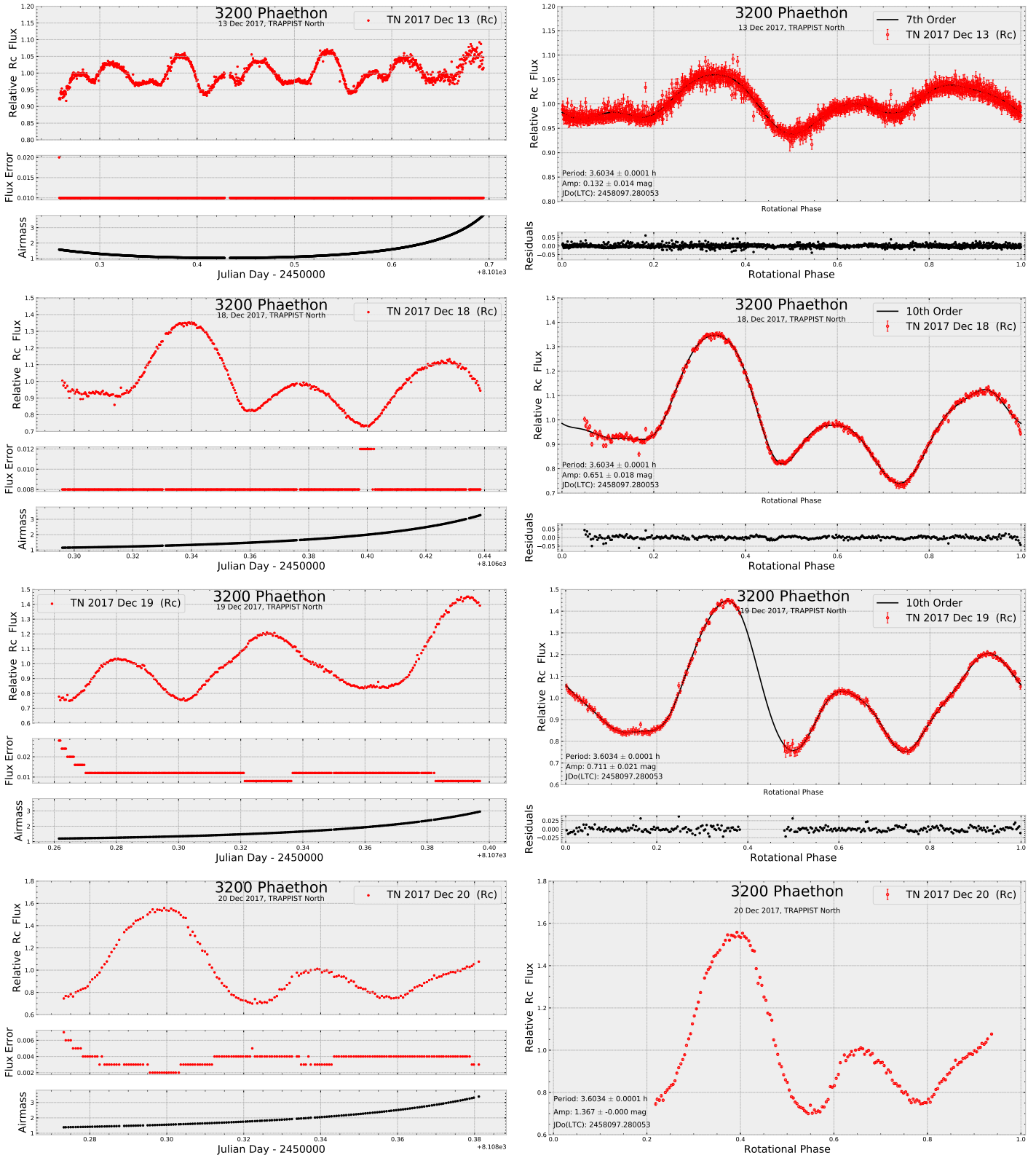
Figure 5.40: *Left*: Lightcurve in Julian Days taken with TRAPPIST-N on December 13, 18, 19 and 20 with the Rc filter. *Right*: The corresponding phased lightcurves.
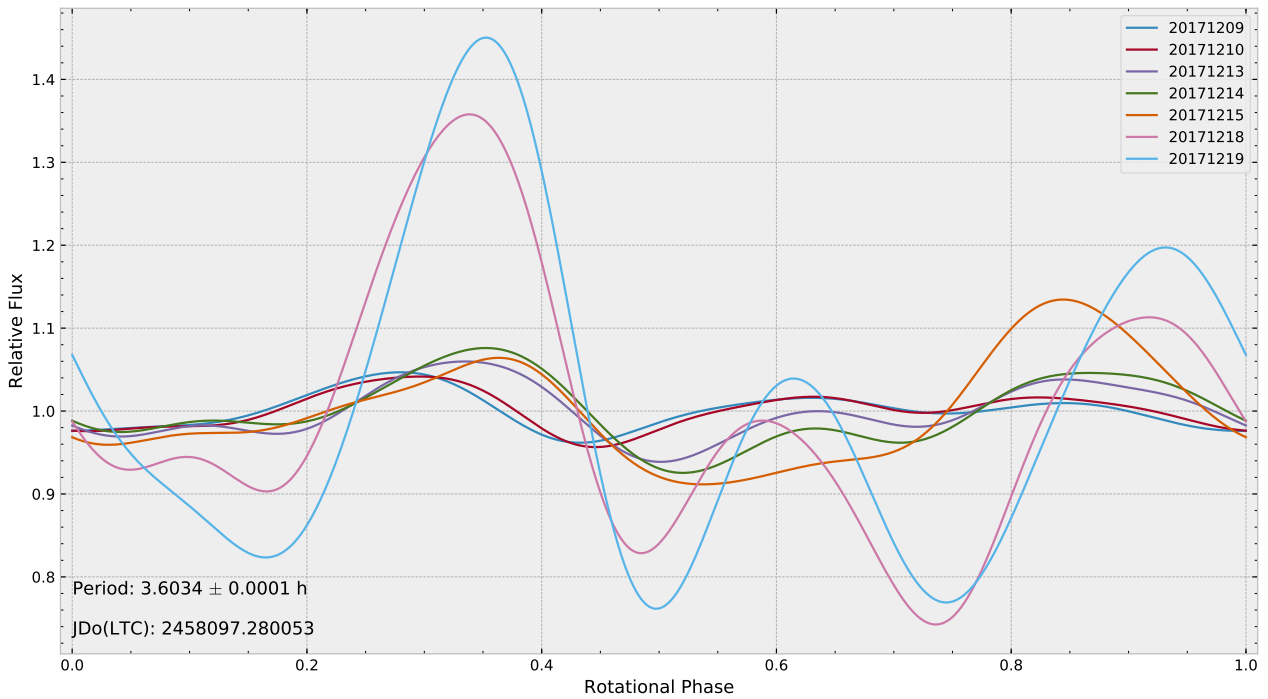
Figure 5.41: Fourier fit of first 7 nights of observations of Phaethon with TRAPPIST-N, between December 9 and December 19, 2017.
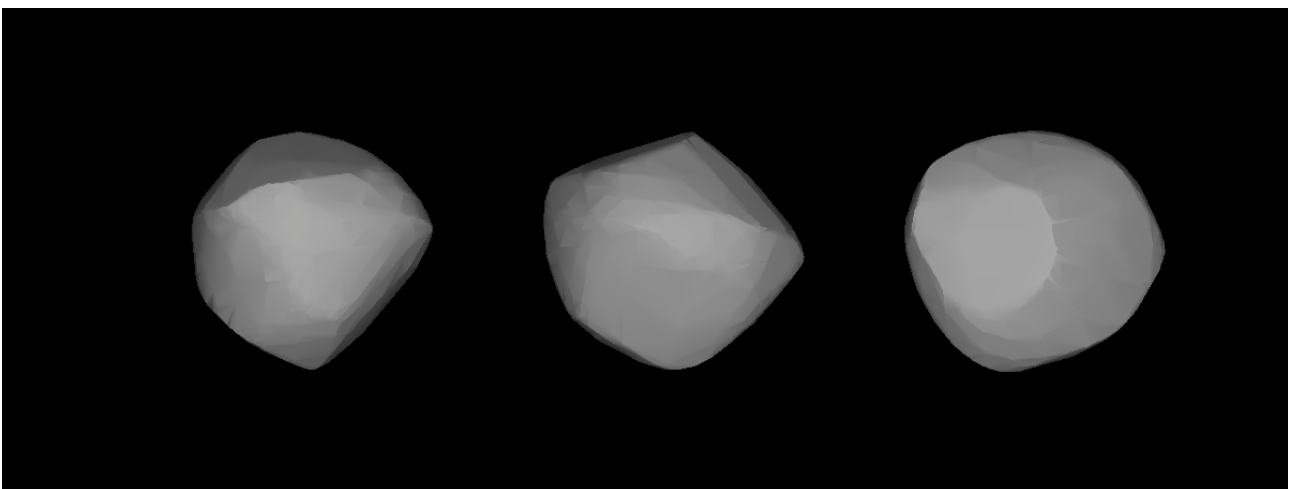

Figure 5.42: The shape model of Hanuš et al. (2016a) available on DAMIT.

We used the *Convexinv* procedure on our extended data set (8260 individual measurements) to produce a new shape model and spin axis orientation. The result is a pole orientation of $(\lambda, \beta) = (314°, -51°)$ and a shape model shown in Fig. 5.43.
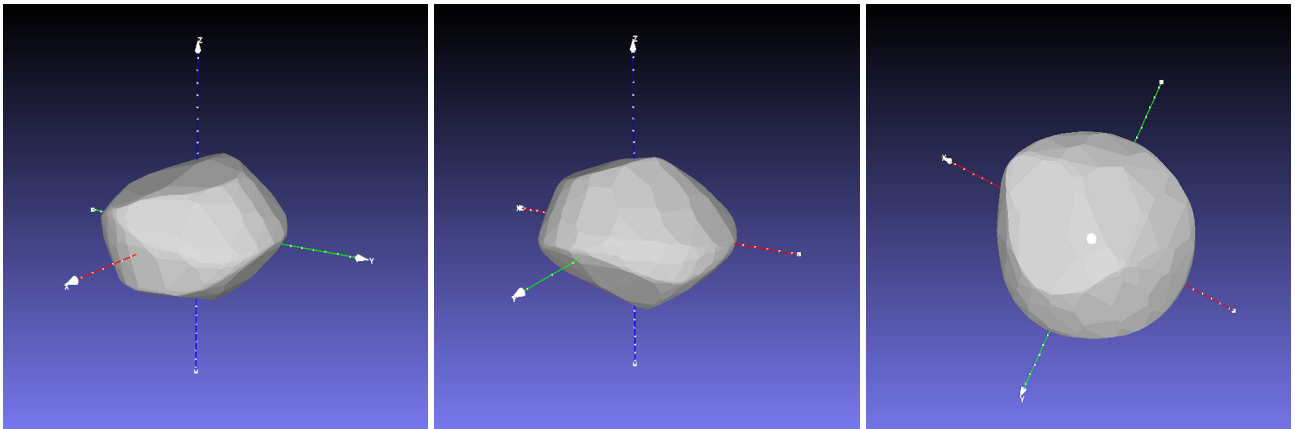
Figure 5.43: Shape model of Phaethon produced with the *Convexinv* procedure (Kaasalainen et al., 2002a) and using the TRAPPIST-N and MOSS lightcurves, plus those available on DAMIT.

The *Lightcurve Inversion* software (Kaasalainen et al., 2002a) creates also a file with the brightness of the asteroid generated by the shape model for the epochs used in the input lightcurves. It allows to compare the generated lightcurves with the input ones, as shown on Fig. 5.44.

Figure 5.44: Example of lightcurves of Phaethon used for the shape modelling with the corresponding synthetic lightcurve generated. *Top:* Dec. 4, 2007 (Hanuš et al., 2016a). *Bottom:* Dec. 18, 2017 with TRAPPIST-N.

Conclusions

With the telescopes TRAPPIST-South and TRAPPIST-North, we observed 9 Main-belt asteroids ((596) Scheila, (476) Hedwig, (89) Julia, (24) Themis, (31) Euphrosyne, (20) Massalia, (145) Adeona, (45) Eugenia and (22) Kall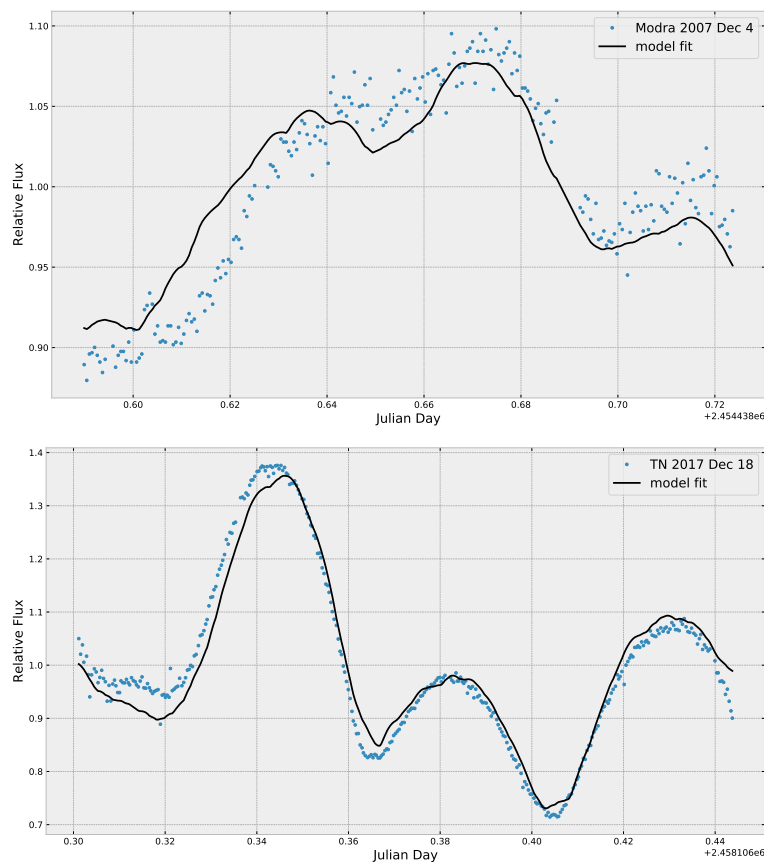iope) and 4 near-Earth asteroids ((3122) Florence, K17V12R, K18D01H and (3200) Phaethon) which allowed us to obtain a lot of results. A large amount of data have been gathered on about 50 nights of observation and the resulting lightcurves contain a total of more than 28,000 individual measurements. For most asteroids, the rotation was completely covered and densely sampled lightcurves were produced. At the exceptions of Scheila, Hedwig and K18V12R, new rotation periods have been derived for each asteroid.

We produced rotation lightcurves for the 9 MBAs that we observed. Each data set had some particularities and its own difficulties, such as a high brightness of the asteroid, a slow rotation, pollution by nearby stars or a low lightcurve amplitude. For (22) Kalliope, we also analysed data taken in February 2012 with TRAPPIST-S during the season of mutual eclipses of the asteroid with its satellite Linus. We detected the brightness attenuation due to the shadow of Linus being projected on the surface of (22) Kalliope on February 27, by taking the observations of February 5 and 7 as reference lightcurves. Such observations will help to characterise this interesting binary system.

We provided our lightcurves of the 9 MBAs to the ESO Large Programme and they will be used in a multi-data sources modelling of their shapes and spin axis orientations. Such models are used to derive the bulk densities of the asteroids and the distribution of the largest craters at their surfaces. These informations help to address entirely new questions about the formation and evolution of the planetesimals and the Solar System. For instance, the question of the origin of the Julia family from a collisional event at the surface of (89) Julia was challenged in Vernazza et al. (2018). Using the new shape model resulting of the disk-resolved images taken with the ESO VLT and new optical lightcurves, they identified the crater that probably originates from this impact.

The observations of (3122) Florence and K17V12R allowed us to refine their rotation periods and for K18D01H the previously unknown period was determined, in agreement with other teams. The lightcurves obtained will be used in addition of radar observations in future shape modelling.

We extensively observed (3200) Phaethon during its flyby of Earth on December 2017 and obtained more than 5000 images on 8 nights. We used the B, V, Rc and Ic filters during 4 of these nights to investigate for potential colour variations through Phaethon's rotation but none were detected above the noise level. Because of the rapidly changing phase angle after December 13, we could observe spectacular changes in the lightcurve shape and amplitude. The amplitude went from 0.09 mag on December 9 to 0.90 mag on December 20. In addition of the TRAPPIST-N data, we used the MOSS data taken also during the 2017 flyby and data available on

DAMIT, taken between 1994 and 2015 by various observers, to reconstruct a new shape model of Phaethon with optical lightcurves only and we derived the pole orientation. Moreover, observations of Phaethon are important for the preparation of the Japanese JAXA DESTINY+ in-situ mission scheduled in 2022.

The ESO LP aims to obtain disk-resolved observations of about 40 asteroids, each at 5 different apparitions. New rotation lightcurves are thus always needed to support the shape modelling. Observations of these large MBAs with TRAPPIST-S and TRAPPIST-N will continue in the future. Moreover, new NEAs passing by the Earth will regularly provide new interesting targets to observe.

MOSS phased lightcurves of (3200) Phaethon

Figures of the the phased lightcurves of Phaethon taken with the MOSS telescope on December 2017 by Claudine Rinner and Michel Ory. Fits by 7th order Fourier series are also plotted on each figure, at the exception of December 18 and 21 because of insufficient rotation coverage.
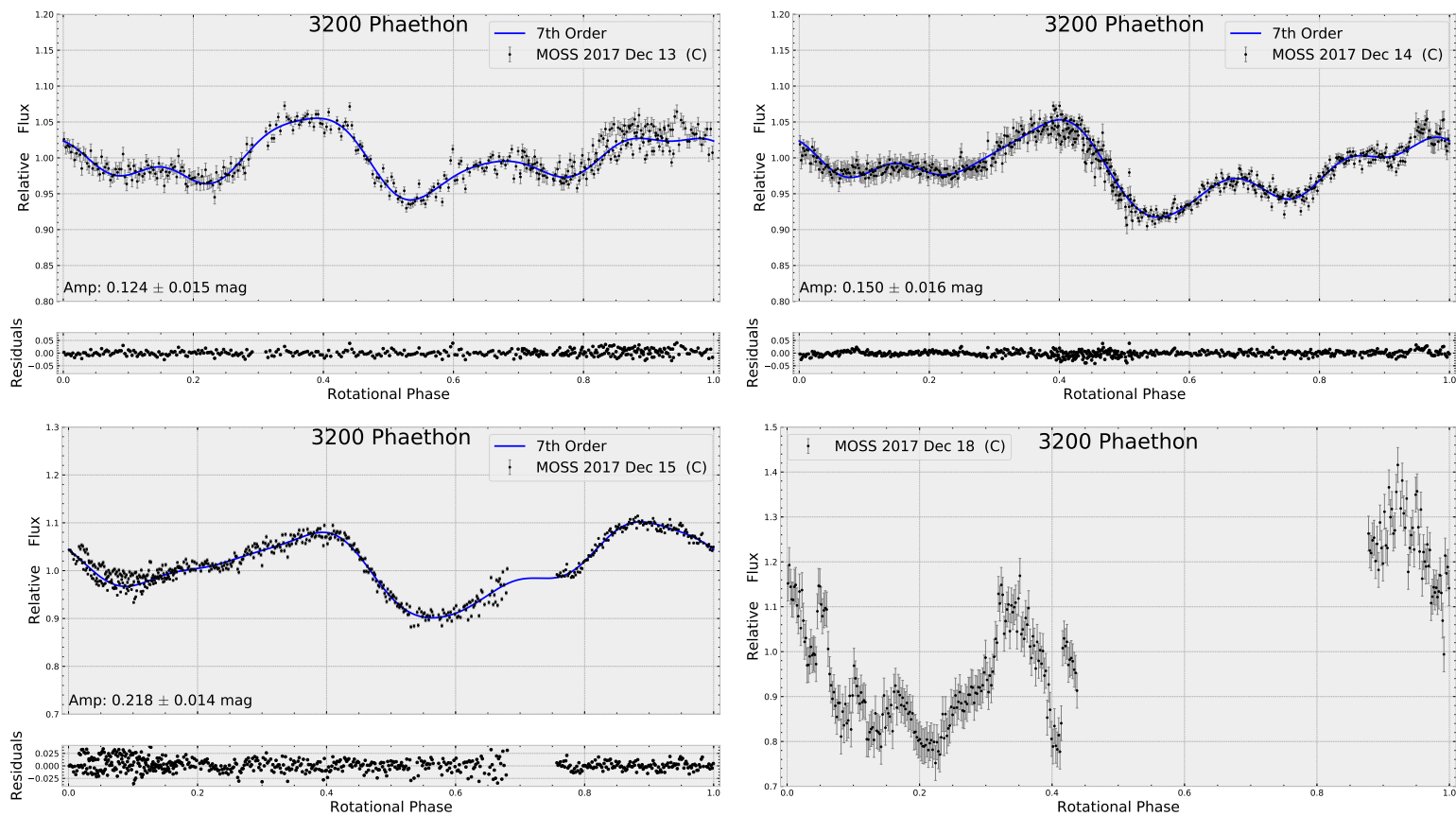

Figure A.1: Phased lightcurve of (3200) Phaethon taken with the MOSS telescope on December 13, 14, 15, 18.
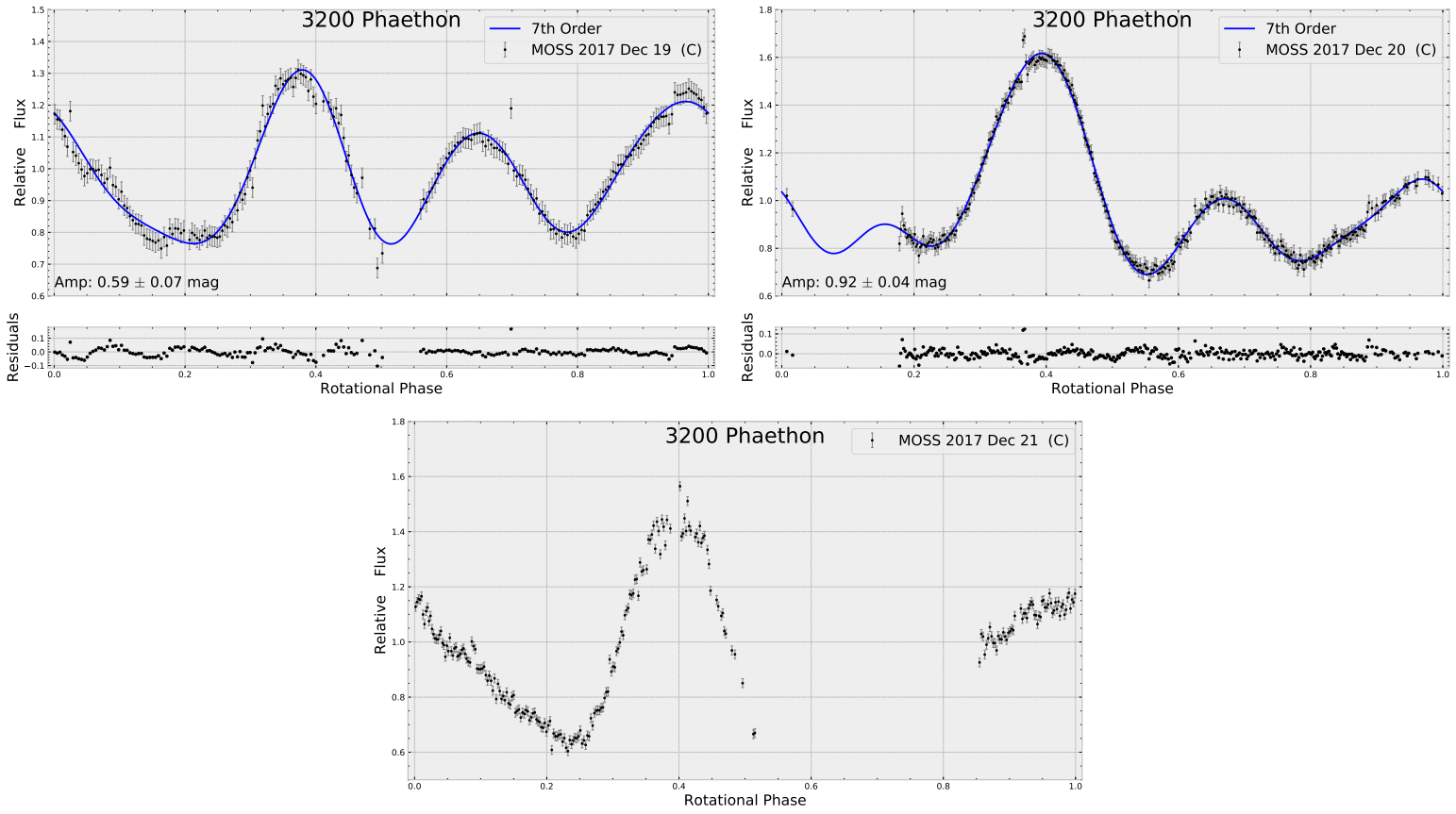
Figure A.2: Phased lightcurve of (3200) Phaethon taken with the MOSS telescope on December 19, 20 and 21.

NEA distances with the parallax method

When a relatively close object is observed from two separate sites, its apparent position changes compared to the more distant background stars. Measuring the angular shift (i.e. the parallax angle γ) allows to calculate the distance d of this target. In the ideal case, the target is centred on the baseline B, the distance between the two observations points (fig. B.1). Then the distance of the target is given by :

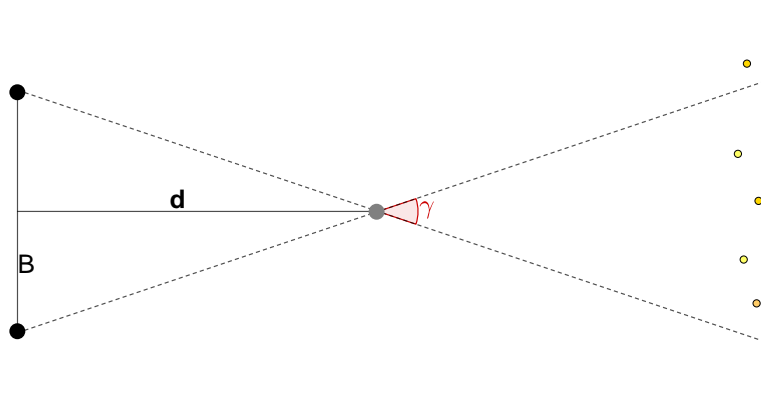$$d = \frac{B/2}{\tan(\gamma/2)}.$$

Figure B.1: Ideal case of the parallax method.

The parallax method has been widely used to determine distances of nearby stars. In this case, the star can be observed six months apart, providing a large baseline of around 2 au thanks to the revolution of the Earth around the Sun. Here we applied the method to estimate the distance of NEAs when they are close to Earth. As the distances to asteroids are much smaller than the stars, the baseline can be smaller as well. A measurable angular shift (a few arcseconds) can be obtained by observing from two separate sites on Earth. We used TRAPPIST-S and TRAPPIST-N, which provide us a quite large baseline of 8600 km. However, we are not in the conditions of the ideal case when applying the technique to asteroids because the two sites are usually not at the same distance to the asteroid, which is moving on the sky anyway. Thus, an effective baseline has to be computed and used instead of the full baseline.

We define a spherical coordinate system where the angle ϕ_X and ϕ_Y are the latitudes of the observatories X and Y (fig. B.2, left). The angle β is the longitude difference between the two sites and $R_\oplus$ is the Earth's radius taken as 6738.1 km. The vectors $\vec{X}$ and $\vec{Y}$ joining the Earth's centre to the observatories X and Y are given by:

$$\vec{X} = R_\oplus(\cos(\phi_X), 0, \sin(\phi_X))$$

$$\vec{Y} = R_{\oplus}(\cos(\phi_Y)\cos(\beta), \cos(\phi_Y)\sin(\beta), \sin(\phi_Y)).$$

The baseline is the difference of the two vectors:
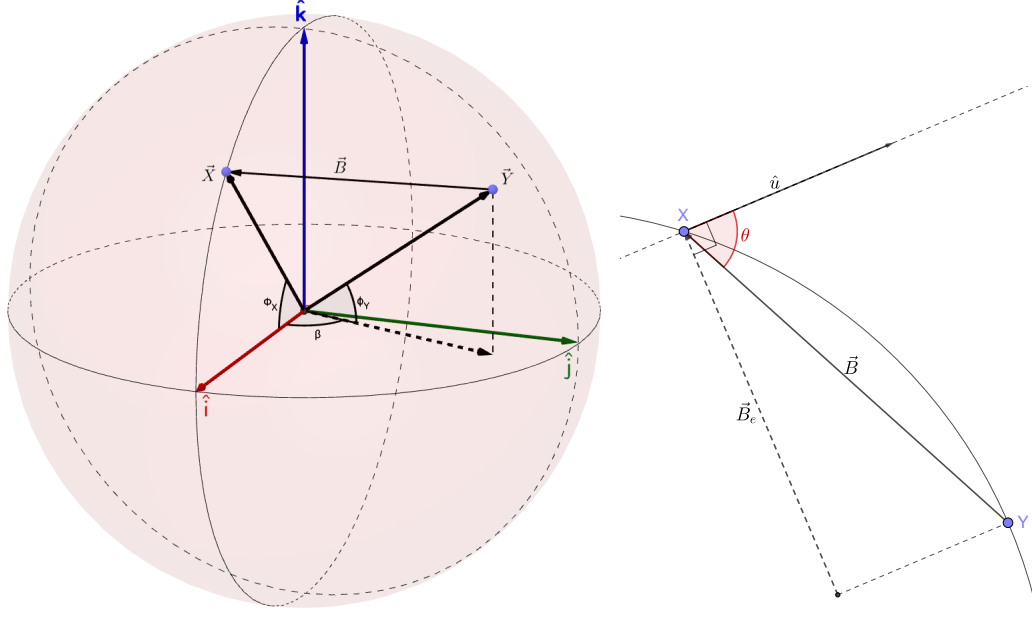
$$\vec{B} = \vec{X} - \vec{Y}.$$

Figure B.2: *Left*: Coordinates system used to calculate the baseline between the two observatories. *Right*: Figure of the effective baseline.

To obtain the effective baseline $\vec{B}_e$ we first define a unit vector $\hat{u}$ that goes from the observatory X toward the asteroid using the hour angle H and the declination δ of the asteroid for the observatory X (fig. B.2, right).

$$\hat{u} = (\cos(H)\cos(\delta), \sin(H)\cos(\delta), \sin(\delta)).$$

The angle θ between $\vec{B}$ and $\hat{u}$ is obtained with the dot product

$$\cos(\theta) = \frac{\hat{u}.\vec{B}}{|\hat{u}||\vec{B}|}.$$

As the effective baseline is the projection of $\vec{B}$ on the line perpendicular to $\hat{u}$, we have

$$B_e = |\vec{B}|\sin(\theta).$$

Finally the distance can be then computed the same way as for the ideal case by substituting B_e to B:

$$d = \frac{B_e/2}{\tan(\gamma/2)}.$$

To measure the parallax angle we took images of the asteroid from the two separated observing sites and with observing time as close as possible to each other. Then we can compare the positions of the asteroid with respect to nearby stars. However, here we choose to stack the images together and directly measure the angular shift on the asteroid itself. Indeed, on a stack of multiple images from the two observatories the asteroid is seen as two parallel trails. As the two cameras of TRAPPIST-N and TRAPPIST-S don't have the same field of view and plate scale, the images from one telescope are projected into the coordinates system of the other. This has been done with the *match_fits* function of the *FITS_tools* python library.

Bibliography

M. Ansdell, K. J. Meech, Hainaut O., Buie M. W., Kaluna H., Bauer J., and Dundon J. Refined rotational period, pole solution, and shape model for (3200) phaethon. *ApJ*, 793(1):50, 2014. URL http://stacks.iop.org/0004-637X/793/i=1/a=50.

T. Arai, M. Kobayashi, K. Ishibashi, F. Yoshida, H. Kimura, K. Wada, H. Senshu, M. Yamada, O. Okudaira, T. Okamoto, S. Kameda, R. Srama, H. Kruger, M. Ishiguro, H. Yabuta, T. Nakamura, J. Watanabe, T. Ito, K. Ohtsuka, S. Tachibana, T. Mikouchi, M. Komatsu, K. Nakamura-Messenger, S. Sasaki, T. Hiroi, S. Abe, S. Urakawa, N. Hirata, H. Demura, G. Komatsu, T. Noguchi, T. Sekiguchi, T. Inamori, H. Yano, M. Yoshikawa, T. Ohtsubo, T. Okada, T. Iwata, K. Nishiyama, T. Toyota, Y. Kawakatsu, and T. Takashima. DESTINY+ Mission: Flyby of Geminids Parent Asteroid (3200) Phaethon and In-Situ Analyses of Dust Accreting on the Earth. In *Lunar and Planetary Science Conference*, volume 49 of *Lunar and Planetary Inst. Technical Report*, page 2570, March 2018.

M. Birlan, M. A. Barucci, P. Vernazza, M. Fulchignoni, R. P. Binzel, S. J. Bus, I. Belskaya, and S. Fornasier. Near-IR spectroscopy of asteroids 21 Lutetia, 89 Julia, 140 Siwa, 2181 Fogelin and 5480 (1989YK8), potential targets for the Rosetta mission; remote observations campaign on IRTF. *New Astronomy*, 9:343–351, June 2004. doi: 10.1016/j.newast.2003.12.005.

F. Braga-Ribas, B. Sicardy, J. L. Ortiz, C. Snodgrass, F. Roques, R. Vieira-Martins, J. I. B. Camargo, M. Assafin, R. Duffard, E. Jehin, J. Pollock, R. Leiva, M. Emilio, D. I. Machado, C. Colazo, E. Lellouch, J. Skottfelt, M. Gillon, N. Ligier, L. Maquet, G. Benedetti-Rossi, A. R. Gomes, P. Kervella, H. Monteiro, R. Sfair, M. El Moutamid, G. Tancredi, J. Spagnotto, A. Maury, N. Morales, R. Gil-Hutton, S. Roland, A. Ceretta, S.-H. Gu, X.-B. Wang, K. Harpsøe, M. Rabus, J. Manfroid, C. Opitom, L. Vanzi, L. Mehret, L. Lorenzini, E. M. Schneiter, R. Melia, J. Lecacheux, F. Colas, F. Vachier, T. Widemann, L. Almenares, R. G. Sandness, F. Char, V. Perez, P. Lemos, N. Martinez, U. G. Jørgensen, M. Dominik, F. Roig, D. E. Reichart, A. P. Lacluyze, J. B. Haislip, K. M. Ivarsen, J. P. Moore, N. R. Frank, and D. G. Lambas. A ring system detected around the Centaur (10199) Chariklo. *Nature*, 508:72–75, April 2014. doi: 10.1038/nature13155.

S. J. Bus and R. P. Binzel. Phase II of the Small Main-Belt Asteroid Spectroscopic Survey. A Feature-Based Taxonomy. *Icarus*, 158:146–177, July 2002. doi: 10.1006/icar.2002.6856.

B. Carry. Density of asteroids. *P&SS*, 73:98–118, December 2012. doi: 10.1016/j.pss.2012.03.009.

B. Carry, M. Kaasalainen, C. Leyrat, W. J. Merline, J. D. Drummond, A. Conrad, H. A. Weaver, P. M. Tamblyn, C. R. Chapman, C. Dumas, F. Colas, J. C. Christou, E. Dotto, D. Perna, S. Fornasier, L. Bernasconi, R. Behrend, F. Vachier, A. Kryszczynska, M. Polinska, M. Fulchignoni, R. Roy, R. Naves, R. Poncy, and P. Wiggins. Physical properties of the ESA Rosetta target asteroid (21) Lutetia. II. Shape and flyby geometry. *A&A*, 523: A94, November 2010. doi: 10.1051/0004-6361/201015074.

B. Carry, M. Kaasalainen, W. J. Merline, T. G. Müller, L. Jorda, J. D. Drummond, J. Berthier, L. O'Rourke, J. Ďurech, M. Küppers, A. Conrad, P. Tamblyn, C. Dumas, H. Sierks, Osiris Team, M. A'Hearn, F. Angrilli, C. Barbieri, A. Barucci, J.-L. Bertaux, C. , G., V. Da Deppo, B. Davidsson, S. Debei, M. De Cecco, S. Fornasier, M. Fulle, O. Groussin, P. Gutiérrez, W.-H. H. Ip, S., H. U. Keller, D. Koschny, J. Knollenberg, J. R. Kramm, E. Kuehrt, P. Lamy, L. M. Lara, M. Lazzarin, J. J. López-Moreno, F. Marzari, H. Michalik, G. Naletto, H. Rickman, R. Rodrigo, L. Sabau, N. Thomas, and K.-P. Wenzel. Shape modeling technique KOALA validated by ESA Rosetta at (21) Lutetia. *P&SS*, 66:200–212, June 2012. doi: 10.1016/j.pss.2011.12.018.

J. de León, H. Campins, K. Tsiganis, A. Morbidelli, and J. Licandro. Origin of the near-Earth asteroid Phaethon and the Geminids meteor shower. *A&A*, 513:A26, April 2010. doi: 10.1051/0004-6361/200913609.

F. E. DeMeo and B. Carry. Solar System evolution from compositional mapping of the asteroid belt. *Nature*, 505:629–634, January 2014. doi: 10.1038/nature12908.

F. E. DeMeo, R. P. Binzel, S. M. Slivan, and S. J. Bus. An extension of the Bus asteroid taxonomy into the near-infrared. *Icarus*, 202:160–180, July 2009. doi: 10.1016/j.icarus.2009.02.005.

P. Descamps, F. Marchis, J. Pollock, J. Berthier, F. Vachier, M. Birlan, M. Kaasalainen, A. W. Harris, M. H. Wong, W. J. Romanishin, E. M. Cooper, K. A. Kettner, P. Wiggins, A. Kryszczynska, M. Polinska, J.-F. Coliac, A. Devyatkin, I. Verestchagina, and D. Gorshanov. New determination of the size and bulk density of the binary Asteroid 22 Kalliope from observations of mutual eclipses. *Icarus*, 196:578–600, August 2008. doi: 10.1016/j.icarus.2008.03.014.

J. Durech, V. Sidorin, and M. Kaasalainen. DAMIT: a database of asteroid models. *A&A*, 513:A46, April 2010. doi: 10.1051/0004-6361/200912693. Accessed: From 2017-09-01 to 2018-05-31 http://astro.troja.mff.cuni.cz/projects/asteroids3D/web.php?page=project_main_page.

J. Durech, B. Carry, M. Delbo, M. Kaasalainen, and M. Viikinkoski. Asteroid Models from Multiple Data Sources. In P. Michel, F. E. DeMeo, and W. F. Bottke, editors, *Asteroids IV*, pages 183–202. University of Arizona Press, 2015. doi: 10.2458/azu_uapress_9780816532131-ch010.

M. Gillon, E. Jehin, S. M. Lederer, L. Delrez, J. de Wit, A. Burdanov, V. Van Grootel, A. J. Burgasser, A. H. M. J. Triaud, C. Opitom, B.-O. Demory, D. K. Sahu, D. Bardalez Gagliuffi, P. Magain, and D. Queloz. Temperate Earth-sized planets transiting a nearby ultracool dwarf star. *Nature*, 533:221–224, May 2016. doi: 10.1038/nature17448.

M. Gillon, A. H. M. J. Triaud, B.-O. Demory, E. Jehin, E. Agol, K. M. Deck, S. M. Lederer, J. de Wit, A. Burdanov, J. G. Ingalls, E. Bolmont, J. Leconte, S. N. Raymond, F. Selsis, M. Turbet, K. Barkaoui, A. Burgasser, M. R. Burleigh, S. J. Carey, A. Chaushev, C. M. Copperwheat, L. Delrez, C. S. Fernandes, D. L. Holdsworth, E. J. Kotze, V. Van Grootel, Y. Almleaky, Z. Benkhaldoun, P. Magain, and D. Queloz.

Seven temperate terrestrial planets around the nearby ultracool dwarf star TRAPPIST-1. *Nature*, 542:456–460, February 2017. doi: 10.1038/nature21360.

S. Green and C. Kowal. 1983 TB. *IAUcirc*, 3878, October 1983.

J. Hanuš, M. Delbo', D. Vokrouhlický, P. Pravec, J. P. Emery, V. Alí-Lagoa, B. Bolin, M. Devogèle, R. Dyvig, A. Galád, R. Jedicke, L. Kornoš, P. Kušnirák, J. Licandro, V. Reddy, J.-P. Rivet, J. Világi, and B. D. Warner. Near-Earth asteroid (3200) Phaethon: Characterization of its orbit, spin state, and thermophysical parameters. *A&A*, 592:A34, July 2016a. doi: 10.1051/0004-6361/201628666.

J. Hanuš, J. Ďurech, D. A. Oszkiewicz, R. Behrend, B. Carry, M. Delbo, O. Adam, V. Afonina, R. Anquetin, P. Antonini, L. Arnold, M. Audejean, P. Aurard, M. Bachschmidt, B. Baduel, E. Barbotin, P. Barroy, P. Baudouin, L. Berard, N. Berger, L. Bernasconi, J.-G. Bosch, S. Bouley, I. Bozhinova, J. Brinsfield, L. Brunetto, G. Canaud, J. Caron, F. Carrier, G. Casalnuovo, S. Casulli, M. Cerda, L. Chalamet, S. Charbonnel, B. Chinaglia, A. Cikota, F. Colas, J.-F. Coliac, A. Collet, J. Coloma, M. Conjat, E. Conseil, R. Costa, R. Crippa, M. Cristofanelli, Y. Damerdji, A. Debackère, A. Decock, Q. Déhais, T. Déléage, S. Delmelle, C. Demeautis, M. Dróżdż, G. Dubos, T. Dulcamara, M. Dumont, R. Durkee, R. Dymock, A. Escalante del Valle, N. Esseiva, R. Esseiva, M. Esteban, T. Fauchez, M. Fauerbach, M. Fauvaud, S. Fauvaud, E. Forné, C. Fournel, D. Fradet, J. Garlitz, O. Gerteis, C. Gillier, M. Gillon, R. Giraud, J.-P. Godard, R. Goncalves, H. Hamanowa, H. Hamanowa, K. Hay, S. Hellmich, S. Heterier, D. Higgins, R. Hirsch, G. Hodosan, M. Hren, A. Hygate, N. Innocent, H. Jacquinot, S. Jawahar, E. Jehin, L. Jerosimic, A. Klotz, W. Koff, P. Korlevic, E. Kosturkiewicz, P. Krafft, Y. Krugly, F. Kugel, O. Labrevoir, J. Lecacheux, M. Lehký, A. Leroy, B. Lesquerbault, M. J. Lopez-Gonzales, M. Lutz, B. Mallecot, J. Manfroid, F. Manzini, A. Marciniak, A. Martin, B. Modave, R. Montaigut, J. Montier, E. Morelle, B. Morton, S. Mottola, R. Naves, J. Nomen, J. Oey, W. Ogłoza, M. Paiella, H. Pallares, A. Peyrot, F. Pilcher, J.-F. Pirenne, P. Piron, M. Polińska, M. Polotto, R. Poncy, J. P. Previt, F. Reignier, D. Renauld, D. Ricci, F. Richard, C. Rinner, V. Risoldi, D. Robilliard, D. Romeuf, G. Rousseau, R. Roy, J. Ruthroff, P. A. Salom, L. Salvador, S. Sanchez, T. Santana-Ros, A. Scholz, G. Séné, B. Skiff, K. Sobkowiak, P. Sogorb, F. Soldán, A. Spiridakis, E. Splanska, S. Sposetti, D. Starkey, R. Stephens, A. Stiepen, R. Stoss, J. Strajnic, J.-P. Teng, G. Tumolo, A. Vagnozzi, B. Vanoutryve, J. M. Vugnon, B. D. Warner, M. Waucomont, O. Wertz, M. Winiarski, and M. Wolf. New and updated convex shape models of asteroids based on optical data from a large collaboration network. *A&A*, 586:A108, February 2016b. doi: 10.1051/0004-6361/201527441.

J. Hanuš, M. Viikinkoski, F. Marchis, J. Ďurech, M. Kaasalainen, M. Delbo', D. Herald, E. Frappa, T. Hayamizu, S. Kerr, S. Preston, B. Timerson, D. Dunham, and J. Talbot. Volumes and bulk densities of forty asteroids from ADAM shape modeling. *A&A*, 601:A114, May 2017. doi: 10.1051/0004-6361/201629956.

A. W. Harris, J. W. Young, E. Bowell, L. J. Martin, R. L. Millis, M. Poutanen, F. Scaltriti, V. Zappala, H. J. Schober, H. Debehogne, and K. W. Zeigler. Photoelectric observations of asteroids 3, 24, 60, 261, and 863. *Icarus*, 77:171–186, January 1989. doi: 10.1016/0019-1035(89)90015-8.

H. H. Hsieh and D. Jewitt. A Population of Comets in the Main Asteroid Belt. *Science*, 312:561–563, April 2006. doi: 10.1126/science.1125150.

E. Jehin. Report on the ground-based observation campaign of 67P/Churyumov-Gerasimenko. In *AAS/Division for Planetary Sciences Meeting Abstracts #47*, volume 47 of *AAS/Division for Planetary Sciences Meeting Abstracts*, page 413.12, November 2015.

E. Jehin, M. Gillon, D. Queloz, P. Magain, J. Manfroid, V. Chantry, M. Lendl, D. Hutsemékers, and S. Udry. TRAPPIST: TRAnsiting Planets and PlanetesImals Small Telescope. *The Messenger*, 145:2–6, September 2011a.

E. Jehin, J. Manfroid, D. Hutsemékers, M. Gillon, and P. Magain. Long term photometric monitoring of comet 103P/Hartley2 with the new robotic TRAPPIST telescope. In *EPSC-DPS Joint Meeting 2011*, page 1489, October 2011b.

E. Jehin, C. Opitom, J. Manfroid, D. Hutsemékers, and M. Gillon. The TRAPPIST comet survey in 2014. In *AAS/Division for Planetary Sciences Meeting Abstracts #46*, volume 46 of *AAS/Division for Planetary Sciences Meeting Abstracts*, page 209.21, November 2014a.

E. Jehin, C. Opitom, J. Manfroid, D. Hutsemékers, and M. Gillon. The TRAPPIST comet survey. In K. Muinonen, A. Penttilä, M. Granvik, A. Virkki, G. Fedorets, O. Wilkman, and T. Kohout, editors, *Asteroids, Comets, Meteors 2014*, July 2014b.

D. Jewitt and J. Li. Activity in Geminid Parent (3200) Phaethon. *AJ*, 140:1519–1527, November 2010. doi: 10.1088/0004-6256/140/5/1519.

D. Jewitt, J. Li, and J. Agarwal. The Dust Tail of Asteroid (3200) Phaethon. *ApJ*, 771:L36, July 2013. doi: 10.1088/2041-8205/771/2/L36.

D. Jewitt, H. Hsieh, and J. Agarwal. The Active Asteroids. In P. Michel, F. E. DeMeo, and W. F. Bottke, editors, *Asteroids IV*, pages 221–241. University of Arizona Press, 2015. doi: 10.2458/azu_uapress_9780816532131-ch012.

David Jewitt, Harold Weaver, Max Mutchler, Stephen Larson, and Jessica Agarwal. Hubble space telescope observations of main-belt comet (596) scheila. *ApJ*, 733(1):L4, 2011. URL http://stacks.iop.org/2041-8205/733/i=1/a=L4.

M. Kaasalainen and J. Torppa. Optimization Methods for Asteroid Lightcurve Inversion. I. Shape Determination. *Icarus*, 153:24–36, September 2001. doi: 10.1006/icar.2001.6673.

M. Kaasalainen, S. Mottola, and M. Fulchignoni. Asteroid Models from Disk-integrated Data. In W. F. Bottke, Jr., A. Cellino, P. Paolicchi, and R. P. Binzel, editors, *Asteroids III*, pages 139–150. University of Arizona Press, 2002a.

M. Kaasalainen, J. Torppa, and J. Piironen. Models of Twenty Asteroids from Photometric Data. *Icarus*, 159: 369–395, October 2002b. doi: 10.1006/icar.2002.6907.

D. Kinoshita, K. Ohtsuka, T. Ito, S. Miyasaka, T. Nakamura, S. Abe, and W.-P. Chen. Rotationally time-resolved vis-spectroscopy of (3200) Phaethon. *ArXiv e-prints*, March 2017.

J.-Y. Li, P. Helfenstein, B. Buratti, D. Takir, and B. E. Clark. Asteroid Photometry. In P. Michel, F. E. DeMeo, and W. F. Bottke, editors, *Asteroids IV*, pages 129–150. University of Arizona Press, 2015. doi: 10.2458/azu_uapress_9780816532131-ch007.

C. Magri, M. C. Nolan, S. J. Ostro, and J. D. Giorgini. A radar survey of main-belt asteroids: Arecibo observations of 55 objects during 1999 2003. *Icarus*, 186:126–151, January 2007. doi: 10.1016/j.icarus.2006.08.018.

A. Mainzer, T. Grav, J. Masiero, J. Bauer, R. M. Cutri, R. S. McMillan, C. R. Nugent, D. Tholen, R. Walker, and E. L. Wright. Physical Parameters of Asteroids Estimated from the WISE 3-Band Data and NEOWISE Post-Cryogenic Survey. *ApJ*, 760:L12, November 2012. doi: 10.1088/2041-8205/760/1/L12.

F. Marchis, M. Baek, P. Descamps, J. Berthier, D. Hestroffer, and F. Vachier. S/2004 (45) 1. *IAUcirc*, 8817, March 2007.

A. Marciniak, P. Bartczak, T. Santana-Ros, T. Michałowski, P. Antonini, R. Behrend, C. Bembrick, L. Bernasconi, W. Borczyk, F. Colas, J. Coloma, R. Crippa, N. Esseiva, M. Fagas, M. Fauvaud, S. Fauvaud, D. D. M. Ferreira, R. P. Hein Bertelsen, D. Higgins, R. Hirsch, J. J. E. Kajava, K. Kamiński, A. Kryszczyńska, T. Kwiatkowski, F. Manzini, J. Michałowski, M. J. Michałowski, A. Paschke, M. Polińska, R. Poncy, R. Roy, G. Santacana, K. Sobkowiak, M. Stasik, S. Starczewski, F. Velichko, H. Wucher, and T. Zafar. Photometry and models of selected main belt asteroids. IX. Introducing interactive service for asteroid models (ISAM). *A&A*, 545:A131, September 2012. doi: 10.1051/0004-6361/201219542.

A. Marciniak, F. Pilcher, D. Oszkiewicz, T. Santana-Ros, S. Urakawa, S. Fauvaud, P. Kankiewicz, Ł. Tychoniec, M. Fauvaud, R. Hirsch, J. Horbowicz, K. Kamiński, I. Konstanciak, E. Kosturkiewicz, M. Murawiecka, J. Nadolny, K. Nishiyama, S. Okumura, M. Polińska, F. Richard, T. Sakamoto, K. Sobkowiak, G. Stachowski, and P. Trela. Against the biases in spins and shapes of asteroids. *P&SS*, 118:256–266, December 2015. doi: 10.1016/j.pss.2015.06.002.

M. Marsset, B. Carry, C. Dumas, J. Hanuš, M. Viikinkoski, P. Vernazza, T. G. Müller, M. Delbo, E. Jehin, M. Gillon, J. Grice, B. Yang, T. Fusco, J. Berthier, S. Sonnett, F. Kugel, J. Caron, and R. Behrend. 3D shape of asteroid (6) Hebe from VLT/SPHERE imaging: Implications for the origin of ordinary H chondrites. *A&A*, 604:A64, August 2017. doi: 10.1051/0004-6361/201731021.

NASA/JPL. Horizons web-interface. Accessed: From 2017-09-01 to 2018-05-31 https://ssd.jpl.nasa.gov/horizons.cgi, 2017a.

NASA/JPL. Small-body database browser. Accessed: From 2017-09-01 to 2018-05-31 https://ssd.jpl.nasa.gov/sbdb.cgi, 2017b.

A. Nathues, S. Mottola, M. Kaasalainen, and G. Neukum. Spectral study of the Eunomia asteroid family. I. Eunomia. *Icarus*, 175:452–463, June 2005. doi: 10.1016/j.icarus.2004.12.013.

D. Nesvorný, M. Brož, and V. Carruba. Identification and Dynamical Properties of Asteroid Families. In P. Michel, F. E. DeMeo, and W. F. Bottke, editors, *Asteroids IV*, pages 297–321. University of Arizona Press, 2015. doi: 10.2458/azu_uapress_9780816532131-ch016.

S. J. Ostro, R. S. Hudson, L. A. M. Benner, J. D. Giorgini, C. Magri, J. L. Margot, and M. C. Nolan. Asteroid Radar Astronomy. In W. F. Bottke, Jr., A. Cellino, P. Paolicchi, and R. P. Binzel, editors, *Asteroids III*, pages 151–168. University of Arizona Press, 2002.

E. Paunzen and T. Vanmunster. Peranso - Light curve and period analysis software. *Astronomische Nachrichten*, 337:239, March 2016. doi: 10.1002/asna.201512254.

F. Pilcher. Rotation period determinations for 80 Sappho, 145 Adeona, 217 Eudora, 274 Philagoria, 567 Eleutheria, AND 826 Henrika. *Minor Planet Bulletin*, 37:148–149, 2010.

P. Pravec and A. W. Harris. Fast and Slow Rotation of Asteroids. *Icarus*, 148:12–20, November 2000. doi: 10.1006/icar.2000.6482.

P. Pravec, M. Wolf, and L. Šarounová. Lightcurves of 26 Near-Earth Asteroids. *Icarus*, 136:124–153, November 1998. doi: 10.1006/icar.1998.5993.

P. Pravec, P. Scheirich, J. Ďurech, J. Pollock, P. Kušnirák, K. Hornoch, A. Galád, D. Vokrouhlický, A. W. Harris, E. Jehin, J. Manfroid, C. Opitom, M. Gillon, F. Colas, J. Oey, J. Vraštil, D. Reichart, K. Ivarsen, J. Haislip, and A. LaCluyze. The tumbling spin state of (99942) Apophis. *Icarus*, 233:48–60, May 2014. doi: 10.1016/j.icarus.2014.01.026.

A. Schwarzenberg-Czerny. Fast and Statistically Optimal Period Search in Uneven Sampled Observations. *ApJ*, 460:107, April 1996. doi: 10.1086/309985.

B. Sicardy, J. L. Ortiz, M. Assafin, E. Jehin, A. Maury, E. Lellouch, R. G. Hutton, F. Braga-Ribas, F. Colas, D. Hestroffer, J. Lecacheux, F. Roques, P. Santos-Sanz, T. Widemann, N. Morales, R. Duffard, A. Thirouin, A. J. Castro-Tirado, M. Jelínek, P. Kubánek, A. Sota, R. Sánchez-Ramírez, A. H. Andrei, J. I. B. Camargo, D. N. da Silva Neto, A. R. Gomes, R. V. Martins, M. Gillon, J. Manfroid, G. P. Tozzi, C. Harlingten, S. Saravia, R. Behrend, S. Mottola, E. G. Melendo, V. Peris, J. Fabregat, J. M. Madiedo, L. Cuesta, M. T. Eibe, A. Ullán, F. Organero, S. Pastor, J. A. de Los Reyes, S. Pedraz, A. Castro, I. de La Cueva, G. Muler, I. A. Steele, M. Cebrián, P. Montañés-Rodríguez, A. Oscoz, D. Weaver, C. Jacques, W. J. B. Corradi, F. P. Santos, W. Reis, A. Milone, M. Emilio, L. Gutiérrez, R. Vázquez, and H. Hernández-Toledo. A Pluto-like radius and a high albedo for the dwarf planet Eris from an occultation. *Nature*, 478:493–496, October 2011. doi: 10.1038/nature10550.

C. Snodgrass, C. Opitom, M. de Val-Borro, E. Jehin, J. Manfroid, T. Lister, J. Marchant, G. H. Jones, A. Fitzsimmons, I. A. Steele, R. J. Smith, H. Jermak, T. Granzer, K. J. Meech, P. Rousselot, and A.-C. Levasseur-Regourd. The perihelion activity of comet 67P/Churyumov-Gerasimenko as seen by robotic telescopes. *MNRAS*, 462: S138–S145, November 2016. doi: 10.1093/mnras/stw2300.

A. Springmann, P. Dalba, F. Marchis, F. Vachier, J. Berthier, P. Descamps, B. Morris, A. Marciniak, T. Santana i Ros, and A. Kryszczynska. Physical and Orbital Properties of the (22) Kalliope System from Mutual Eclipse Observations. In *Asteroids, Comets, Meteors 2012*, volume 1667 of *LPI Contributions*, page 6352, May 2012.

P. A. Taylor, S. E. Marshall, F. Venditti, A. K. Virkki, L. A. M. Benner, M. Brozovic, S. P. Naidu, E. S. Howell, T. R. Kareta, V. Reddy, D. Takir, A. S. Rivkin, L. F. Zambrano-Marin, S. S. Bhiravarasu, E. G. Rivera-Valentin, B. Aponte-Hernandez, C. Rodriguez Sanchez-Vahamonde, M. C. Nolan, J. D. Giorgini, R. J. Vervack, Y. R. Fernandez, J. L. Crowell, D. S. Lauretta, and T. Arai. Radar and Infrared Observations of Near-Earth Asteroid 3200 Phaethon. In *Lunar and Planetary Science Conference*, volume 49 of *Lunar and Planetary Inst. Technical Report*, page 2509, March 2018.

D. J. Tholen. *Asteroid taxonomy from cluster analysis of photometry*. PhD thesis, University of Arizona, Tucson, September 1984.

P. Vernazza, M. Broz, A. Drouard, J. Hanuš, M. Viikinkoski, M. Marsset, L. Jorda, R. Fetick, B. Carry, F. Marchis, M. Birlan, T. Fusco, T. Santana-Ros, E. Podlewska, E. Jehin, M. Ferrais, P. Bartczak, G. Dudziński, J. Berthier, J. Castillo-Rogez, F. Cipriani, F. Colas, Durech. F, M. Kaasalainen, A. Kryszczynska, P. Lamy, H. Le Coroller,

T. Marciniak, T. Michalowski, P. Michel, M. Pajuelo, P. Tanga, P. Vachier, A. Vigan, B. Warner, O. Witasse, B. Yang, E. Asphaug, D. C. Richardson, and P. Ševeček. The impact crater at the origin of the ∼100 Myrs old Julia family detected with VLT/SPHERE? Submitted, 2018.

M. Viikinkoski, M. Kaasalainen, and J. Durech. ADAM: a general method for using various data types in asteroid reconstruction. *A&A*, 576:A8, April 2015. doi: 10.1051/0004-6361/201425259.

M. Viikinkoski, J. Hanuš, M. Kaasalainen, F. Marchis, and J. Ďurech. Adaptive optics and lightcurve data of asteroids: twenty shape models and information content analysis. *A&A*, 607:A117, November 2017. doi: 10.1051/0004-6361/201731456.

B. D. Warner. Near-Earth Asteroid Lightcurve Analysis at CS3-Palmer Divide Station: 2014 October-December. *Minor Planet Bulletin*, 42:115–127, April 2015.

B. D. Warner. *A Practical Guide to Lightcurve Photometry and Analysis*. pringer International Publishing Switzerland, 2016. doi: 10.1007/978-3-319-32750-1.

B. D. Warner, A. W. Harris, and P. Pravec. The asteroid lightcurve database. *Icarus*, 202:134–146, July 2009. doi: 10.1016/j.icarus.2009.02.003. Updated 2018 March 7. http://www.MinorPlanet.info/lightcurvedatabase.html.

D.B. Warner. Asteroid lightcurve analysis at CS3-Palmer Divide Station: 2017 April through June. *Minor Planet Bulletin*, 44:289–294, 2017.

D.B. Warner. Near-Earth Asteroid lightcurve analysis at CS3-Palmer Divide Station: 2017 July through October. *Minor Planet Bulletin*, 45:19–34, 2018a.

D.B. Warner. Asteroid lightcurve analysis at CS3-Palmer Divide Station: 2017 July through October. *Minor Planet Bulletin*, 45:39–45, 2018b.

I. P. Williams and Z. Wu. The Geminid meteor stream and asteroid 3200 Phaethon. *MNRAS*, 262:231–248, May 1993. doi: 10.1093/mnras/262.1.231.

B. Zellner, D. J. Tholen, and E. F. Tedesco. The eight-color asteroid survey - Results for 589 minor planets. *Icarus*, 61:355–416, March 1985. doi: 10.1016/0019-1035(85)90133-2.